Gaining insights into brain tissues using multi-compartment T2 relaxometry models

Sudhanya Chatterjee

UNIVERSITE BRETAGNE LOIRE MATHSTIC

UNIVERSITÉ DE RENNES 1

THESE DE DOCTORAT DE

L'UNIVERSITE DE RENNES 1
COMUE UNIVERSITE BRETAGNE LOIRE

ECOLE DOCTORALE N° 601
Mathématiques et Sciences et Technologies de l'Information et de la Communication
Spécialité : *Signal Image Vision*

Par
Sudhanya CHATTERJEE

Gaining insights into brain tissues using multi-compartment T_2 relaxometry models

Thèse présentée et soutenue à Rennes, le 5 Décembre 2018
Unité de recherche : VisAGeS U1228, INRIA/INSERM, IRISA, UMR CNRS 6074
Thèse N° :

Rapporteurs avant soutenance :

Jean-Philippe THIRAN Associate professor, EPFL, Switzerland
Jean-Philippe RANJEVA Professor of Neuroscience, Marseille, France

Composition du Jury :

Président:	Eric MARCHAND	Professor, Université de Rennes 1, Rennes.
Examinateurs:	Jean-Philippe THIRAN	Associate professor, EPFL, Switzerland
	Jean-Philippe RANJEVA	Professor of Neuroscience, Marseille, France
	Helene RATINEY	Chargée de recherche, CREATIS, Lyon
	Bruno STANKOFF	Professor, Université Pierre et Marie Curie
Encadrants:	Simon K. WARFIELD	Professor, Boston Children's Hospital
	Olivier Commowick	Chargée de recherche, INRIA, Rennes
Dir. de thèse:	Christian BARILLOT	Directeur de recherche, CNRS

Titre : Analyse quantitative des tissus cérébraux à l'aide de modèles multi-compartiments en IRM de relaxométrie T2

Mots clés : relaxométrie T2, IRM, microstructures, sclérose en plaques

Résumé : L'imagerie par résonance magnétique (IRM) est l'une des méthodes d'imagerie in-vivo les plus utilisées pour obtenir de l'information sur la santé du cerveau. Cependant, les voxels d'IRM ont une résolution limitée en raison de contraintes physiques. L'objectif de cette thèse est d'obtenir des estimations quantitatives des microstructures tissulaires cérébrales (comme la myéline, les matières intra/extra-cellulaires et l'eau libre) à partir des données d'IRM T2 relaxométrie. Deux modèles paramétriques multi-compartiments (MCT2) sont proposés dans cette thèse. L'approche et le cadre d'estimation pour les deux modèles sont justifiés en utilisant des études de simulation. Une série de simulations et d'expériences sur des données IRM in vivo ont été réalisées pour évaluer l'exactitude et la robustesse de ces modèles. Le modèle jugé plus robuste a ensuite été utilisé pour deux études sur de patients atteints de sclérose en plaques (SEP). Dans la première étude, l'évolution des biomarqueurs de MCT2 a été étudiée dans les lésions de SEP présentant une prise de contraste gadolinium (Gd) ou non chez 10 patients sur une période de trois ans. Dans la deuxième étude, nous avons démontré le potentiel de l'utilisation combinée des biomarqueurs MCT2 proposés avec ceux obtenus à partir de modèles existants de diffusion multi-compartiment IRM pour répondre à une tâche cliniquement pertinente et difficile : identifier les régions de lésions SEP en cours de dégradation de la barrière hémato-encéphalique sans utilisation de produit de contraste.

Title : Gaining insights into brain tissues using multi-compartment T2 relaxometry models

Keywords : T2 relaxometry, MRI, microstructure, multiple sclerosis

Abstract: Magnetic resonance imaging (MRI) is one of the most widely used in-vivo imaging method for obtaining information on brain health. However, MRI voxels have limited resolution due to physical constraints. The objective of this thesis is to obtain quantitative estimates of brain tissue microstructures (such as myelin, intra/extracellular matters and free water) from T2 relaxometry MRI data. Two parametric multi-compartment T2 relaxometry (MCT2) models are proposed in this thesis. The approach and estimation framework for both models were justified using cost function simulation studies. A range of simulation and in-vivo MRI data experiments were performed to evaluate the accuracy and robustness of these models. The model found to be more robust of the two was then used for two studies on multiple sclerosis (MS) lesions. In the first study the evolution of the MCT2 biomarkers was studied in gadolinium (Gd) enhancing and non-enhancing regions of MS lesions in 10 patients with clinically isolated syndrome over a period of three years. In the second study we demonstrated the potential of combined use of the proposed MCT2 biomarkers with those obtained from existing multi-compartment diffusion MRI models to address a clinically relevant and challenging task of identifying regions of MS lesions undergoing active blood brain barrier breakdown without use of Gd injection.

Acknowledgments

I would like to start by thanking Christian Barillot for providing his support throughout this period. His optimism and motivation has immensely helped me in learning various aspects of research patiently through the ups and downs of the PhD. I will always be thankful for sharing his research experiences with me and for his support at the critical moments. Olivier Commowick has been very kind with all his support and advice at every step of this PhD. His clarity of vision on research, critical thinking ability and dexterity in seeing through ideas from conception to realization has immensely helped me in learning how to perform research. Numerous discussions with Olivier has helped me learn a lot in these few years. I would like to thank Simon K. Warfield for providing critical insights into the subject matter at various stages of the PhD. Stimulating discussions with Simon on many occasions has helped me identify the scopes for improvement. I will always cherish the significant learning experiences from the research trips to Boston as a part of the BARBANT collaboration.

I would like to thank Jean-Philippe Thiran and Jean-Philippe Ranjeva for reading the thesis and reporting on it with constructive remarks. I am also thankful to Simon K. Warfield, Hélène Ratiney, Eric Marchand and Bruno Stankoff for agreeing to be a part of the jury for the thesis defense. I would like to thank all the jury members again for providing their comments on this work.

I would to take this opportunity to thank a few more people who have contributed to this PhD. Onur Afacan has helped me immensely with his inputs on this work. His intuitive explanations on various aspects of MRI acquisitions and discussions with him on results has helped me in many ways. I would also like to thank him for all his help in conducting the experiments while I visited Boston. I thank Elise Bannier for her help in developing the quantitative MRI protocols for our studies in Rennes. She has been very patient in explaining the complexities of acquisition methods in simpler terms and in helping me understand various aspects of it. I will always cherish my discussions with Emmanuel Caruyer and would like to thank him for his kind help throughout my time at Rennes.

The Visages team members have extended their help to me at all times. Thanks again to everyone in the team for making my stay in Rennes a wonderful time.

I would like to thank Dattesh D. Shanbhag for the numerous stimulating discussions we had on medical imaging topics which motivated me to take up the PhD research. I will always be thankful to him for his kind and patient efforts to teach me various aspects of the subject. I would also take this opportunity to thank Kajoli Krishnan, Suresh Joel, Sandeep Kaushik and Radhika Madhavan for their insightful opinions at various times while I was at Bangalore (and even after!).

I would now like to thank my parents without whose support none of this would have been possible. Thanks again for standing by me through all the ups and downs and extending your immense support at each and every step of my life. I thank my grandparents for their love and support. I would like to thank Salini for patiently being by my side through these times and for being a source of motivation.

I would finally like to extend a heartfelt thanks and gratitude to my grandfather, late Sudhanshu S. Chatterjee who has always been an inspiration for me. I would like to dedicate this manuscript to him.

Sudhanya Chatterjee

Contents

Part I

Introduction

Chapter 1

Obtaining brain tissue microstructure information from T2 relaxometry MRI

Contents

1.1 In vivo imaging using MRI

The nucleus must possess the property of *spin* to undergo nuclear magnetic resonance (NMR). It might have a spin quantum number of 0, a half integer or a whole number. Nucleus with a half integer or whole number spin quantum number can undergo NMR. Magnetic resonance imaging (MRI) is an application of NMR for in-vivo imaging of the human body. The hydrogen nuclei posses the spin property (1/2 spin). Its abundance in the human body (in the form of protons in water) makes it an important element while studying NMR in the context of in-vivo imaging. The principles of NMR are discussed in much greater detail in [Bloch 1946, Purcell 1946, Callaghan 1993] among the many other reports. In the scope of this thesis, we shall discuss introductory concepts in the field of NMR and spin echo methods. Further discussions will be carried out assuming we are imaging hydrogen nuclei (i.e. proton in water).

1.1.1 Introduction

The positively charged spinning proton behaves like a tiny bar magnet. In the absence of any external field, these dipoles are randomly aligned. However, in the presence of an external magnetic field (say B_0), the nucleus experiences a torque as its moment is aligned along the B_0 direction. This causes the nucleus to precess

around B_0 at a frequency called the Larmor frequency (ω_0). The Larmor frequency is proportional to B_0. They are associated with a constant called the gyromagnetic ratio (γ) as $\omega_0 = \gamma B_0$. This is illustrated in Fig. 1.1.

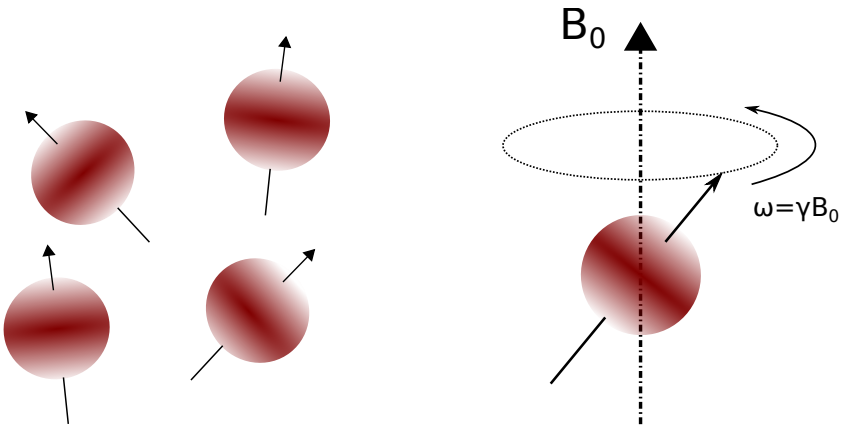

(a) (b)

Figure 1.1: (a) In absence of an external field, spinning nuclei are randomly oriented. When a bulk of these are considered, the net magnetization tends to be zero. (b) In the presence of an external field (B_0), the spinning nuclei precesses around the external field at a frequency ω_0 (Larmor frequency).

Henceforth we shall discuss the concepts considering many protons are present in the system (which is usually the case when a voxel is imaged using MRI). In the presence of an external field, the hydrogen nuclei can have two states: magnetization aligned along B_0 and magnetization aligned against B_0. In the presence of a high strength external magnetic field the former outnumber the later, resulting in a net magnetization value in direction of B_0. The net magnetization on the transverse plane in this state still tends to being nil.

This state is disturbed when an external radio frequency (RF) signal (at frequency ω_0) is applied perpendicular to B_0 i.e. on the transverse plane. This transverse magnetic field is commonly referred to as B_1. Due to this RF pulse, the net magnetization vector (M) direction starts tilting away from the B_0 field direction. The amount by which the tilt occurs is dependent on the magnitude and duration for which the RF pulse is applied. As a result of B_1 application, M now precesses around both B_0 and B_1. This also results in a non-zero magnetization signal in the transverse plane which can be detected and measured. This is illustrated in Fig. 1.2a. Let us say that observations made from outside is the laboratory frame. The axis directions for the laboratory framework are as shown in Fig. 1.2a. In the illustrations (and henceforth in this section) B_0 is applied in the z-direction. From the laboratory frame, the trajectory followed by the net magnetization when precessing away from the B_0 field direction and towards the transverse plane is spiral in

nature as the precession occurs both around B_0 and B_1. Hence from the laboratory frame, understanding the precession in the transverse plane is not straight forward. The transverse plane analysis becomes simplified when observed from the frame of rotation around B_0. This is illustrated in Fig. 1.2b, where the B_1 is considered to be along the x'-axis. From the rotating frame, M precesses only around B_1 as illustrated in Fig. 1.3.

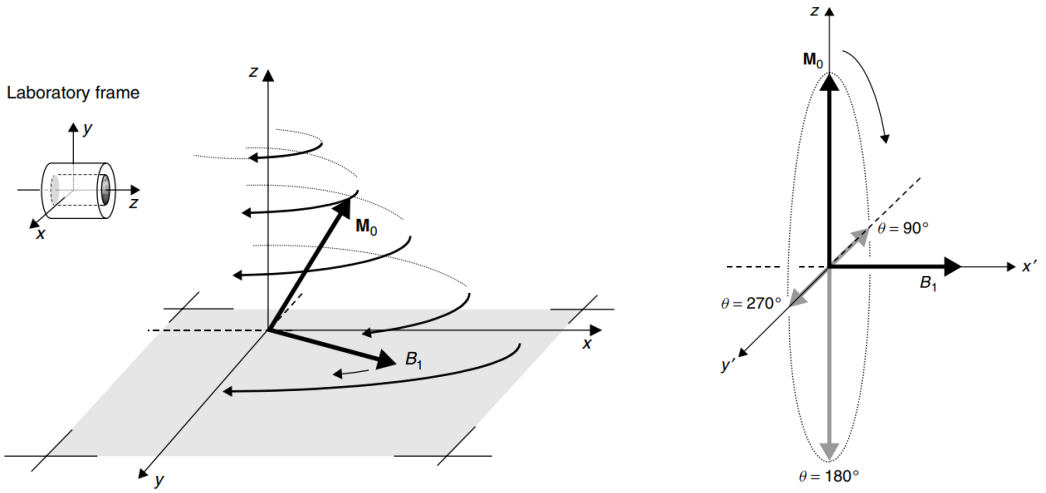

(a) (b)

Figure 1.2: In these illustrations, B_0 is applied in the z-direction. (a) The bulk magnetization precesses around both B_0 and B_1. (b) Observation from the rotating frame allows us to describe the transverse plane magnetization with much more ease. Image courtesy: [Tofts 2005].

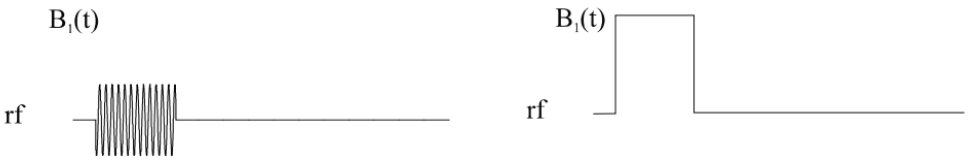

Figure 1.3: The RF signal while observing from the (left) laboratory and (right) rotation frame. When observation is made from the rotation frame, the B_1 applied along the transverse plane is constant (unlike oscillating when observed from laboratory frame). Image courtesy: [Brown 2014].

1.1.2 Relaxation

After the external RF signal is removed after some time, M starts aligning itself along the B_0 direction. Hence, the isochromats[1] transit from higher to lower energy

[1] An isochromat is a group of nuclei exposed to the same magnetic field B, hence precessing at the same frequency [Tofts 2005]. This concept is useful as in realistic scenarios (heterogeneous

states. This energy loss occurs in two forms: from the spin system to the lattice and within the spin system itself. The lattice may be regarded as the large thermal reservoir surrounding the spin system. The longitudinal magnetization goes back to the value existing prior to the RF signal application. This is referred to as the T_1 relaxation, or spin-lattice relaxation. The isochromats start losing the phase coherence due to the energy lost within the spin system. Hence the transverse component of M starts decaying (and does so exponentially). This is referred to as the T_2 decay. The spin-spin relaxation is caused due to a background magnetic field formed as result of a variety of processes[2]. Among these, the background magnetic field due to the dipole-dipole interaction is the most dominant (especially while studying relaxation of hydrogen nuclei in absence of contrast agents). Two components of this background field are important: (a) the component perpendicular to the B_0 direction, and (b) the one parallel to the B_0 direction. The former component is similar to an external RF signal and the precession due to this field results in a T_1 type relaxation. This phenomenon introduces a T_2 decay by removing some of the spin states in the transverse plane. This is also referred to at T_1 contribution to T_2, or as nonsecular T_2 contribution. Now let us discuss the effect of the second component of the background field i.e. the external magnetic field component parallel to the B_0 (say B_0'). An isochromat now experiences precession at two frequencies where one is proportional to $(B_0 + B_0')$ and the other is proportional to only B_0. Over a time t, this creates a phase difference in precession proportional to $B_0' t$ with respect to the isochromats precessing around B_0. Each isochromat develops such phase differences depending on the B_0' value experienced by it. This knocks the isochromats out of phase leading to each one precessing at a different rate and hence causing the T_2 relaxation. This phenomenon is referred to as the secular contribution to T_2 relaxation. So these are the basic phenomenons which explain the relaxation due to the energy disbursement within the spin system.

The assumption so far has been the uniformity of B_0 in and around the measured system. However, this is not always true. The B_0 value at the measured location might be slightly higher or lower than the expected value, due to which the phase coherence loss rate is higher than expected. Hence the observed transverse decay time is higher than the true value. This observed decay time is referred to as T_2^* and is as shown below:

$$\frac{1}{T_2^*} = \frac{1}{T_2} + \frac{1}{T_2'} \tag{1.1}$$

where T_2 is the true value and T_2' is due to the field inhomogeneity. This observation implies that the transverse decay measured after an external RF pulse is T_2^* weighted rather than being purely T_2 weighted.

However, measuring the true T_2 value is of interest as it is characteristic of the composition of the measured substance. It is a quantitative measurement. Mea-

systems), observing phenomenons from a single spin point of view is not always feasible. The isochromats help in explanation of the change of net magnetization while understanding relaxation phenomenons.

[2] refer Section 6.4 in [Tofts 2005] for further reading

surement of T_2 weighted signal was proposed by [Hahn 1952] using the spin echo method. In this method, a 90° RF pulse is applied along the x' direction (for axes refer to Fig. 1.2b) which tilts M along the transverse plane. Once the RF pulse is withdrawn, the isochromats start precessing at different rates. After a time duration (say τ), a 180° RF pulse is applied along the y' direction which flips the precessing isochromats as illustrated in Fig. 1.4. The 180° pulse is known as the refocusing pulse which creates the echo at time, $t = 2\tau$. The flip causes the faster precessing isochromats to lag behind the slower ones and is thus critical for forming the T_2 weighted echo signal. This is illustrated in Fig. 1.5.

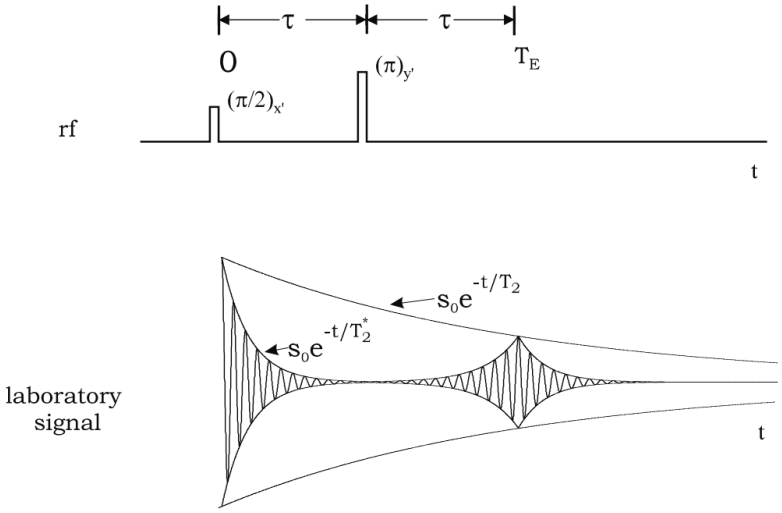

Figure 1.4: The spin echo method has been shown here. The signal at echo time (2τ) is T_2 weighted. Image courtesy: [Brown 2014].

In the classical spin echo method, a single echo is obtained after each 90° RF pulse. However, multiple refocusing pulses can be applied successively to obtain the T_2 decay signal at multiple echo times [Carr 1954]. This multiple echo spin echo method is shown in Fig. 1.6. The ability of this sequence to generate a perfect T_2 weighted echo train is reliant on the application of perfect refocusing pulse (i.e. exactly 180°) for each echo. This is however not always possible in measurement systems. A solution to this was proposed as a modified multiple echo spin echo method in [Meiboom 1958]. This method is popularly referred to as the Carr-Purcell-Meiboom-Gill (CPMG) method. The main idea of the CPMG method is to apply the 180° pulse with a slight error and with a phase in quadrature with the initial 90° pulse. As a result of this, the even echoes are T_2 weighted without error. The odd echoes are affected by the error introduced in the 180° pulse. Ideally, the error prone echoes should be left out of any analysis performed using the CPMG data.

Although the CPMG method addresses the issue of imperfect refocusing pulses, the echoes with imperfect refocusing generate stimulated echoes [Crawley 1987]. The stimulated echoes deform the T_2 exponential decay curve (examples shown in

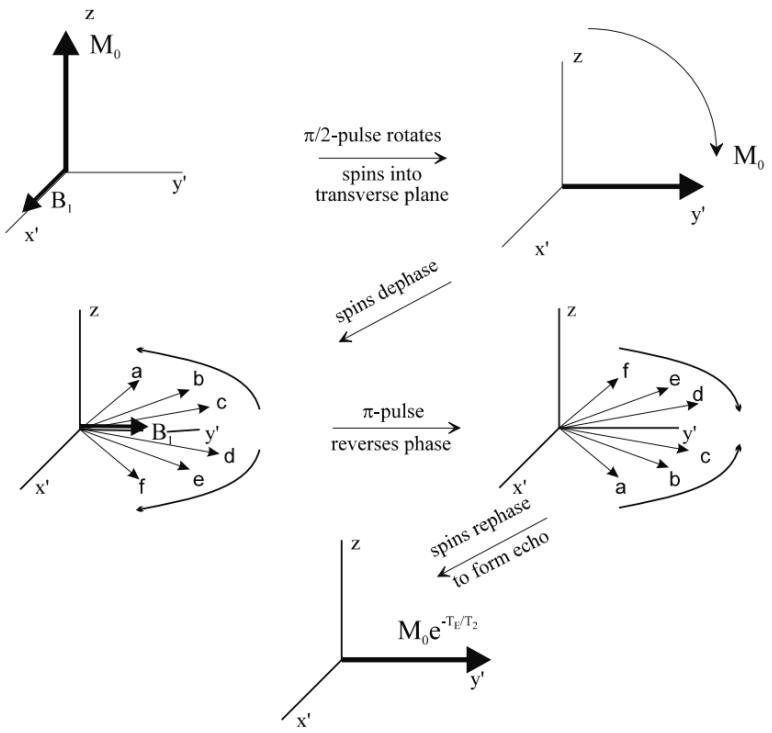

Figure 1.5: The spin echo formation is illustrated here. On application of the refocusing pulse (at $t = \tau$) the phases of the isochromats are flipped. This refocuses them to form an echo at time 2τ. Image courtesy: [Brown 2014].

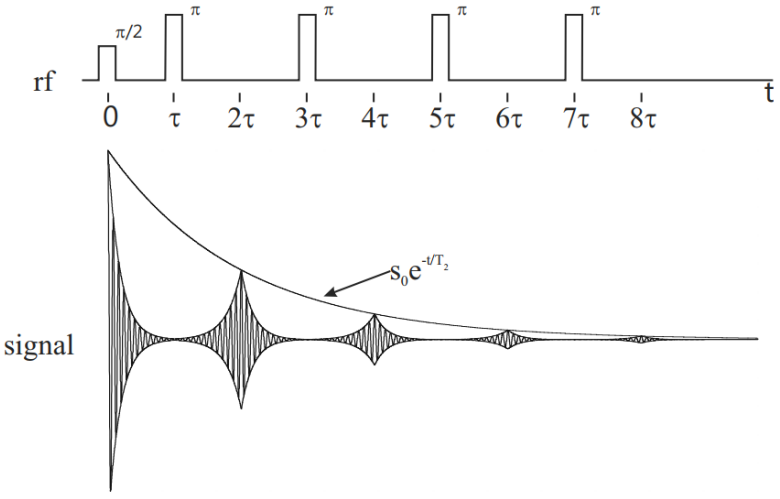

Figure 1.6: The multiple echo spin echo method has been shown here. The signal at multiple echo times by applying successive refocusing pulses. Image courtesy: [Brown 2014].

next section). However, there are methods which can account for the stimulated echo effects in the data. This is particularly important when the echo train data is used for fitting signal models to estimate the T_2 of the measured signal. This approach is popularly known as T_2 relaxometry. Obtaining T_2 relaxometry data of human tissues and using signal models to obtain their T_2 values has proved to be an effective technique for detecting anomalies [Tofts 2005]. Several decades of research have also been performed to develop signal models to obtain tissue microstructure information of tissues from T_2 relaxometry signals. An overview of such techniques will be provided in the next section.

1.2 Microstructure information from T_2 relaxometry MRI

In this section we focus on a few methods used for obtaining tissue microstructure information from T_2 relaxometry MRI data. As discussed in the last section, T_2 relaxometry MRI data acquires T_2 decay values of the image at multiple echo times. The most basic analysis would thus be to fit a single exponential curve (or a echo phase graph (EPG) curve accounting for the stimulated echoes) to the acquired data points for each voxel. The decay rate would provide us information on the transverse relaxation constants for the voxels. This is often referred to as mono-exponential analysis. Let us say that the acquired data (Y) has N echoes with an echo spacing of ΔTE. Hence we seek to solve the formulation shown below for each voxel:

$$\underset{M_0,T_2}{\arg\min} \sum_{i=1}^{N} \left(y_i - M_0 \exp\left(\frac{-i \times \Delta TE}{T_2} \right) \right)^2 \quad \text{where} \quad M_0, T_2 \geq 0 \tag{1.2}$$

The above equation can be solved using a non-negative least square optimization [Lawson 1995]. The stimulated echoes can be accounted for in Eq. 1.2 using the EPG curve instead of a pure exponential. In the EPG formulation we need to estimate the B_1 scale factor to account for the field inhomogeneity. This formulation for a mono T_2 analysis is shown below:

$$\underset{M_0,T_2,B_1}{\arg\min} \sum_{i=1}^{N} \left(y_i - M_0\, EPG\left(i, \Delta TE, T_1, T_2, B_1\right) \right)^2 \quad \text{where} \quad M_0, T_2, B_1 \geq 0 \tag{1.3}$$

The inaccuracies in the application of perfect refocusing pulse is accounted for using a scale factor term in the EPG. For example, a scale factor of 0.95 would imply a 5% error in the refocusing pulse. In Eq. 1.3, the term B_1 is the scale factor correction for the flip angle error (not to be confused with the B_1 in earlier sections). It is usually optimized for only in a definite interval. The flip angle error is considered to be in the range of 0% and 50% in this work (i.e. the scaling factor ranges from 1.0 to 1.5). The T_1 value can be obtained from a quantitative T_1 map. However, it has been shown in earlier work that for white matter assuming a constant T_1 of $800ms$ is good enough [Prasloski 2012]. The effect of stimulated echoes can be clearly seen in data acquired using a multiple echo spin echo sequence. This has been shown via an example using an in vivo brain image in Fig 1.7.

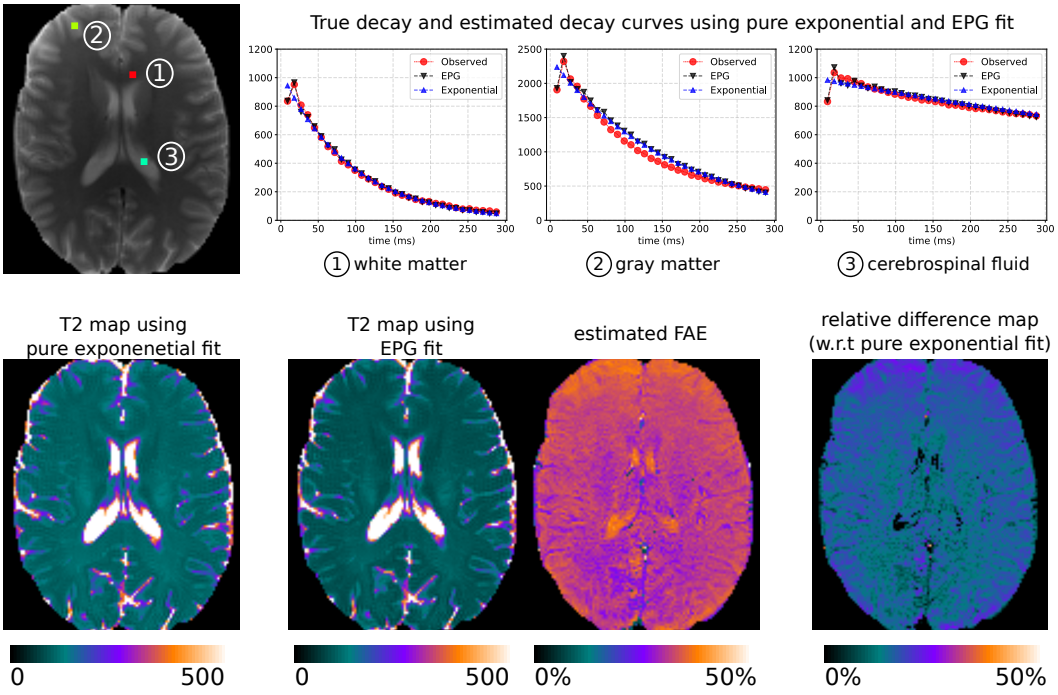

Figure 1.7: Mono T_2 estimations using pure exponential and EPG fitting models are compared here. In general, using pure exponential leads to higher T_2 estimations. The fitting shows that accounting for stimulated echoes leads to better fit of the estimated curve to the observed decay curve.

The data used in this example was acquired using a 2D multi-slice CPMG sequence. The T_2 relaxometry data had 32 echoes with an echo spacing of $9ms$ and repetition time of $3720ms$. A mono T_2 estimation was performed using: *(i)* pure exponential fit (refer Eq. 1.2) and *(ii)* EPG fit (refer Eq. 1.3) accounting for the stimulated echoes. The observed echoes are compared to the estimated echoes using two approaches for three voxels, one in white matter, one in gray matter and one in cerebrospinal fluid (CSF). The observed echoes are not pure exponentials and have stimulated echo effects. This can be observed from the T_2 decay curves of the voxels shown in Fig. 1.7. The second echo signal magnitude of the observed signal is generally higher than the first echo signal magnitude. Using the EPG shows a better fit to the observed curve compared to pure exponential. The T_2 map using pure exponential has a higher T_2 value. For example, the white matter voxel (label 1) has a T_2 value of $94ms$ using pure exponential fit compared to $81ms$ when using the EPG fit model. For a voxel in dense white matter with close to 20% myelin (which has T_2 values in range of 10-50ms), a T_2 value of greater than $90ms$ is higher than expected. The T_2 value for the gray matter voxel (label 2) was higher by around $25ms$ when using pure exponential fit model. The estimated flip angle error (FAE) percentage map is also shown in Fig. 1.7. The relative difference map shown

in Fig. 1.7 was computed as shown below:

$$\text{Relative Difference} = \frac{T_{2_{exp}} - T_{2_{EPG}}}{T_{2_{exp}}} \times 100\%$$

where $T_{2_{exp}}$ and $T_{2_{EPG}}$ are T_2 values estimated using pure exponential and EPG respectively. On comparing the observed and estimated decay curves, it is clear that pure exponentials are not ideal when using FSE sequences. Hence imperfect refocusing after the 180° RF pulse should be factored into the signal model while performing T_2 fittings.

1.2.1 Multiple T_2 analysis

The brain white matter has been shown to possess multiple T_2 water pools. Hence a mono T_2 estimation maps is not enough when we are analyzing T_2 relaxometry data of the brain. This was first reported by [Whittall 1997]. A range of studies suggest that there are primarily two water pools in the brain white matter [MacKay 1994, Whittall 1997, Stanisz 1998]. There is no certain explanation to it, but it might be attributed to the fact that white matter is quite dense and contains tightly packed nerve fibers [Does 2018]. The nerve fibers contain axons and layers of tightly wrapped myelin around it. The myelin water and water associated with axons, intra/extracellular bodies are well separated with respect to their T_2 relaxation times. Myelin has a short T_2 relaxation time compared to other white matter tissues. This has been illustrated in Fig. 1.8.

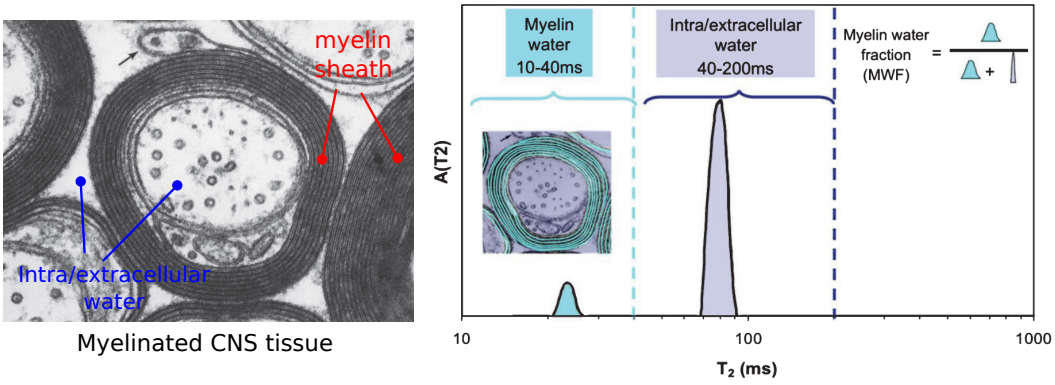

Figure 1.8: (Left) Electron microscope image of myelinated CNS tissue. The myelin sheath surrounds the axons. (Right) T_2 distributions of the myelin and intra/extracellular water are shown here. Image courtesy: [MacKay 2016].

Since the T_2 water pools are well separated, their contributions in a voxel can be quantified using models to analyze the T_2 relaxometry data. The common approach is to quantify the fraction of myelin in a voxel, popularly referred to as myelin water fraction (MWF). MWF has been shown to be an indicator of myelin (and its absence) in brain tissues using histological studies [Laule 2007a].

1.2.1.1 Multi-component T_2 relaxometry model

The most popular method of obtaining the myelin water fraction is a multi-component T_2 relaxometry analysis. The central idea of this model is to consider the observed T_2 relaxometry signal as a (weighted) composition of arbitrary number of exponential decays (or EPG curves [Prasloski 2012]). The fractional contributions of the decay curves with short T_2 values is referred to as the MWF. This interpretation of the T_2 relaxometry signal was proposed by Whittall et al. [Whittall 1989]. The capability of this method to obtain a myelin water fraction was demonstrated on in-vivo brain T_2 relaxometry MRI data [MacKay 1994]. The multi-component T_2 relaxometry model is shown below:

$$s(t_i) = \sum_{k=1}^{M} w_k \exp\left(\frac{-t_i}{T_{2_k}}\right) \tag{1.4}$$

In the above equation, the signal magnitude at each echo is considered to be a weighted combination of M number of T_2 curves. The most popular strategy for choosing the T_2 values of the decay curve is to select logarithmically equally spaced values. The number of T_2 values choice is however arbitrary. But the most popular choice remains as 80 logarithmically spaced points between $10ms$ and $2000ms$ [Laule 2007a, MacKay 2016]. In such a case, there are 80 variables to estimate from far less number of observations. A standard T_2 relaxometry data consists of 32 echoes. Hence this is an extremely ill posed problem. This is usually tackled by introducing regularization terms in the estimation [Graham 1996, Whittall 1997, Laule 2007a]. The choice of a fixed regularization weight is not an appropriate choice. Hence strategies to update the regularization based on the current cost function value is usually adopted to mitigate this issue. Graham et al. discuss this approach in their work [Graham 1996].

Sensitivity to noise

Other than the ill-posed nature of the problem, the high signal to noise ratio (SNR) requirement of this model is another challenge. Graham et al. showed that the ideal scan parameters and SNR requirements for a reliable estimation of short T_2 water fraction using the T2NNLS (refer [Graham 1996]) model from a 32 echo T_2 relaxometry data would be an echo time of $6.5ms$ and a SNR of around 500. The usual echo time used for the T_2 relaxometry data is around $10ms$, for which the SNR requirement was found to be 700 for reliable estimation of myelin water fraction in white matter tissues. Resolution of T_2 peaks from the multi-component T_2 relaxometry analysis is challenging at low SNRs. This has been shown in [Fenrich 2001]. Fenrich et al. fixed the distribution of a T_2 pool and investigated the capability of multi-component T_2 relaxometry analysis at resolving two T_2 pools for varying levels of SNR. Another variable which was factored in the analysis was the separation of the T_2 pools.

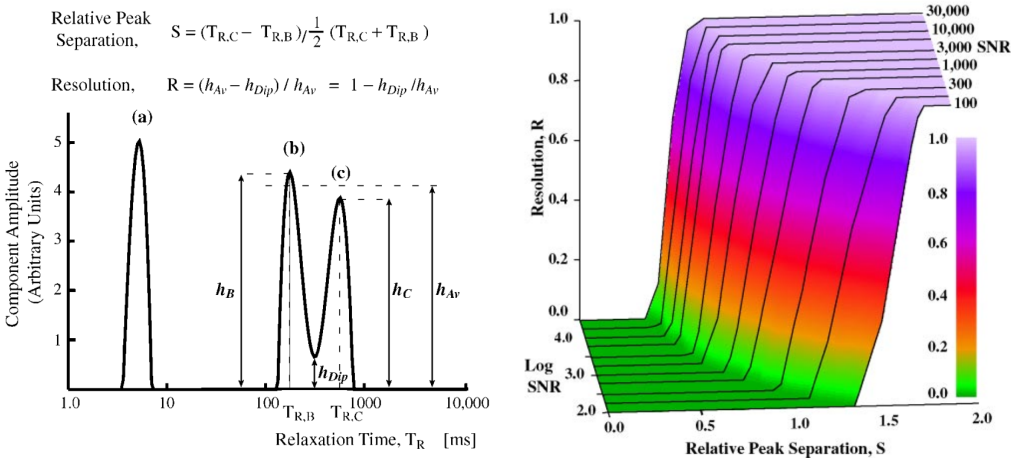

(a) (b)

Figure 1.9: (a)The resolution (R) and separation (S) between the T_2 pools are shown here as defined by [Fenrich 2001]. (b) The resolution capability is shown for a given separation and SNR level. The plot is color coded with respect to the resolution values. It can be seen that greater separation is required for full resolution as the SNR drops. Image courtesy: [Fenrich 2001].

The resolution (R) and separation (S) are illustrated in Fig. 1.9a. A T_2 pool (the short T_2 in this case) was fixed and the resolution and separation characteristics were studied for the other two pools for varying levels of SNR (result shown in Fig. 1.9b). It can be observed from the definition of R, that $R = 1$ ensures complete separation of the T_2 pools. Ideally, we would like to have full resolution between the peaks while using a multi-component T_2 analysis. The usual SNR for in-vivo imaging is 100 (without multiple signal averages). As the plot shows in Fig. 1.9b, we can have a non-zero resolution for a SNR of 100 only at separation values greater than 1.35. This study highlights the challenge that lies with the multi-component T_2 relaxometry model in identifying T_2 pools in close proximity to each other. Although Lancester et al. proposed a three pool model for white matter [Lancaster 2003], studies like [Fenrich 2001] show the underlying complexities which make realizations of such models on in-vivo data with a SNR of around 100. Hence, reliable separation of T_2 pools can only be performed on high SNR T_2 relaxometry data. A higher SNR image can be obtained using multiple signal averages. However, this leads to a longer acquisition time which is not favorable for clinical conditions. Levesque et al. proposed an acquisition scheme for multi-echo T_2 data in 4 min sequence [Levesque 2010a]. However, to maintain the SNR requirements for the multi-exponential fitting, the voxel resolution was maintained at $2{\times}2{\times}7mm^3$. Although the chosen scanning parameters help in reducing the acquisition time while maintaining the required SNR levels for multi-exponential T_2 fitting, it is not appropriate while studying pathologies like MS lesions where lesion dimensions are considerably smaller than the voxel dimensions used in the study.

Table 2 in [Alonso-Ortiz 2015] compares the scan times of popular multiple echo spin echo acquisitions popularly used for myelin imaging.

T_2 threshold for MWF

The multi-component T_2 model requires thresholds on T_2 values for which the signal is considered to be from myelin. In Table 1 of [Lancaster 2003], authors compare the T_2 values used by multiple reports for representing the three pools in white matter: myelin, myelinated axons and mixed pool. The myelin and myelinated axons are stated to have a T_2 value of around $10ms$ and $40ms$ respectively. Whereas MacKay et al. considered myelin to be represented by T_2 decay curves with values in the range of 10-$55ms$ and all decay curves with T_2 curves beyond it belonging to a mixed pool [MacKay 1994]. The T_2 threshold considered for deciding the myelin water fraction also affects its values. An example of this can be observed from Fig. 3 and 4 in [Levesque 2010a], where a change in threshold by $10ms$ leads to visible changes in the myelin water fraction values in various regions of the brain. The authors also observed an increased variability in the inter-scan myelin water fraction measurements when using a 10-$50ms$ threshold compared to 10-$40ms$ threshold. Hence the T_2 threshold value to decide for myelin not only leads to observable changes in MWF, but also affects the inter-scan variability of estimations.

Myelin is not the only brain tissue microstructure information which the multi-echo T_2 relaxometry data can provide. The MS lesion regions have inflammation due to continuous tissue injuries. The inflammation can be seen in FLAIR images. The water accumulation in the MS lesion regions leads to them having a prolonged T_2 relaxation time compared to the normal appearing brain matters. This has been observed in earlier studies where 48 echo T_2 relaxometry data were acquired for MS patients [Laule 2007b, Laule 2007c].

Despite the challenges existing around the multi-component exponential models, Alex Mackay and his group's studies have proved its efficacy in obtaining MWF estimates from T_2 relaxometry data using this method [Whittall 1989, MacKay 1994, Whittall 1997, Laule 2007a, MacKay 2016]. The MWF has been shown to be a reliable indicator of myelin on healthy subjects and MS patient. This was also shown using histology studies on healthy and MS affected brain tissues [Laule 2006]. Among all the limitations, SNR is the most important limitations which needs to be factored in while performing multi-component T_2 relaxometry analysis. A comprehensive discussion on this topic can be found in the review article by Mark D. Does [Does 2018].

1.2.1.2 Multi-compartment T_2 relaxometry models

The multi-component model discussed in the earlier section does not assume anything on the distribution of weights of the T_2 curves. The multi-component exponential fitting is essentially a non-parametric model. The model is based on the knowledge of underlying physiology of the imaged tissues. Elaborative studies using

the multi-component T_2 model on images with high SNR has shown the existence of two distinguishable T_2 pools in human brain white matter (refer Fig. 1.8). The challenges of the non-parametric method of multi-exponential fitting can be addressed using parametric models. The parametric models can deal effectively with the curse of dimensionality associated with the multi-component T_2 models.

The basic idea of the parametric models is to consider multiple T_2 compartments in a T_2 relaxometry MRI voxel. Stanisz et al. proposed a two compartment model where each compartment was modeled as a log-Gaussian probability density function (PDF) [Stanisz 1998]. In another parametric formulation, Raj et al. modeled the T_2 spectrum as weighted sum of two Gaussian PDFs describing the myelin and intra/extra-cellular matter and a delta function describing the CSF [Raj 2014]. The authors performed a simultaneous estimation of weights and parameters of the PDF, and the weight and location of the delta function representing the CSF. The model also included two regularization terms. The first one is a general Tikhonov regularization term. The second regularization term is aimed at obtaining spatial consistency. It is realized using a first difference operator matrix. The weights of the regularization terms are obtained via a semi-supervised method. Although authors used Gaussian PDFs to model the underlying compartments, they chose not to adopt a integration based approach but a matrix based formulation. The authors demonstrated the application of the parametric method on low SNR simulated and in-vivo data (acquired in around 10-26 minutes). Application was shown on MS patients where myelin maps obtained from the proposed parametric model had significantly lower values in lesions compared to normal appearing white matter. However, the myelin maps for the in-vivo data with low SNR (acquired using T_2 prep method) showed elevated MWF in gray matter. The authors have attributed this to the spiral sequence rather than the method used for MWF estimation. The authors have however not commented on the performance of estimation for the parameters other than MWF.

As pointed out by Layton et al. in their work, simultaneous estimation of PDF parameters and weights using NNLS is non-trivial and non-reliable [Layton 2013]. In Figure 7 of [Raj 2014] the authors showed estimated T_2 distributions for deep gray matter and white matter voxel. Both have similar Gaussian PDF parameters. However, the deep brain gray matter tissues should have had a different T_2 spectrum compared to a normal appearing white matter tissue in the brain due to the difference in tissue composition. The challenge of not being able to identify it might lie either with the method, or presence of the information in the data. A cost function (and simulation) analysis can reveal more on whether the method is capable of identify such phenomenons. Both [Stanisz 1998] and [Raj 2014] have assumed pure exponential decay and have not accounted for stimulated echoes.

Akhondi-Asl et al. proposed a method where the T_2 signal at a voxel was considered to be a mixture of three Wald PDFs [Akhondi-Asl 2015]. The three PDFs represented the following compartments: myelin, intra/extracellular water and free water (CSF). The PDF parameters and their associated weights were estimated. Unlike [Stanisz 1998] and [Raj 2014], Akhondi-Asl et al. accounted for the effect of

stimulated echoes in their model using Bloch equations. The PDF parameters were estimated using a variable projection approach [Golub 2003]. Analytical derivatives were obtained to make the estimation faster. The B_1 inhomogeneity scale factor was estimated in a separate step by performing an exhaustive search over a range of feasible values. Synthetic data, in-vivo phantom data and in-vivo brain MRI data was used to evaluate performance of the proposed method for estimating MWF maps. Authors also commented on the ability of this method to obtain superior (smoother and less noisy) MWF maps from 2D Multi-slice CPMG data as compared to multi-component models (on low SNR synthetic and in-vivo brain data). Unlike [Raj 2014], [Stanisz 1998] and [Akhondi-Asl 2015] used an integration based approach. This might be the reason that [Stanisz 1998] and [Akhondi-Asl 2015] did not require any external regularization term (such as the spatial smoothening used in [Raj 2014]) since continuous functions are used to describe the compartments and an integration based method is used to solve for the weights and other parameters. This also relieves the method of accounting for techniques (semi-supervised or otherwise) to update the regularization weight term(s).

1.3 Discussion

Quantitative tissue microstructure information on fast relaxing tissues in brain such as myelin can be obtained from T_2 relaxometry data using parametric and non-parametric analytical models. The non-parametric methods have been shown to be effective in obtaining MWF maps but require high SNR to reliably and accurately estimate myelin content. This makes the data acquisition time longer (multiple signal averages). Estimation of a large number of variables with far fewer observations is also a concern with non-parametric models. Regularization terms can be used for tackling this issue. This requires additional techniques to ensure regularization weights are properly updated so as not to under or over estimate variables. The ability to identify distinct T_2 pools is also a challenge at lower SNR levels. Other than MWF, T_2 relaxometry has been shown to provide information on long T_2 tissues as well. This is encouraging for clinical studies as most brain tissue abnormalities have an increased water level in and around affected tissues (such as edema in MS).

The parametric methods on the other hand estimate much lesser number of parameters and evade the problem with the curse of dimensionality. The simulation studies have shown them to be reliable even at low SNR values. The evaluation of the estimation methods is however critical for the parametric methods. The difficult nature of the estimation for such models has been highlighted by Layton et al. (especially simultaneous T_2 pool parameters and weights estimation) [Layton 2013]. Rigorous cost function analysis can provide more insights into it. It has also been found that accounting for stimulated echoes is important for accurate estimation of tissues with short T_2 relaxation time such as myelin. This can either be performed using various realizations of the EPG algorithm [Prasloski 2012, Layton 2013] or just by using Bloch equations [Akhondi-Asl 2015].

Chapter 2

Multiple Sclerosis

Contents

2.1 Introduction

In this chapter, we shall briefly discuss the understanding of clinical and pathological aspects of multiple sclerosis (MS). This is important for interpretation of the results from any (advanced) MRI analysis model. In terms of appearance, relapse and progress, MS is a clinically and pathologically heterogeneous disease [Tofts 2005]. A healthy nerve fiber has an axon with myelin wrapping around it. Degeneration of myelin marks the onset of MS. Hence, demyelination is a primary indication of MS. The healthy nerve fiber and a nerve fiber with degenerated myelin are illustrated in Fig 2.1. Myelin is a tightly wrapped structure around the axons. It is critical for normal functioning of nerve fibers as it ensures proper transmission of message signals via the axons (refer illustration in Fig. 2.2). Demyelination disrupts the normal transmission capability of signal in nerve fibers thus causing handicap to the patients.

Demyelination exposes the axons to damages from external cellular bodies. Permanent disability due to MS is a result of axonal loss [Tofts 2005, Ferguson 1997]. However, demyelination and axonal loss follow varying trends for different patient groups [Lassmann 2001]. The knowledge of the pathological features of MS can provide potentially valuable insights into understanding of the clinical heterogeneity.

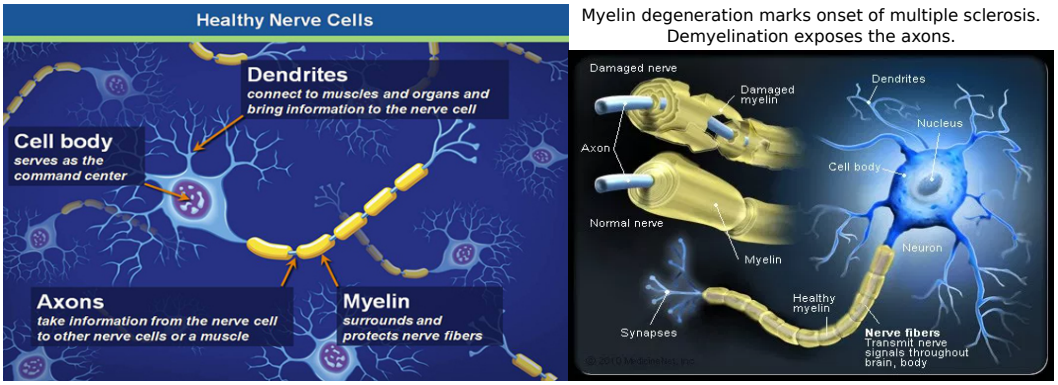

Figure 2.1: The normal nerve fiber and a demyelinated one are illustrated here. Demyelination marks the onset of MS in patients.

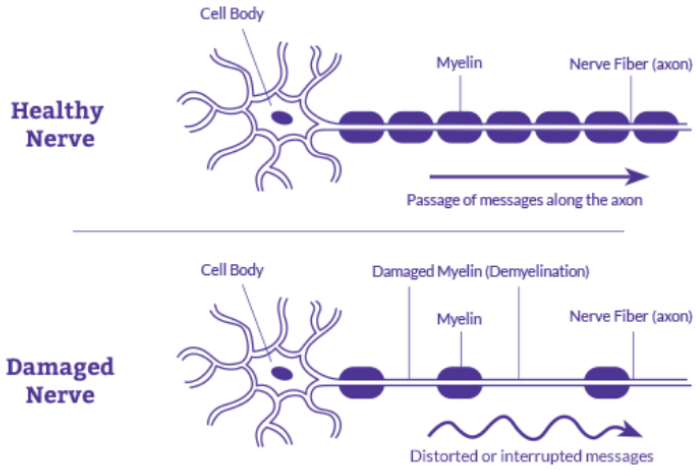

Figure 2.2: Demyelination exposes the axons. This disrupts the capability of nerve fibers to normally transmit messages. Demyelination also exposes the axons to damage from extracellular bodies.

2.2 Clinical trend of MS

Multi-focal lesions and demyelination are widely considered to be a distinguishing feature of MS. Clinically speaking, the progress of MS can be classified into a preliminary (onset of disease) and an advanced stage [Leray 2010]. In preliminary stage a patient is ambulatory and has isolated syndromes. Whereas the advanced stage is characterized by significant ambulatory disability and/or memory impairments. Based on clinical observations, severity of physical/memory disability are scored as per laid guidelines [Kurtzke 1983]. The Expanded Disability Status Scale (EDSS) is used to rate physical disability of a MS patient on a scale of $0-10$, where a score of 0 is *healthy* and 10 is *death due to MS*. Intermediate scores represent varying progression of physical disability. It should be noted that, beyond certain EDSS

scores ($EDSS = 3$ & $EDSS = 6$), the damage caused by MS is considered irreversible [Leray 2010]. Also, the progress from EDSS score of 0 to 3 is highly variable [Leray 2010]. As discussed later, the irreversible damages in MS is mainly attributed to axonal damage and the variability in early onset of MS is due to demyelination, to which every patient responds uniquely. Evidence to support this claim is discussed later in pathological aspects of MS. This is one aspect which adds to the heterogeneity of the disease.

MS in patients is classified based its clinical courses. These are primarily classified into three main categories:

1. Relapsing-remitting MS (RRMS)
2. Primary progressive MS (PPMS)
3. Secondary progressive MS (SPMS).

It shall however be noted that these are the classifications post clinical identification of MS. In most cases, the first episode of MS after which an in-vivo imaging (checkup) might be prescribed, is known as Clinically Isolated Syndrome (CIS). Patients reporting CIS may or may not go on to develop MS. However, patients reporting CIS are considered at a high risk of developing MS, especially if lesions (with characteristics of MS) are identified in brain MRI. Follow-up MRI of CIS patients are studied to conclude on MS progress-type (RRMS or PPMS). The observations are based on the revised McDonald criteria of 2010 [Rovira 2015].

Representative trends of MS classified based on clinical observations are shown in Fig. 2.3. The majority of patients who develop MS post CIS usually develop RRMS followed by SPMS. Few patients directly follow the PPMS pattern. It shall be noted that prior to disease progressions, there are no indications for PPMS, contrary to that of SPMS. MS phenotype descriptions for relapsing and progressive disease are explained in [Lublin 2014].

Definitions of *active* and *progression* of MS as defined in [Lublin 2014] for relapsing and progression phenotype can be found in Table 2.1 and Table 2.2 respectively. Phenotype descriptions for clinical protocol for initial detection or onset of MS is shown in Figure 2.4. The decision whether CIS progresses as RRMS is taken based on follow up MRI scans of the patients who exhibit CIS. Scan intervals may vary from patient to patient based on the neurologist's recommendation. If there active lesions (for definition refer Table 2.1) which follow McDonald's criteria [Rovira 2015], then the patient is considered to be in RRMS phase. RRMS more or less follows pattern shown in Fig 2.3.

However, classifying progressive MS is a more subjective task. Whether progression of MS is PPMS or SPMS is carried out by investigating whether the lesion is active (refer Table 2.2). The activity of lesion is concluded predominantly from MRI scans but the progression of MS is concluded from clinical scores such as EDSS and other clinical evaluations [Kurtzke 1983]. Phenotype description for Progressive MS is shown in Fig 2.5. Fig 2.5 suggests that progressive accumulation of disability

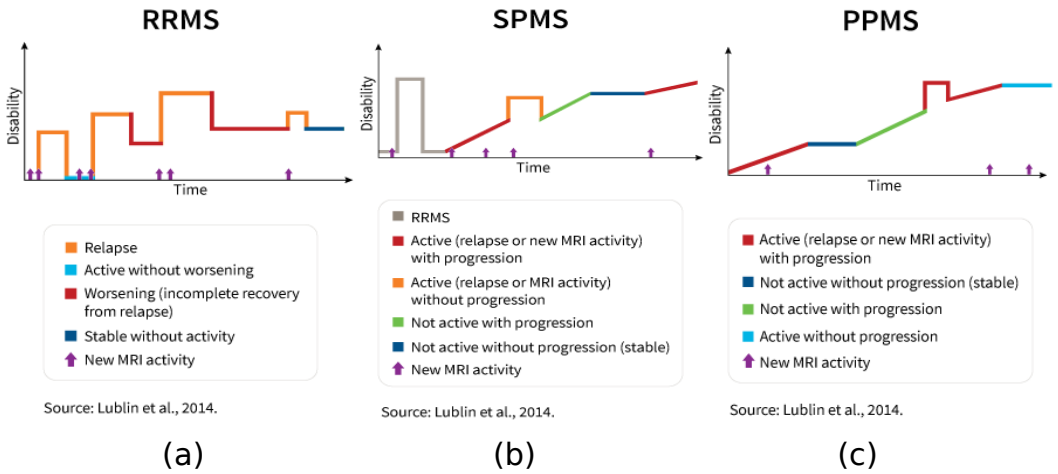

Figure 2.3: (a)RRMS (b)SPMS and (c)PPMS type of MS. Image courtesy: [Lublin 2014]

right after onset suggests PPMS, and progressive accumulation of disability after initial relapse course suggests SPMS. However, there is an uncertainty in identifying the type of progressive MS in patients from clinical point of view. This is attributed to a couple of significant reasons [Lublin 2014].

1. Measuring the progression using clinical observations misses on some subtle indications, either due to frequency of clinical observations taken or variance of human observation.

2. Another important factor is the determination of whether a lesion is active (for definition refer Table 2.2). For this, radiologists rely on MRI scans. For example: although T_2 and Gd-Lesions are indications of active lesions, there is a lack of standardized protocol in place to make quantitative judgments of a lesion being active (or not).

The solution to the second problem may be found in quantitative biomarkers being proposed for the detection of early lesions. This will need understanding of the pathology of MS lesions and addressing them accordingly. However, recent publications from clinicians and radiologists cite lack of confidence on advanced MRI techniques for inferring the biomarkers that indicate activity and progression of a lesion [Rovira 2015, Lublin 2014]. One possible reason might be the lack of specificity and reproducible capability of the methods proposed. This lack of consensus between clinical disability/prediction and quantitative predictions made by MRI is known as *clinico-radiological paradox*.

From the discussion it can be concluded that there are uncertainties in clinical predictions (especially for progression of MS) which can be resolved by providing concrete and reliable inputs from quantitative MRI techniques. Whereas the clinical observations are critical in grading the status of a MS patient, it suffers from the

Active	Determined by clinical relapses and/or MRI activity (contrast enhancing lesions; new or unequivocally enlarging T_2 lesions assessed at least annually); if assessments are not available, activity is indeterminate.

Table 2.1: Definition of Active for Relapsing MS

Active	Determined by clinical relapses assessed at least annually and/or MRI activity contrast enhancing lesions; new and (such as unequivocally enlarging T_2 lesions).
Progression	Measured by clinical evaluation, assessed at least annually. If assessments are not available, activity and progression are *indeterminate*.

Table 2.2: Definition of Active and Progression for Progressive MS

drawback of being subjective. Quantitative medical imaging techniques can help in making this procedure more objective. This becomes more important because based on the status of the MS patient, therapy is provided. Correct MS therapy at a correct time can modify the time-line of the disease.

2.3 Pathological features of MS

Pathological features of MS are quite heterogeneous which has wide implications on diagnosis and therapy of the disease. Demyelination and multifocal lesions are distinguishing features of MS pathology. Demyelination is followed by axonal destruction. It is a primary event, but axonal losses can not be overruled completely in the primary stages of the disease. As mentioned in the previous section, axonal losses cause irreversible damage. Based on the clinical trends' study, we can thus associate PPMS with a condition where there is demyelination and axonal losses (at high rate) simultaneously from the onset of MS. Likewise, when there is only demyelination in

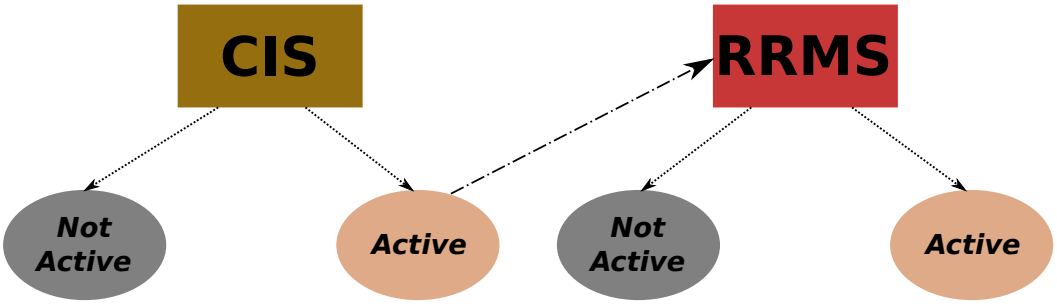

Figure 2.4: MS Phenotype for Relapsing Disease [Lublin 2014]

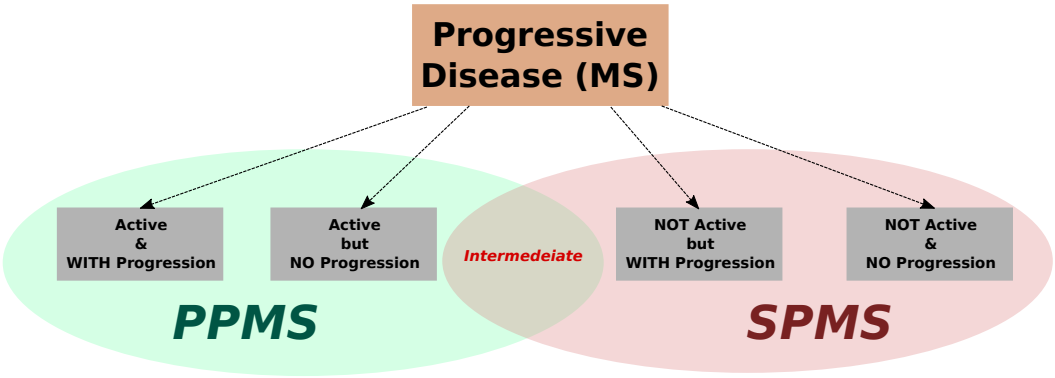

Figure 2.5: MS Phenotype for Progressive MS [Lublin 2014]

the primary stage (or onset) of MS, a patient shall display symptoms corresponding to RRMS (refer Fig 2.3). Hence by monitoring the demyelination and axonal losses, assertive assumptions can be made whether the progression of MS in a patient will follow RRMS (followed by SPMS) or PPMS. This can be a significant information from the MS therapy point of view where it shall be noted that inflammation and demyelination *may be* reversible unlike axonal damage [Lassmann 2001].

There is evidence in favor of the hypothesis that pathology of demyelination and inflammation varies among different patient subgroups [Lassmann 2001]. It has been shown in [Leray 2010] that MS is a two stage disease, and rate of progress of a patient from EDSS score of 0-3 (onset of MS) is highly variable. In contrast, rate of progress from EDSS score of 3-6 is fairly consistent. Observations from [Leray 2010] are shown in Fig 2.6. It might be helpful to recall here that, [Leray 2010] states that EDSS scores of 3 & 6 are stages beyond which damages caused are irreversible. The heterogeneous nature of the MS onset can be attributed to different demyelination (or inflammation) pathogenetic pathways followed by patient subgroups.

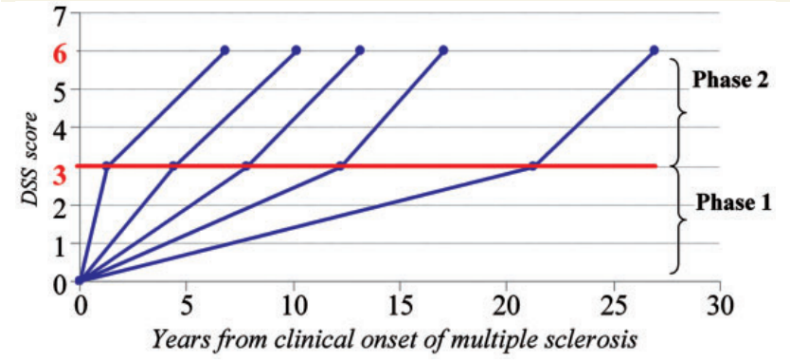

Figure 2.6: Disability progression during Phase 2 (mean time from DSS 3 to DSS 6) in five subgroups defined according to the duration of Phase 1 (mean time from multiple sclerosis clinical onset to DSS 3) in the 718 multiple sclerosis patients who had reached both DSS 3 & DSS 6. Image courtesy: [Leray 2010]

2.3.1 Pathology of demyelination

Demyelination is the most prominent activity in the primary stage of Myelin. Demyelination is accompanied by inflammation too. Inflammation activity during the primary stage of MS will be discussed later. Axons, nerve cells and astrocytes are also affected during active demyelination, but to a much lesser degree (unless patient starts exhibiting PPMS symptoms). Damage to astrocytes are critical because they are responsible for

1. Providing critical support for blood-brain barrier maintenance.
2. Promoting myelinating activity of oligodendrocytes. Oligodendrocytes are critical in the creation of myelin sheaths.

Axonal damages during active demyelination are mainly attributed to:

1. Macrophage toxins.
2. Direct effect of cytotoxic T-cells.

In [Lassmann 2001] authors propose possible pathogentic pathways leading to demyelination in MS patients (based on their patient subgroup study):

1. *Macrophage mediated.* In this case, there might be demyelination also due to toxic products produced by the macrophages.
2. *Antibody mediated.*
3. *Distal Oligodendrogliopathy & Apoptosis.* Due to degenerative changes in distal processes, in particular those of periaxonal oligodendrocytes (distal oligodendrogliopathy), followed by apoptosis. Apoptosis refers to automatic death of cells due to some reason. This is however caused by factors like ischemia or toxic viruses.
4. *Primary oligodendroglia degeneration.* This is a metabolic defect. Absence of oligodendrocytes diminishes regeneration of myelin sheaths. Observation of this phenomenon in MS patients has been restricted only to patients with primary progressive disease [Lucchinetti 1999].

Hence, we observe that most of the factors are dependent heavily on the immune system of a patient. Hence heterogeneity of response of patients to demyelination vary across patient subgroups. Based on pathology, lesions can be classified into inactively or actively demyelinating. For definitions refer to Table 2.3.

2.3.2 Pathology of MS inflammation

Pathology of inflammation in MS lesions is consistent with a T-cell-mediated immune reaction[Lassmann 2001]. Such a T-cell mediated immune reaction has two important consequences:

1. Recruitment of hematogenous macrophages

2. Activation of microglia.

Microglia act as the first and main form of active immune defense in central nervous system. Although most evidences indicate towards an inflammation driven by $Th1$ mediated autoimmune response, there is substantial evidence against it too [Hohlfeld 1997]. Authors in [Lassmann 2001] show evidence to argue in favor of the point that MS inflammation is more complicated than a pure $Th1$ autoimmune response, and is rather a combination of $Th1$, $Th2$ and $Tc1$ autoimmune response[1].

Feature	**Active**	**Inactive**
Macrophage infiltration	Yes	May or may not be
Immunoreactive	for all myelin protein Including minor ones	For minor protein only
Others		Demyelinated/Remyelinated

Table 2.3: Definition of active and inactive MS lesions in terms of demyelination [Lassmann 2001, Brück 1995]

2.3.3 Pathology of Axonal Loss

Axonal damage is critical as it is irreversible. Axonal injury in MS occurs in two stages [Lassmann 2001]:

1. During active stage of myelin degeneration (refer Table 2.3)

2. Continued axonal degeneration in active MS plaques. This stage kicks in only if there is no remyelination of axons post initial myelin-degeneration and inflammation.

The extent of axonal injuries caused during the first phase is correlated to the number of macrophages and class-I-restricted T cells in the lesion. The later stage of axonal injury is attributed to the inability of oligodendrocytes in remyelinating the actively demyelinating lesions. The axonal damage in this stage can be quite aggressive.

The axonal loss thus depends on the extent of remyelination and inflammation of the lesions during active demyelination of lesions. Hence the heterogeneity in susceptibility of individual patients is also an important factor for axonal injuries in lesions.

[1] $Th1$: T helper 1 cells. $Th2$: T helper 2 cells. $Tc1$: Class I-restricted cytotoxic T cells

2.4 In-vivo imaging of MS lesions using MRI

Magnetic resonance imaging (MRI) has played a critical role in detection and monitoring of MS in patient [Rovira 2013, Rovira 2015, Barillot 2016]. Evidence for appearance of new lesions in MS is considered to be a crucial parameter for deciding the clinical course the patient needs to take. Another important clinical indicator is the presence or absence of active lesions in MS patients. MRI has emerged as a leading in-vivo imaging technique for monitoring MS lesions. The MS lesions have different contrast than the normal appearing brain tissues in MRI. Based on the type of MRI measurement performed, the MS lesions are either hyper-intense or hypo-intense compared to the intensity of normal appearing brain tissues. Use of contrast agents (such as gadolinium) allows identifying lesions undergoing active blood brain barrier breakdown. These are also commonly referred to as active lesions (early stage lesions). Presence of active lesions is an important clinical observation. Four different MRI measurements for the same subject with a MS lesion is shown in Fig. 2.7. The MS lesion in the subject is highlighted using red arrow.

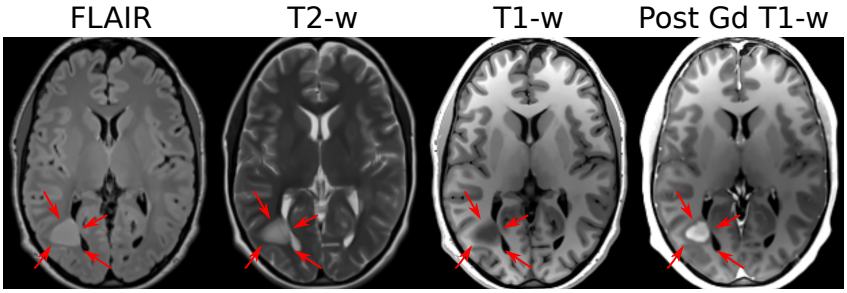

Figure 2.7: (Left to right) Fluid-attenuated inversion recovery (FLAIR). T_2 weighted image. T_1 weighted image. T_1 weighted image acquired post gadolinium injection.

The fluid-attenuated inversion recovery (FLAIR) image is similar to a T_2 weighted image (transverse relaxation), except that the signal from free fluids is suppressed. The edema in the lesion affected region leads to its higher contrast than the surrounding and contra-lateral normal appearing white matter tissues. The lesion region appears brighter than the normal appearing white matter regions in the T_2 weighted images as well. However, unlike the FLAIR image there is a greater contrast between the normal appearing white matter tissue and the gray matter and the cerebrospinal fluids appear bright as well. Free fluids have the highest contrast on a T_2 weighted image. The edema is relatively less bright than the CSF due to its (relatively) smaller mobility.

2.5 Discussion

From the existing literature on clinical trends of MS and pathogenetic ways of its onset and progression, we can conclude that MS is a highly heterogeneous disease.

The uncertainty in deciding the category to which a MS patient belongs based on clinical observations may be attributed to the heterogeneity in susceptibility of individual patients towards MS progression (in pathogenetic ways). The heterogeneity in pathogenetic progression may be due to the fact that the ability to cope up with degenerating aspects of onset of MS is heavily dependent on immune response of the patient. Since there is no clinically-accepted quantitative in-vivo imaging method to quantify initial onset of MS (such as extent of demyelination, glial-cell activity, etc.), prescription drugs to inhibit onset of MS at a very early stage is an existing challenge [Rovira 2015, Bakshi 2008]. Although emerging qMRI techniques have received positive acclamation from the radiologists, due to lack of specificity of these techniques they are not in clinical use at present [Rovira 2015].

But from a single MS lesion point of view, stage-wise progression has been established [Lassmann 2001, Leray 2010] where each stage may be represented by a set of defined degeneration characteristics [Lassmann 2001, Van Waesberghe 1999, Laule 2007a]. This fact is a motivating factor to investigate biomarkers which can give an overall sense of MS disease progression in a MS patient, as well as provide insights into the microstructure information of individual lesions.

Advanced MRI techniques which can provide quantitative information of brain tissues (popularly) include diffusion MRI, Magnetization Transfer (MT), and relaxometry imaging technique. The standard MRI techniques in clinical practice today include T_2 & T_1 weighted imaging methods. Authors in [Van Waesberghe 1999] discuss how the advanced MRI techniques compare to standard MRI-techniques with respect to histology reports of axonal damage. The study was done for a population of early stage lesions, actively progressing lesions and lesions in advanced stages of MS. T_2 weighted images are very sensitive to detection of lesions. Among the T_2 visible lesions, axonal density varied between $0-100\%$. Hence, a standard T_2 weighted image lacks specificity in terms of explaining axonal density in a lesion, which is an important marker for the disease progression. But the high sensitivity of T_2 images with respect to lesion detection makes it useful for detecting lesions in early stages. This high sensitivity of T_2 can also be explained from the fact that T_2 predominantly reflects the changes that occur in NAWM (which bear early degenerations in MS). T_1 hypo-intensity and MTR shared similar and strong correlation scores with the degree of axonal density. MT is however more sensitive because its measurement reflects the loss of membrane integrity. Thus unlike T_1, MT also reflects changes in WM (& hence demyelination). Authors in [Van Waesberghe 1999] show that MT shows higher correlation strength with axonal loss than with myelin density for active lesions. For demyelination, Myelin Water Fraction (MWF) has been shown as an effective biomarker based on histology studies [MacKay 2006, Laule 2007a].

Multi-exponential methods for T_2 Relaxometry MRI have been shown to provide information on myelin content in the brain tissues [MacKay 2016, Laule 2007b, Laule 2007c, Levesque 2010b, Laule 2007a]. Earlier work has shown that there are multiple (and distinct) T_2 pools in whiter matter tissues [Whittall 1997]. This has been illustrated in Fig. 2.8. The edema in MS lesions are observed to have a T_2 value higher than the intra/extracellular water T_2 pool shown in Fig. 2.8

[Laule 2007b, Laule 2007c]. In this thesis we propose models and the estimation framework to estimate tissues with short, medium and high T_2 relaxation times in a MRI voxel from low SNR T_2 relaxometry MRI data.

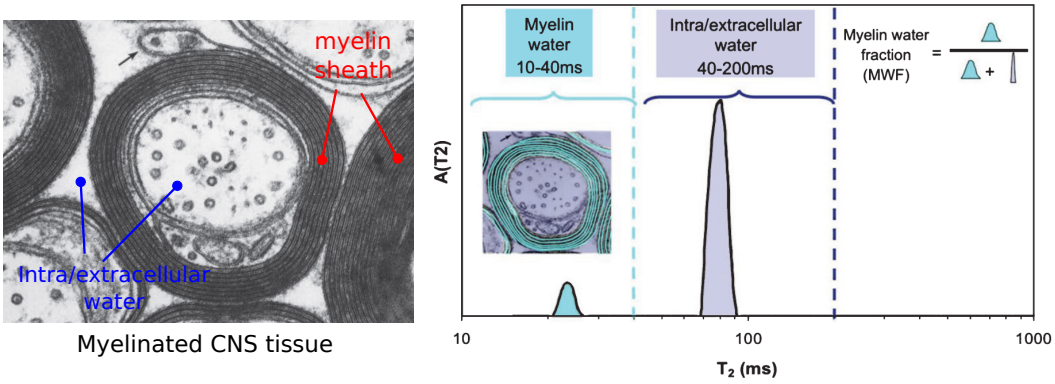

Figure 2.8: (Left) Electron microscope image of myelinated CNS tissue. The myelin sheath surrounds the axons. (Right) T_2 distributions of the myelin and intra/extracellular water are shown here. Image courtesy: [MacKay 2016].

Chapter 3

Gaining insights into brain tissues using multi-compartment T_2 relaxometry MRI

In this thesis two realizations of parametric T_2 relaxometry models and their parameter estimation framework are proposed and analyzed. Each tissue in the brain is considered to be composed of three compartments with tissues having: short T_2, medium T_2 and high T_2 relaxation times. These will henceforth be referred to as short T_2, medium T_2 and high T_2. The objective of the proposed models is to obtain quantitative estimates of the fraction of tissues belonging to each of these compartments present in a T_2 relaxometry MRI voxel. This is illustrated in Fig. 3.1.

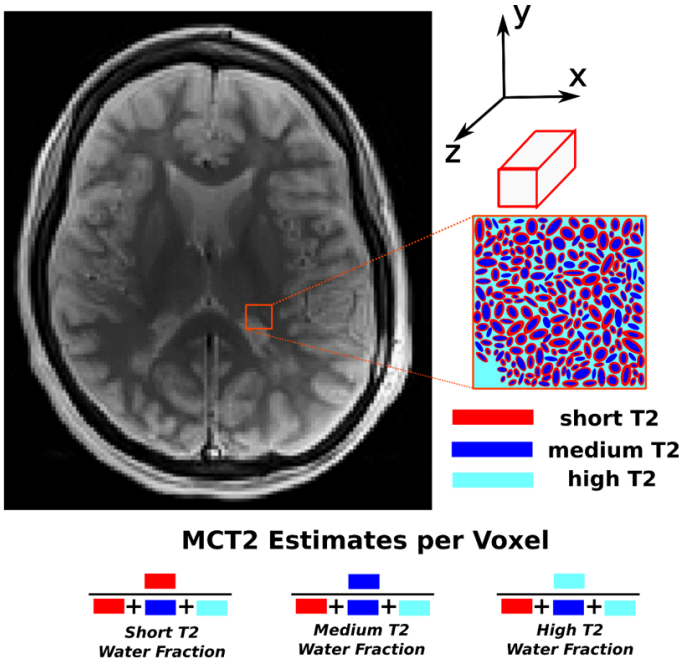

Figure 3.1: The idea of the multi-compartment T_2 relaxometry model is illustrated here. The objective is to obtain robust and reliable short T_2, medium T_2 and high T_2 water fraction maps from a T_2 relaxometry MRI data.

The short T_2 water fraction map provides information on myelin and highly

myelinated axons in the voxel. The medium T_2 water fraction provides information on a mixed pool comprising intra and extracellular matters in the voxel. The high T_2 water fraction is an estimate of the fraction of the voxel containing freely moving water, which can be CSF and long T_2 components such as edema.

The contributions in this thesis have been divided into two parts: *(i)* Methods and *(ii)* Applications.

Methods

In chapter 5 we present a multi-compartment T_2 relaxometry model where each compartment is represented using Gaussian PDFs. The difficult nature of simultaneous estimation of PDF parameters and their weights was shown by studying the cost function on synthetic data for varying levels of SNR. In this chapter, we decided to fix the PDF parameters based on the T_2 pool descriptions provided in earlier studies. The weights of short T_2, medium T_2 and high T_2 compartment PDFs are estimated in this framework. The stimulated echoes were accounted for using the EPG algorithm. The flip angle error percentage is also estimated. The method was validated on T_2 relaxometry data of a synthetic phantom and two in-vivo phantoms. The repeatability of the proposed method was evaluated on healthy controls. The water fraction maps were observed for a MS patient case.

In chapter 6 we proposed a multi-compartment T_2 relaxometry model using gamma PDFs. In this chapter we evaluate the possibility of estimating PDF parameters along with their weights. Based on the cost function evaluation, we found that estimation of the medium T_2 PDF mean is feasible (although difficult). We estimated the PDF parameters and their weights in a variable projection framework. Similarly to chapter 5, stimulated echoes were accounted for by estimating the flip angle error percentage. The model was validated on synthetic and in-vivo phantom data with known ground truth. Repeatability of the estimated water fractions were evaluated on four healthy controls. The MS patient study revealed that the estimated medium T_2 PDF parameter provided useful insights into the lesions. The short T_2 water fraction map indicated demyelination lesion affected regions.

Applications

In chapter 7 we observed the longitudinal evolution of multi-compartment T_2 relaxometry biomarkers in regions of lesions undergoing active blood brain barrier breakdown and the inactive regions of the lesions in 10 patients with clinically isolated syndrome over a period of three years. The biomarkers were obtained using the method proposed in chapter 5. A substantial part of this chapter was to evaluate the performance of the method on T_2 relaxometry data acquired in low acquisition time ($<$ 7 minutes). We designed synthetic phantom experiments to compare the performance of the method on T_2 relaxometry data acquired with standard protocol parameters and with that of data acquired under clinical settings (short acquisition

time). There were several important observations made by studying the evolution of the water fractions in these regions. It was observed that the active lesions regions showed activity latest till 9 months from the baseline scan. We also observed significant differences in the short T_2 and high T_2 water fractions values between the active and inactive lesion regions. Traditionally studies have focused only on evolution of the short T_2 components in the tissues which is an indicator of myelin. However, our study emphasizes on the importance of interpreting the changes in the short T_2 component in conjunction with the changes observed in the representation of other T_2 compartments in the lesions.

In the second application described in chapter 8 we address a challenging and relevant clinical problem. Reports on the issue of gadolinium retention in tissues due to its repeated usage have been on an increase in the recent years. Moreover, usage of gadolinium contrast agent is not possible for patients with renal complications. However, gadolinium contrast agents play an important role in understanding the status and progress of neurodegenerative diseases such as MS. We proposed a method to identify gadolinium enhanced regions in MS lesions using tissue microstructure information obtained from T_2 relaxometry and diffusion MRI data. This chapter had two important observations. The tissue microstructure information obtained from T_2 relaxometry and diffusion MRI data complement each other. The experiment on a test case demonstrated the potential of the proposed framework in detecting active regions in the MS lesions without using gadolinium contrast agent injection.

Chapter 4

Résumé en français

Contents

4.1 Contexte

La mesure de la propriété de relaxation T_2 en imagerie par résonance magnétique (IRM) est intéressante car elle est caractéristique de la composition de la substance mesurée. Il s'agit de plus d'une mesure quantitative, c'est à dire ne variant pas ou peu d'un examen à l'autre. La mesure du signal pondéré T_2 a été proposée par Hahn en utilisant la méthode spin echo [Hahn 1952]. Dans la méthode classique d'écho de spin, un seul écho est obtenu par l'application d'une impulsion de refocalisation après l'impulsion radio fréquence (RF) initiale (donc un seul point sur la courbe de relaxation T_2). Cependant, plusieurs impulsions de recentrage peuvent être appliquées après l'impulsion RF successivement pour obtenir le signal de désintégration T_2 à plusieurs temps d'écho [Carr 1954]. Cette technique est communément appelée imagerie par résonance magnétique relaxométrie T_2. Les données communément appelées de relaxométrie T_2 correspondent á différentes valeurs le long de la courbe de relaxation T_2 de l'image à plusieurs temps d'écho.

L'analyse la plus simple consisterait à adapter une courbe exponentielle unique (ou une courbe de graphe de phase d'écho (EPG) représentant les échos stimulés [Crawley 1987]) aux points de donnés acquis pour chaque voxel. Le taux de décroissance de cette courbe nous fournirait des informations sur les constantes transversales de relaxation pour le voxels. Ceci est souvent appelé analyse mono-exponentielle. Cependant, il a été démontré que la matière blanche du cerveau possède plusieurs classes de tissus ayant différents temps de relaxation T_2. Par conséquent, une carte d'estimation mono T_2 ne suffit pas lorsque nous analysons les données relaxométrie T_2 du cerveau. Ceci a été rapporté pour la première fois par [Whittall 1997]. Une série d'études suggère qu'il existe principalement deux compartiments d'eau dans la matière blanche ducerveau [MacKay 1994, Whittall 1997, Stanisz 1998]. Ceci pourrait être attribué au fait que la matière blanche est assez dense et contient des fibres nerveuses serrées et empactées [Does 2018].

Les fibres nerveuses contiennent des axones et des couches de myéline étroitement enveloppées autour de lui. L'eau de la myéline et l'eau associée aux axones, aux corps intra/extracellulaires sont donc séparées en terme de temps de relaxation T_2. La myéline a un court temps de relaxation T_2 par rapport à d'autres tissus de la matière blanche. Ceci est illustré dans la Fig. 4.1. Comme les compartiments de T_2 sont bien séparés, leurs contributions dans un voxel peuvent être quantifiées à l'aide de modèles pour analyser les données relaxométrie T_2. L'approche commune consiste à quantifier la fraction de la myéline dans un voxel, communément appelée fraction d'eau de la myéline (MWF) [MacKay 1994]. Il a été montré que le MWF est un indicateur de la myéline (et de son absence) dans les tissus cérébraux à l'aide d'études histologiques [Laule 2007a].

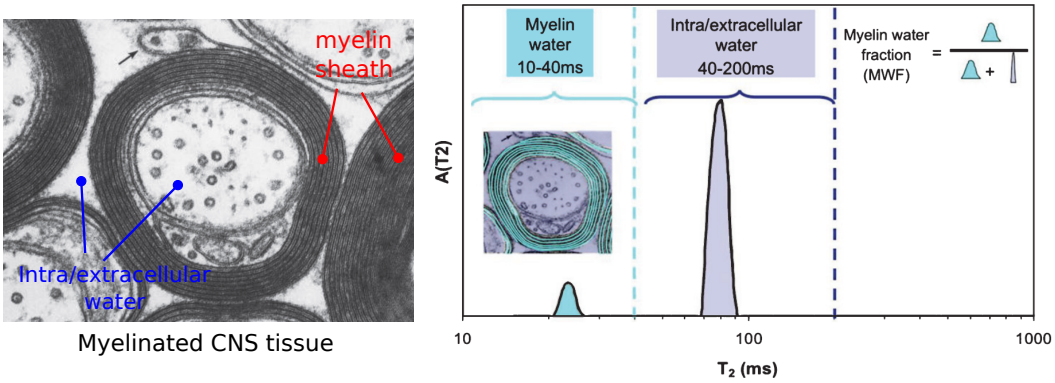

Figure 4.1: (Gauche) Image au microscope électronique de tissus du système nerveux central montrant la myéline enveloppant les axones. (Droite) Distributions T_2 de la myéline et des tissus intra/extra cellulaires. Image extraite de [MacKay 2016].

Dans cette thèse, deux modèles paramétriques de relaxométrie T_2 et leur cadre d'estimation de paramètres sont proposés et analysés. Les tissus dans le cerveau sont considéré comme composés de trois compartiments ayant des propriétés différentes : court, moyen et long temps de relaxation T_2. L'objectif des modèles proposés est d'obtenir des estimations quantitatives de la fraction de tissus appartenant à chacune de ces composantes présentes dans un voxel de relaxométrie T_2 en IRM. Ceci est illustré dans la Fig. 4.2.

La carte de fraction de T_2 court fournit des informations sur la myéline et les axones fortement myélinisés dans le voxel. La fraction de T_2 intermédiaire fournit des informations sur un compartiment mixte comprenant les tissus intra et extra-cellulaires dans le voxel. La fraction de T_2 haut est une estimation de la fraction de l'eau se déplaçant librement, par exemple du CSF ou encore un œdème.

Les contributions de cette thèse ont été divisées en deux parties: (1) méthodes, et (2) applications.

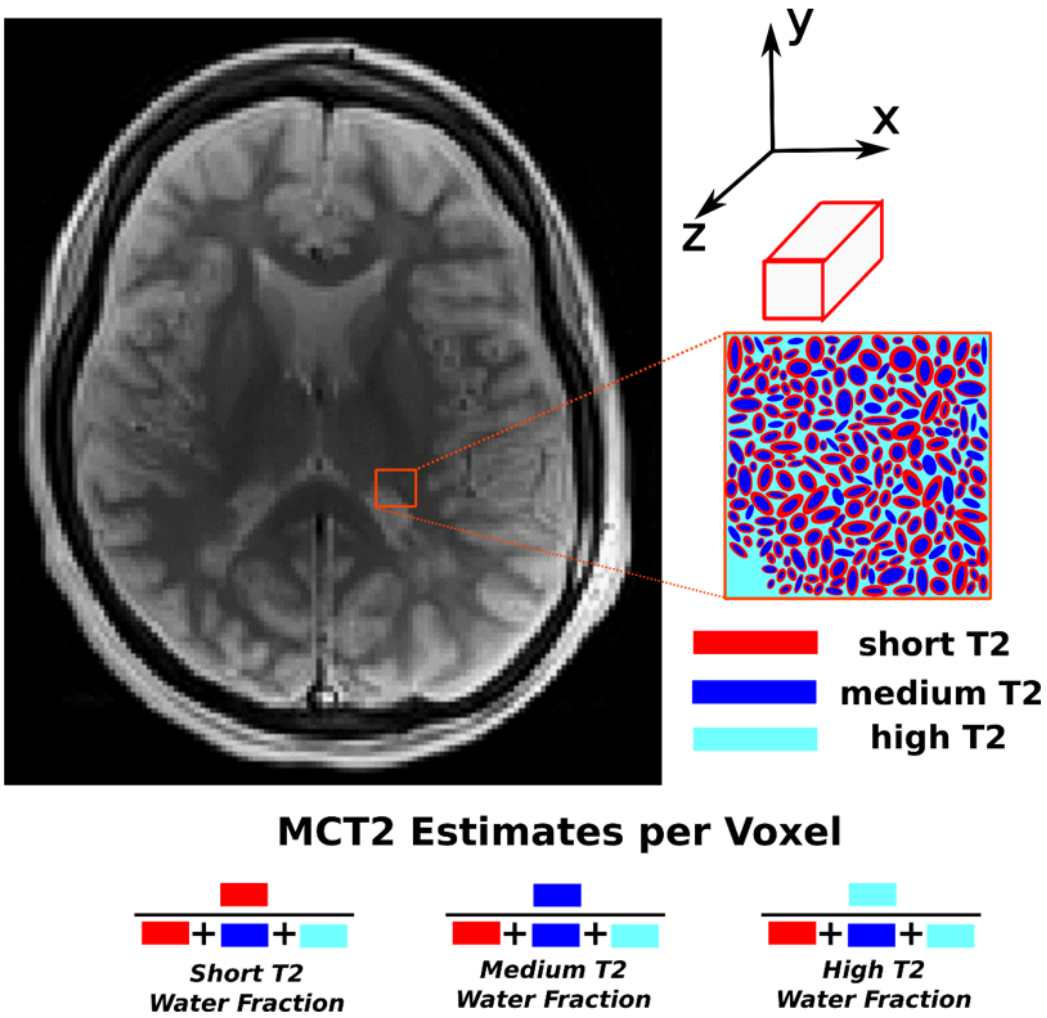

Figure 4.2: Idée générale des modèles multi-compartiment T_2 de relaxométrie. L'objectif est d'obtenir de manière robuste les fractions de trois compartiments T_2: court, moyen et long T_2, et ce à partir d'images cliniques de relaxométrie.

4.2 Méthodes

Chapitre 5

Dans ce chapitre, nous présentons un modèle relaxométrie T_2 multi-compartiment où chaque compartiment est représenté à l'aide d'une densité de probabilité (PDF) Gaussienne. L'estimation simultanée des paramètres des PDFs et leurs poids est étudiée et sa difficulté démontrée par l'étude de la fonction de coût sur des données synthétiques pour différents niveaux de bruit. Dans ce chapitre, nous proposons donc de fixer les paramètres des PDFs en se basant sur les descriptions de compartiments T_2 fournies dans des études antérieures. Le poids des compartiments T_2 court, moyen et long sont donc estimés dans ce cadre. Les échos stimulés dûs à une acquisition

imparfaite sont pris en compte à l'aide de l'algorithme de l'EPG. La méthode a été validée sur les données de relaxométrie T_2 d'un fantôme synthétique et deux fantômes in-vivo. La répétabilité de la méthode proposée a été évaluée sur des sujets sains. Les cartes de fraction de chaque compartiment ont été observées pour un cas de patient atteint de sclérose en plaques.

Chapitre 6

Dans ce chapitre, nous proposons un modèle relaxométrie T_2 multi-compartiment où chaque compartiment est représenté à l'aide d'une densité de probabilité (PDF) Gamma. Nous évaluons la possibilité d'estimer les paramètres des PDFs ainsi que leurs poids. Basé sur l'évaluation de fonction de coût, nous avons trouvé que l'estimation de la moyenne de la PDF pour le compartiment T_2 intermédiaire est possible (bien que difficile). Nous avons estimé ce paramètre etles fractions de chaque PDF dans un cadre de projection de variable [Golub 2003]. De manière similaire au chapitre 4, les échos stimulées sont pris en compte par la méthode EPG. Le modèle a été validé sur des données synthétique et fantômes in vivo où la réalité terrain est connue. La répétabilité des fractions estimées ont été évaluées sur quatre sujets sains. L'étude de patients souffrant de sclérose en plaques (SEP) a révélé que le paramètre estimé pour le compartiment T_2 moyen fournit des indications utiles sur les lésions. La démyélinisation des lésions est par ailleurs bien visible sur les cartes de poids du compartiment T_2 court.

4.3 Applications

Chapitre 7

Dans ce chapitre, nous avons observé l'évolution longitudinale des biomarqueurs issus de relaxométrie T_2 multi-compartiment dans les régions de lésions SEP où la barrière hémato-encéphalique est en cours (partie de lésion active) ou terminée (partie de lésion inactive) chez 10 patients atteints d'un syndrome cliniquement isolé sur une période de trois ans. Les biomarqueurs ont été obtenus à l'aide de la méthode proposée au chapitre 5. Une partie substantielle de ce chapitre a consisté à évaluer la performance de la méthode sur les données T_2 relaxométrie acquises en temps d'acquisition faible ($<$ 7 minutes). Nous avons conçu des expériences sur des fantômes synthétiques pour comparer les performances de la méthode sur les données T_2 relaxométrie acquises avec des paramètres de protocole standard et avec celles des données acquises dans un contexte clinique. Plusieurs observations importantes ont été faites en étudiant l'évolution des fractions T_2 dans ces régions. Il a été observé que les régions actives de lésions ont montré une activité plus tard jusqu'à 9 mois de l'analyse de base. Nous avons également observé des différences significatives dans les valeurs des fractions T_2 court et T_2 élevées entre les régions de lésion active et inactive. Traditionnellement, les études n'ont porté que sur l'évolution des composantes T_2 court dans les tissus, qui est un indicateur de la

myéline. Cependant, notre étude met l'accent sur l'importance d'interpréter les changements dans la composante T_2 court en conjonction avec les changements observés dans la représentation des autres compartiments T_2 dans les lésions.

Chapitre 8

Dans la deuxiéme application, nous avons abordé un probléme clinique récent et important. Les rapports sur la question de la rétention gadolinium dans les tissus dus à son utilisation répétée ont augmenté ces dernières années. En outre, l'utilisation de l'agent de contraste gadolinium n'est pas possible pour les patients souffrant de complications rénales. Cependant, les agents de contraste gadolinium jouent un rôle important dans la compréhension de l'état et de la progression des maladies neurodégénératives telles que la SEP. Nous avons donc proposé dans ce chapitre une méthode pour identifier les régions prenant le contraste gadolinium en utilisant uniquement l'information de microstructure tissulaire obtenue par des données d'IRM de relaxométrie et de diffusion de T_2 (donc sans injection de produit de contraste). Ce chapitre a permis deux observations importantes. Tout d'abord, les informations de microstructure tissulaire obtenues à partir des données T_2 relaxométrie et diffusion IRM se complètent. Ensuite, l'expérience sur un cas de test a démontré le potentiel du cadre proposé pour la détection des régions actives dans les lésions SEP sans utiliser l'injection d'agent de contraste gadolinium.

4.4 Conclusion

Les remarques concluantes des observations des méthodes et des applications proposées sont abordées dans ce chapitre. Nous y présentons également un certain nombre de perspectives qui peuvent être poursuivies en tant que travaux futurs basés sur les conclusions de cette thèse.

Part II

Methods

Chapter 5

Multi-compartment T_2 relaxometry model using Gaussian distributions

Contents

5.1 Introduction

In this chapter, we propose a method for computing water fractions corresponding to fast−, medium− and slow− decaying components with respect to T_2 relaxation times. This method is applied on T_2 relaxometry MRI data acquired using 2D multislice Carr-Purcell-Meiboom-Gill (CPMG) sequence. In this estimation framework, the T_2 space is modeled as a weighted mixture of three continuous probability density functions (PDF) representing the three T_2 compartments. Imperfect refocusing

(due to the B_1 inhomogeneities) leads to errors in T_2 estimation due to stimulated echo effects [Crawley 1987]. We used the extended phase graph (EPG) algorithm to account for these stimulated echoes [Prasloski 2012]. Since the T_2 space is modeled as a weighted mixture of three continuous PDFs representing the three components, the proposed model does not include any regularization on the water fractions. The estimated weights of each compartment provide a quantitative estimate of the tissue microstructure in a voxel. The multi-compartment T_2 relaxometry signal model is explained in Section 5.2.1.

For such parametric models, the robustness and accuracy of the implementations to simultaneously estimate the weights and parameters of the distributions was found to be non-trivial and not reliable [Layton 2013]. Simulations are performed for varying levels of signal to noise ratio (SNR) to evaluate the feasibility of simultaneous estimation of weight and PDF parameters for the signal model in Section 5.2.2. Based on the observations of the cost function analysis, we setup the problem in Section 5.2.3. The flip angle error is estimated numerically. In section 5.3.1, 5.3.2 and 5.3.2 we described experiments to validate the proposed method using synthetic phantom and in-vivo phantom data experiments. In section 5.3.4 the experiment to evaluate the repeatability of the method on test-retest data of in-vivo MRI brain data of healthy subjects is discussed. The analysis on multiple sclerosis (MS) case application has been discussed in section 5.3.5.

5.2 Method

5.2.1 Signal model

We model the T_2 space as a weighted mixture of three continuous PDFs representing the three T_2 relaxometry compartments. The compartments represent tissues with short, medium and high T_2 relaxation times. The weight of the $j-$th distribution is denoted by w_j. The weights are normalized such that $\sum_j w_j = 1$. Hence, the signal of a voxel at the $i-$th echo time (t_i) is given as:

$$s\left(t_i\right) = M_0 \sum_{j=1}^{3} w_j \left[\int_0^{\infty} f_j\left(T_2; \mathbf{p_j}\right) EPG\left(T_2, \triangle TE, i, B_1\right) dT_2 \right] \tag{5.1}$$

where $t_i = i \times \triangle TE$ and $\triangle TE$ is the echo spacing of the 2D Multi-slice CPMG sequence. Each $f_j\left(T_2; \mathbf{p}\right)$ is the chosen PDF with parameters $\mathbf{p_j} \in \mathbb{R}^{+l_j}$ (assuming the chosen PDF is explained using l_j number of parameters). In Eq. (5.1), M_0 is the magnetization constant. $EPG(\cdot)$ represents the stimulated echo computed at the time point ($t_i = i \times \triangle TE$) using the EPG algorithm [Layton 2013]. The FAE is realized as B_1 is the field inhomogeneity scale factor [Layton 2013].

Optimization The optimization is thus formulated as a least square problem:

$$\begin{aligned}\left(\hat{M}_0, \hat{\mathbf{w}}, \hat{\mathbf{p}}, \hat{B}_1\right) &= \underset{M_0,\mathbf{w},\mathbf{p},B_1}{\arg\min} \sum_{i=1}^{m} \left(y_i - s\left(t_i\right)\right)^2 \\ &= \underset{M_0,\mathbf{w},\mathbf{p},B_1}{\arg\min} \left\|\mathbf{Y} - \mathbf{\Lambda}\left(M_0, \mathbf{p}, B_1\right)\mathbf{w}\right\|_2^2 \end{aligned} \tag{5.2}$$

where m is the number of echoes; $\mathbf{Y} \in \mathbb{R}^m$ is the observed signal. The parameters to be estimated in Eq. (5.2) are: $\{M_0, \mathbf{w}, \mathbf{p}, B_1\}$. $M_0 \in \mathbb{R}^+$; $\{w_j\}_{j=1}^3 \in [0,1]$; $p \in \mathbb{R}^{+^{l\times 3}}$ and $\sum_j w_j = 1$. Each element of $\mathbf{\Lambda}$ ($\Lambda_{ij} = \lambda_j\left(t_i; M_0, \mathbf{p}, B_1\right); i = \{1, ..., m\}$, $j = \{1, 2, 3\}$) in Eq. (5.2) is computed as:

$$\lambda_j\left(t_i; M_0, \mathbf{p}, B_1\right) = M_0 \int_0^\infty f_j\left(T_2; \mathbf{p}\right) EPG\left(T_2, \triangle TE, i, B_1\right) dT_2 \tag{5.3}$$

In this chapter, the PDFs to represent each T_2 relaxometry compartment ($\{f_j(\cdot)\}_{j=1}^3$ in Eq. (5.1)) are chosen as Gaussian PDFs:

$$f_j\left(T_2; \mu_j, \sigma_j\right) = \frac{1}{\sqrt{2\pi\sigma_j^2}} \exp\left(-\frac{\left(T_2 - \mu_j\right)^2}{2\sigma_j^2}\right) \tag{5.4}$$

where μ_j and σ_j are the mean and standard deviation of PDF (f_j).

5.2.2 Cost function evaluation

Before going ahead with the optimization of the proposed signal model, we will evaluate the feasibility of the simultaneous estimation of the PDF parameters and weights for our estimation framework. To realize this objective we observed the nature of the cost function with respect to the variables (PDF parameters and their associated weights) for the three compartments for varying levels of signal to noise ratio (SNR) levels. The noise free signal is generated using the forward model (shown in Eq. 5.1) for known values of PDF parameters and weights. The true multi-compartment T_2 relaxometry model values chosen for the simulation are shown in Table 5.1. A magnetization constant (M_0) value of 950 was chosen for the simulations.

	Short T2	**Medium T2**	**High T2**
μ	20.0	100.0	2000.0
σ	5.0	10.0	80.0
weight	0.4	0.4	0.2

Table 5.1: True values of the variables used for generating the decay curve using the multi-compartment T_2 relaxometry model. The units for the Gaussian PDF mean (μ) and standard deviation (σ) are in ms.

In this experiment, we first evaluate a simple scenario where we observe the possibility of estimating the mean and weight of a single compartment simultaneously. The mean of the compartments are varied within a reasonable range for each compartment. The mean of short, medium and high T_2 compartments are varied in the range of $[10, 30]$, $[70, 120]$ and $[1900, 2100]$ respectively (all values in milliseconds). The weight values are varied from 0 to 1. The other weights are maintained same as true values. Simulations are carried out for SNR values of $\{25, 50, 75, 100, 200\}$. Gaussian noise was added and the SNR was defined with respect to the first echo signal magnitude. The nature of the cost function i.e. the expression on the right hand side of Eq. 5.2 is observed to decide on the feasibility of simultaneous PDF parameter and weights estimations for a compartment. Simulation results for the cost function when the mean and weights of a compartment are simultaneously varied is shown in Fig. 5.1. For the short T_2 compartment, minimization operations for PDF mean and compartment weight simultaneously at SNR of 25 is very difficult. Although we observe an enhancement in the regularity of the cost function with increasing SNR, optimization for this cost function is unreliable. Similar observations can be made for the case of medium and high T_2 compartments (refer Fig. 5.1b and 5.1c respectively). It can be argued that if we consider a greater range of PDF mean values, we may obtain cost function values which are more convenient for simultaneous optimization of the PDF mean and weights. However, that would then dissolve the purpose of a multi-compartment T_2 relaxometry model where each compartment is intended to represent tissues with certain common characteristics (for example, mobility of water in the tissues in our case). Hence the cost function was evaluated on a suitable range of values for each compartment based on the findings in the literature [Laule 2007a, Lancaster 2003, MacKay 2016]. In the next experiment we studied the nature of the cost function when the weights of two compartments are varied simultaneously for different SNR levels. Results are shown in Fig. 5.2. For all three possible combinations, simultaneous estimation of weights of different compartments is feasible. This is however expected as when fixing the PDF parameters, the problem reduces to that of minimizing a quadratic expression.

5.2.3 Final problem setup

The observations from Section 5.2.2 indicate that simultaneous estimation of PDF parameters and weights for the compartments is non-trivial and unreliable. Hence in this chapter we choose to fix the PDF parameters. The mean and standard deviations are chosen for the three compartments based on histology findings reported in the literature [Laule 2007a, Lancaster 2003, MacKay 2016] and are set as $\mu = \{20, 100, 2000\}$ and $\sigma = \{5, 10, 80\}$ (all values in milliseconds).

Without any loss of generality, M_0 and $\{w_j\}_{j=1}^3$ in Eq. (5.1) can be combined into a single term, $\{\alpha_j\}_{j=1}^3 \in \mathbb{R}^+$. The weight corresponding to each compartment can be obtained as $w_j = \alpha_j / \sum_i \alpha_i$ and M_0 as $\sum_i \alpha_i$. The signal of the voxel at

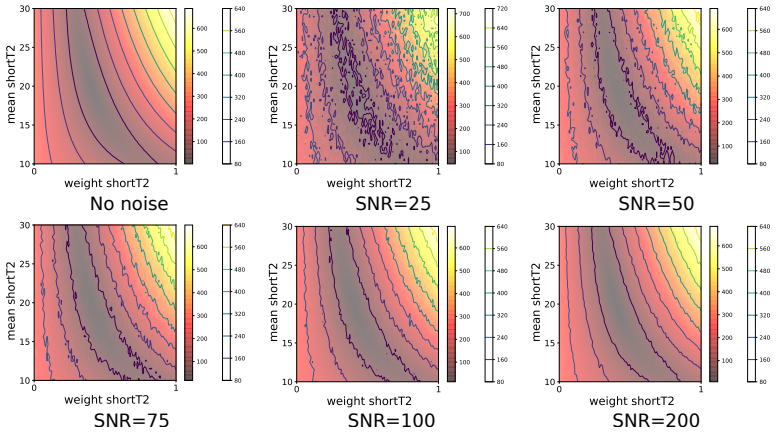

(a) With respect to short T_2 PDF mean and weights. True values: Short T_2 PDF mean = 20.0 milliseconds, weight = 0.4.

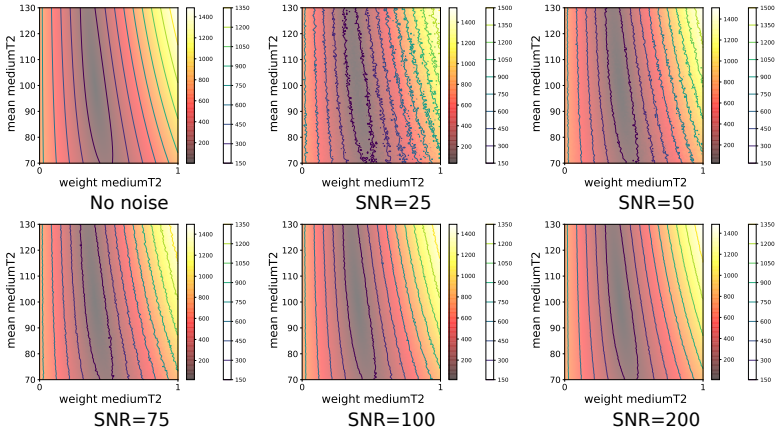

(b) With respect to medium T_2 PDF mean and weights. True values: Medium T_2 PDF mean = 100.0 milliseconds, weight = 0.4.

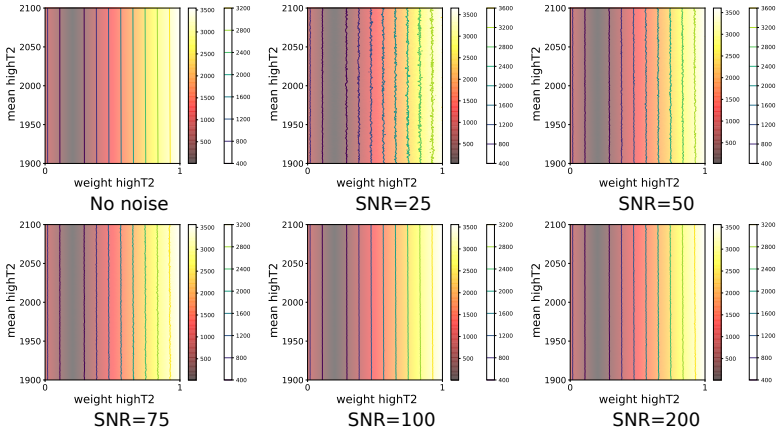

(c) With respect to high T_2 PDF mean and weights. True values: High T_2 PDF mean = 2000.0 milliseconds, weight = 0.2.

Figure 5.1: Cost function values as a function of PDF mean and weights evaluated separately for the three compartments are shown for varying levels of SNR.

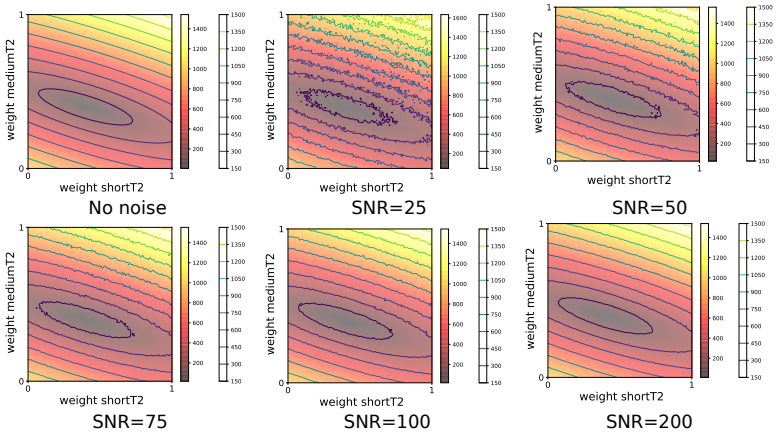

(a) With respect to short and medium T_2 compartment weights. True values: Short T_2 weight = 0.4, Medium T_2 weight = 0.4.

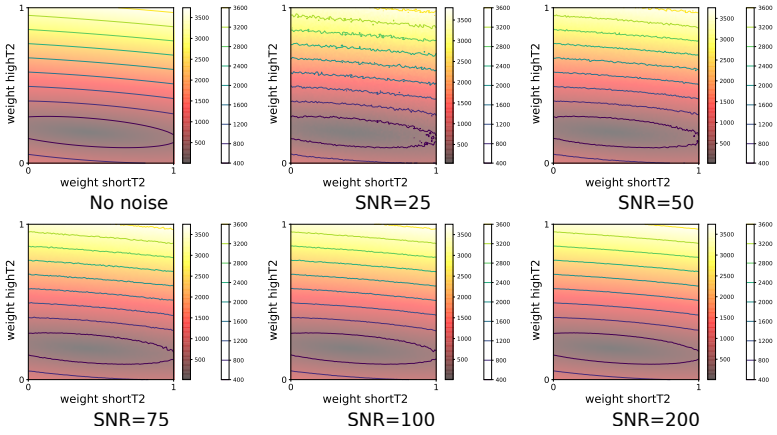

(b) With respect to short and high T_2 compartment weights. True values: Short T_2 weight = 0.4, High T_2 weight = 0.2.

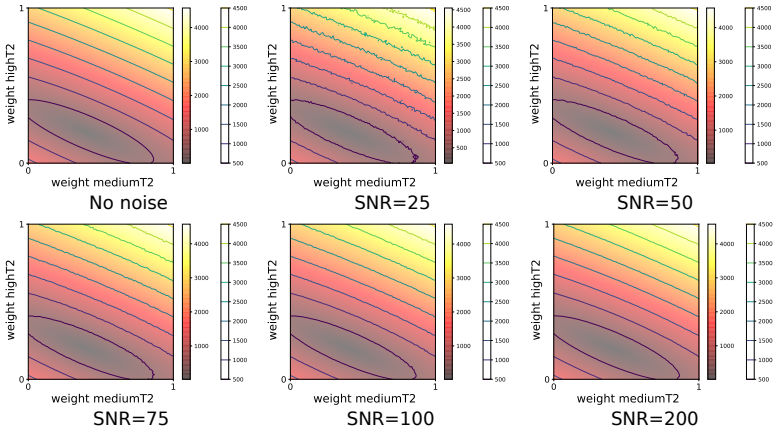

(c) With respect to medium and high T_2 compartment weights. True values: Medium T_2 weight = 0.4, High T_2 weight = 0.2.

Figure 5.2: Cost function values as a function of weights of two compartments evaluated separately are shown for varying levels of SNR.

time t_i is thus expressed as:

$$s\left(t_i\right) = \sum_{j=1}^{3} \alpha_j \left[\int_0^{\infty} f_j\left(T_2; \mathbf{p_j}\right) EPG\left(T_2, \triangle TE, i, B_1\right) dT_2 \right] \tag{5.5}$$

The optimization problem to be solved now is as shown below:

$$\begin{aligned} \left(\hat{\boldsymbol{\alpha}}, \hat{B_1}\right) &= \arg\min_{\boldsymbol{\alpha}, B_1} \sum_{i=1}^{m} \left(y_i - s\left(t_i\right)\right)^2 \\ &= \arg\min_{\boldsymbol{\alpha}, B_1} \left\| \mathbf{Y} - \boldsymbol{\Lambda}\left(B_1\right) \boldsymbol{\alpha} \right\|_2^2 \end{aligned} \tag{5.6}$$

Each element of $\boldsymbol{\Lambda} \in \mathbb{R}^{+m \times 3}$ in Eq. (5.6) is now computed as:

$$\lambda_j\left(t_i; B_1\right) = \int_0^{\infty} f_j\left(T_2; \mathbf{p_j}\right) EPG\left(T_2, \triangle TE, i, B_1\right) dT_2 \tag{5.7}$$

The parameters to be estimated in the least squares optimization problem stated in Eq. (5.6), $\boldsymbol{\alpha}$ and B_1, are linear and non-linear in nature respectively. However they are linearly separable. Hence we chose to perform the optimization for $\boldsymbol{\alpha}$ and B_1 alternatively until convergence is obtained in a desired error limit. In the first step, α is computed by non-negative least squares (NNLS) optimization [Lawson 1995] with a fixed B_1 value. In the next step, the weights computed in the first step are used to compute B_1 by a gradient free optimizer (BOBYQA). We choose to perform a numerical optimization to obtain B_1 as it does not have any closed form solution [Prasloski 2012]. The integral in Eq. (5.7) also does not have a closed form solution and the EPG gradient computations are computationally expensive. Hence the integral is computed using the Riemann sum approach by dividing the T_2 region into rectangles of finite width (= 0.33ms in our case) over the range of $[0, 2500]$ ms.

5.3 Experiments

We begin by evaluating the proposed method on a synthetic phantom in Section 5.3.1. The synthetic phantom is created with multiple sections representing various tissues such as normal appearing white matter, free fluid and MS lesion like tissues. The lesion like tissue voxels were simulated with low short T_2 content and presence of high T_2 components to account for myelin degeneration and inflammation (presence of edema) respectively. In the next two experiments we performed experiments on in-vivo T_2 relaxometry images of two phantoms. The phantoms and the associated experiment are explained in Section 5.3.2 and 5.3.3. Repeatability is an important aspect of quantitative MRI techniques. In Section 5.3.4 we discuss the test-retest experiments carried out to assess the repeatability of the proposed method on 4 healthy controls. The agreements of the values are evaluated with the help of Bland-Altman plots. Finally we evaluate the performance of the proposed

method on a MS patient in Section 5.3.5. In this experiment we observe the evolution of water fraction values in lesions and compare them with those of the normal appearing white matter.

5.3.1 Synthetic phantom experiment

A synthetic phantom with sections of different water fraction values was created to evaluate the proposed method. In addition to sections with different water fraction values, the phantom has four sections with FAE percentages of {0%, 5%, 10%, 20%}. This allowed us to account for the effect of stimulated echoes observed in multiple echo spin echo sequences, as opposed to pure exponentials [Crawley 1987]. The flip angle error values are used to account for the effect of stimulated echoes using the EPG algorithm [Prasloski 2012, Layton 2013]. The true water fraction values and FAE percentages are shown in Fig. 5.3.

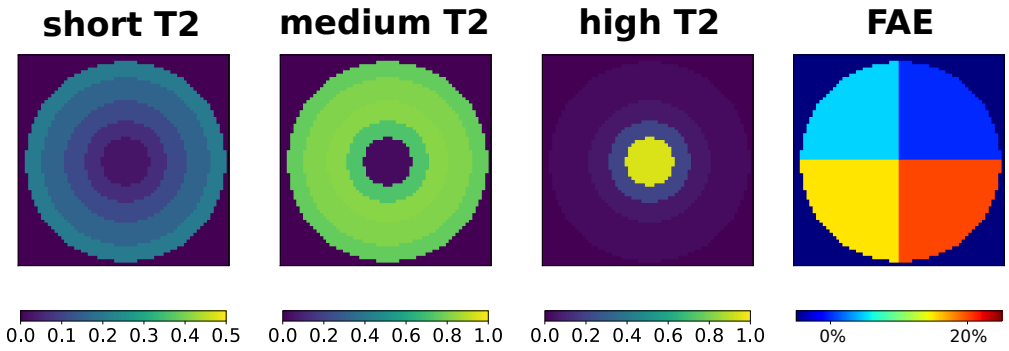

Figure 5.3: True values of the flip angle error (FAE) percentage, short T_2, medium T_2 and high T_2 water fraction for the synthetic phantom are shown here.

For simulating a multi-compartment T_2 relaxometry voxel, decay components for each voxel are mixed in the proportion of the corresponding true water fraction value (shown in Fig. 5.3). The T_2 values for short, medium and high T_2 compartments are drawn randomly from Gaussian PDFs with (mean, standard deviation) of (20, 5), (100, 10) and (2000, 80) respectively (all in ms). The simulations are performed for six SNR levels of 50, 75, 100, 200, 500 and 1000. Gaussian noise was added and the SNR is defined with respected to the first echo signal. Please refer Appendix A for details on how the synthetic phantom is generated. The first echo images of the synthetic phantom with echo spacing of $9ms$ and number of echoes = 32 are shown in Fig. 5.4 for all SNR levels evaluated in this work. We evaluate the accuracy of the proposed method for the estimated water fraction values and B_1 scale factors for all SNRs.

5.3.2 In-vivo phantom experiment I

The second experiment is performed on a phantom with three sections. Each section contains water with a different level of Gadolinium (Gd) and is intended to simulate

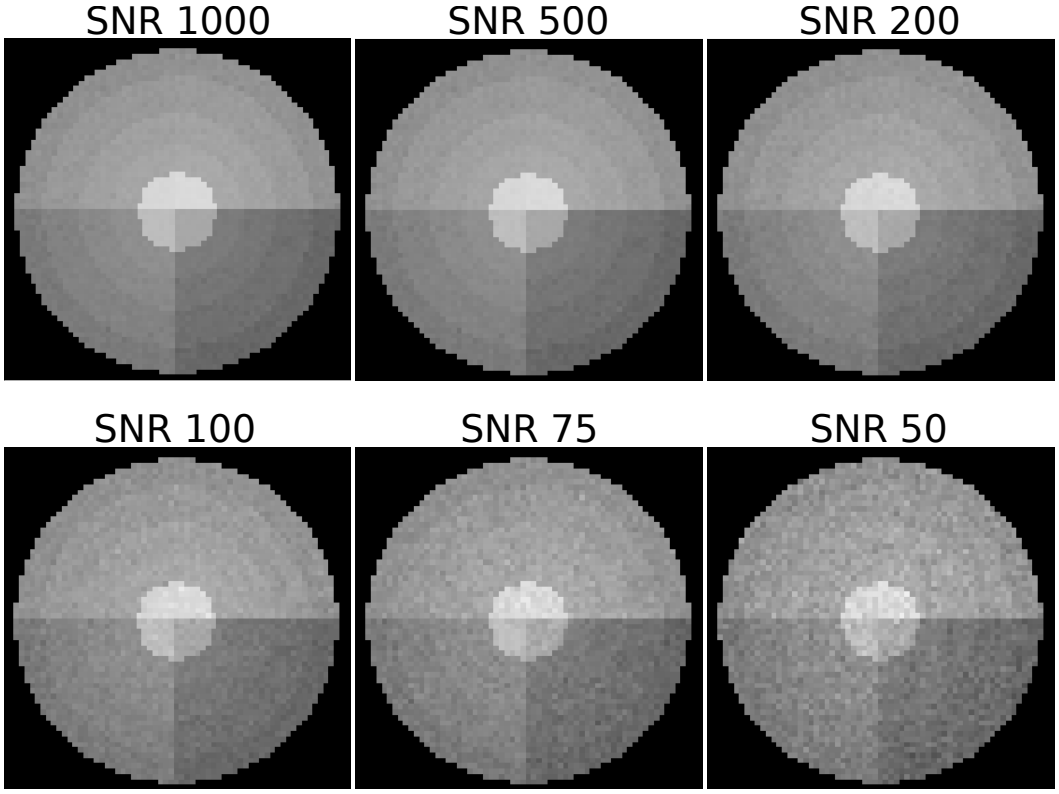

Figure 5.4: The first echo for all SNR levels of the synthetic phantom are shown here. The synthetic phantom data is generated with following specification: echo spacing = 9.0ms, number of echoes = 32.

one of the three major compartments in the brain. An observed echo of the phantom is shown in Fig. 5.5. This phantom was made by Onur Afacan, Boston Children's Hospital, Boston, MA, USA. Since each section contains a single solution, a mono T_2 estimation of the T_2 relaxometry data was performed to confirm the in-vivo T_2 values of the sections. *Section 1* contains 6mM Gd-DPTA (Magnevist) solution. The mono T_2 estimation (using EPG instead of pure exponential) showed that this section had a mean T_2 value of 39.78 ms (standard deviation = 1.37). This represents the short T_2 compartment. The water and Gd-DPTA (Magnevist) solution in the *section 2* has a mean T_2 value of 141.93 ms (standard deviation = 4.13). Hence this shall represent the medium T_2 compartment. *Section 3* contains saline water and the mean T_2 value in this section was found to be 1985.68 ms (standard deviation = 186.02). This is not a perfect test for a multi-compartment T_2 relaxometry model as each section contains values pertaining to only one compartment. The objective of this experiment is to evaluate how the method performs in presence of a single compartment in a voxel.

The acquisition details are as follows: Siemens 3T MRI machine; 2D multislice CPMG sequence; number of echoes = 32; first Echo at 9ms; echo spacing = 9ms;

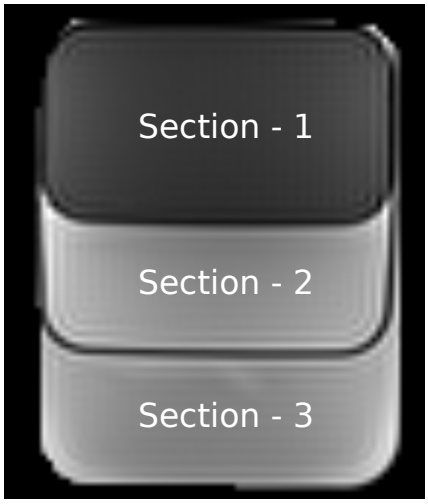

Figure 5.5: The T_2 relaxometry MRI of the phantom used for in-vivo phantom experiment I is shown here. The three sections are annotated in this figure.

single slice acquisition; in plane resolution = 1.1mm × 1.1mm; slice thickness = 4mm; matrix size = 192 × 192.

5.3.3 In-vivo phantom experiment II

For this experiment we tested our method against the NIST phantom, "Phannie" [Russek 2012]. This phantom is illustrated in Fig. 5.6.

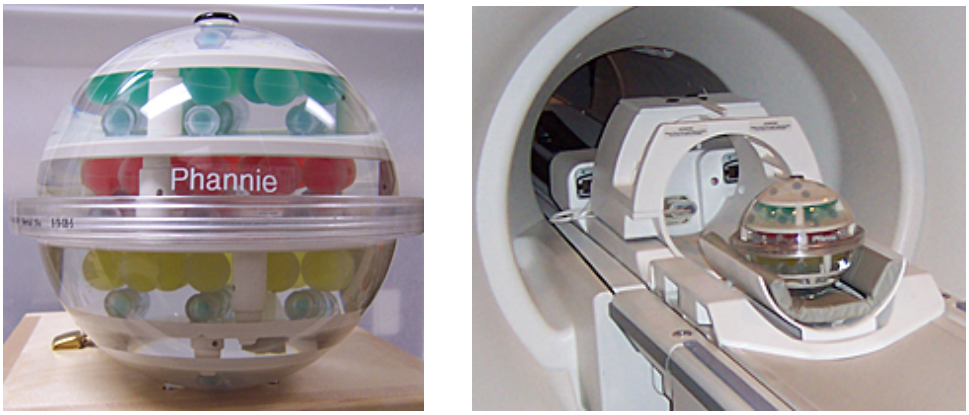

(a) (b)

Figure 5.6: The NIST phantom "Phannie". Images source: https://www.nist.gov/news-events/news/2010/05/meet-phannie-nists-standard-phantom-calibrating-mri-machines

As it can be observed from Fig. 5.6a, the phantom contains three layers of spheres. The middle layer (red spheres) consists of spheres containing solutions of

varying T_2 relaxation times. The in-vivo T_2 values for the scanner at our research center were found using mono T_2 analysis. The values ranged from around 10ms to 700ms. The water fraction values for the short T_2, medium T_2 and high T_2 were estimated for these spheres. Objective of this experiment is to observe whether the water fraction values estimated for the spheres reflect the changing T_2 values of the solution in the spheres.

The acquisition details are as follows: Siemens 3T MRI machine; 2D multislice CPMG sequence; number of echoes = 32; first Echo at $9ms$; echo spacing = $9ms$; in plane resolution = $1.33mm \times 1.33mm$; slice thickness = $3mm$; spacing between slice centers = $3mm$; matrix size = 192×192.

5.3.4 Repeatability test

The objective of this experiment is to observe whether the proposed model is repeatable in terms of estimation of the microstructure maps. For that purpose, test retest T_2 relaxometry scans of 4 healthy controls were obtained. The age of the healthy controls was in the range of 26-32 years. 15 regions of interest (ROI) marked in the brain for each healthy control over which the test and retest values of the compartments' water fractions were compared. All the ROIs were marked for one case. The ROIs were then registered on the other cases using a rigid followed by an affine registration [Ourselin 2000, Commowick 2012] to ensure that similar regions were

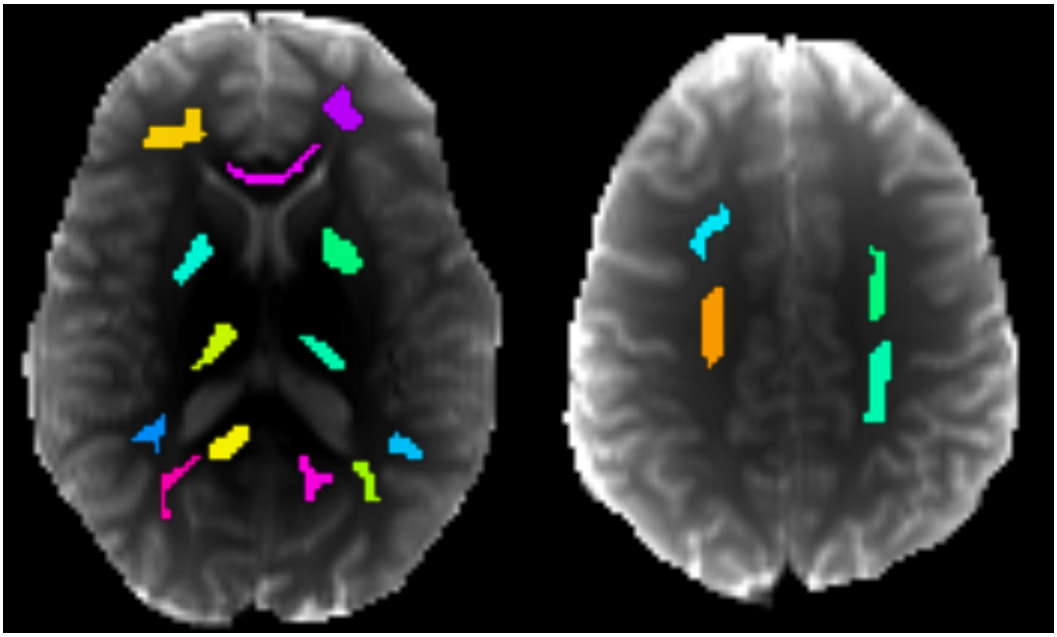

Figure 5.7: Test retest scans were performed for 4 healthy controls to study the repeatability of the proposed method. This figure shows the 15 regions which were marked on the healthy controls over which the repeatability was studied.

analyzed for repeatability in all cases. An illustration of these ROI on a subject is shown in Fig. 5.7.

The details of the acquired data are as follows: 3T MRI scanner; 2D multislice CPMG sequence; 32 echoes; first echo at 9ms; echo spacing = 9ms; TR = 2000ms; single slice acquisition; in plane resolution= 1.1mm ×1.1mm; slice thickness of 5mm; matrix size of 192×192; number of averages= 1. The data was acquired on the same day. The subject was moved out and then placed back in the scanner to acquire the test and the retest data.

A Bland-Altman plot was used to observe the repeatability of the estimations over the ROIs. From the plot we obtained the mean deviation (m_d) of the test retest values for the ROIs and checked whether there are noticeable systematic changes in the estimations. We further look at the limits of agreement (LoA) between the test retest estimations. The voxel wise values in the ROI are compared in a scatter plot between estimated test and retest values. The coefficient of determination was computed for a linear fit. The slope and intercept of the linear fit was also observed. The ideal fit shall have a R^2 fit score of 1.0 and a slope and intercept of 1.0 and 0.0 respectively.

5.3.5 Application on healthy control and multiple sclerosis patient

In this experiment we will observe the water fraction maps for a healthy control and multiple sclerosis (MS) patient. Water fraction values in two lesions are observed. The same patient had two scans following the baseline scan at 12 and 24 months time intervals. Hence we observe the evolution of the water fraction values of the three compartments in the two lesions. In another analysis, evolution of water fraction values for all the lesions are compared with the evolution of few normal appearing white matter (NAWM) regions in the MS patient. The lesion and NAWM regions are marked on the baseline scan and the water fraction values of these regions is analyzed for the follow-up scans. All lesions are marked by a radiologist on FLAIR images. All the water fraction maps are registered on the FLAIR image acquired at the baseline using a block matching algorithm [Commowick 2012, Ourselin 2000].

The details of the T_2 relaxometry data acquired for the healthy control are as follows: 3T MRI scanner; 2D multislice CPMG sequence; 32 echoes; first echo at 9ms; echo spacing = 9ms; TR = 3720ms; in plane resolution= 1.33mm ×1.33mm; slice thickness of 4mm; space between consecutive slices = 4mm; matrix size of 192 × 192; number of averages= 1. The MS patient had the following details: 3T MRI scanner; 2D multislice CPMG sequence; 11 echoes; first echo at 8.4ms; echo spacing = 8.4ms; TR = 4650ms; in plane resolution= 1.33mm ×1.33mm; slice thickness of 3mm; space between consecutive slices = 3mm; matrix size of 192×192; number of averages= 1. All images were registered to the FLAIR image acquired at baseline scan (on which the lesions were marked). The FLAIR image had voxel size of = 0.5mm ×0.5mm ×1.1mm (matrix size of 256 × 246).

5.4 Results

5.4.1 Synthetic phantom experiment

Relative mean square error (rMSE) was used to quantify the error in estimation. The rMSE was computed as shown below:

$$rMSE = \frac{\sum_{i=1}^{N} (\hat{q}(i) - q_{true}(i))^2}{\sum_{j=1}^{N} q_{true}(j)^2} \tag{5.8}$$

where $\hat{q}$ is the estimated quantity and q_{true} is the true value. Results are shown in Fig. 5.8. The rMSE values are in the order of 10^{-2} for all the water fraction values. The rMSE values reduce as the SNR improves. The errors in FAE estimation were observed to be in the order of 10^{-5}. The water fraction maps estimated for all SNRs are shown in Fig. 5.9.

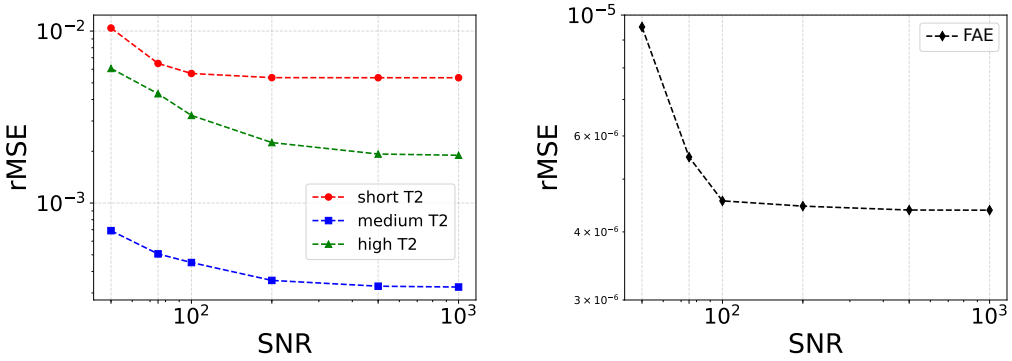

Figure 5.8: rMSE values for estimated water fraction (left) and FAE (right) are shown here. Both axes are in log scale.

5.4.2 In-vivo phantom experiment I

Results of the experiment discussed in section 5.3.2 are shown in Fig. 5.10 and 5.11. The statistics of the estimated water fractions corresponding to short, medium and high T_2 compartments for each section are computed over the regions of the phantom shown in Fig. 5.10. The statistics of the short T_2, medium T_2 and high T_2 water fraction are computer over the blue, green and red masks respectively. The FAE percentage estimated using the method is shown also shown in Fig. 5.10.

The water fraction maps estimated for the sections are shown in Fig. 5.11. The statistics computed over the regions shown in Fig. 5.10 are summarized in Table 5.2. For each section the water fraction value for the relevant compartment is stated.

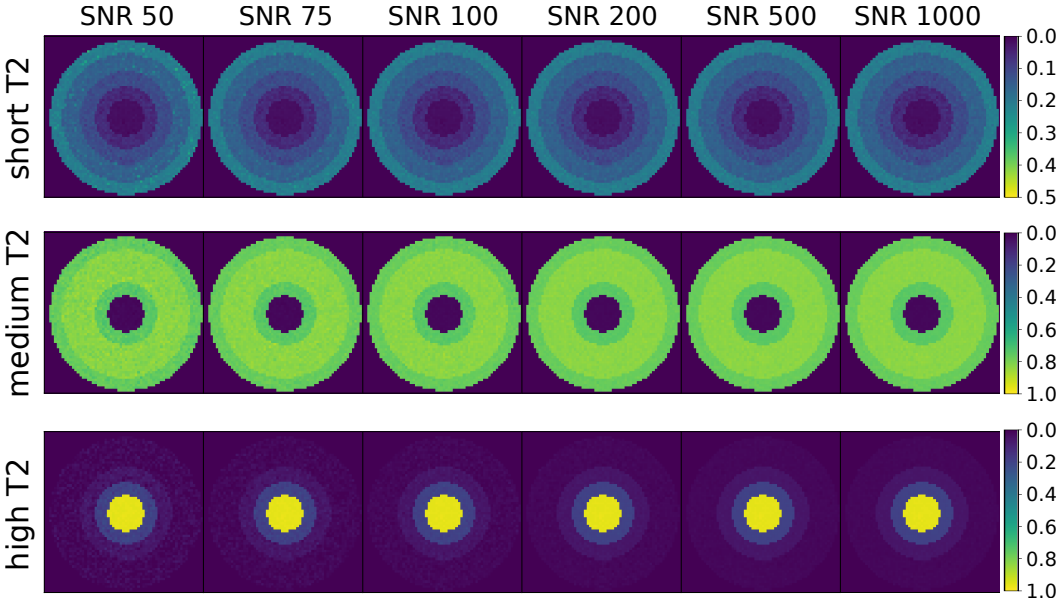

Figure 5.9: Short, medium and high T_2 water fraction maps estimated using the proposed methods for different levels of SNRs are shown here.

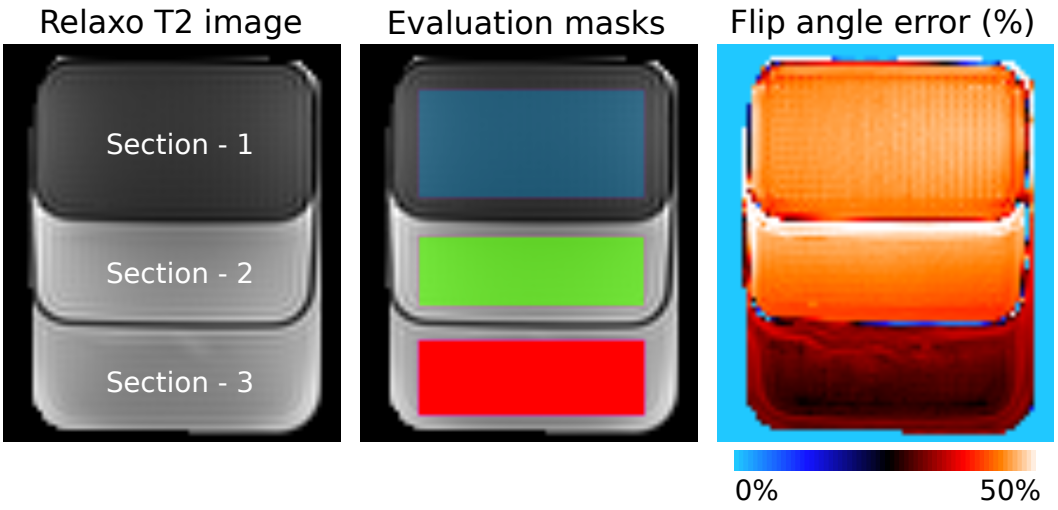

Figure 5.10: *(Left to right)* The phantom with the annotated sections. Region of interest over which statistics of the estimated water fraction is computed for the three sections. FAE maps estimated using the model.

5.4.3 In-vivo phantom experiment II

The results of the NIST phantom analysis is discussed in this section. The phantom consists of multiple spheres where each contains solution with a specific T_2 value (see Section 5.3.3). The T_2 relaxometry image, evaluation masks for each of the 14

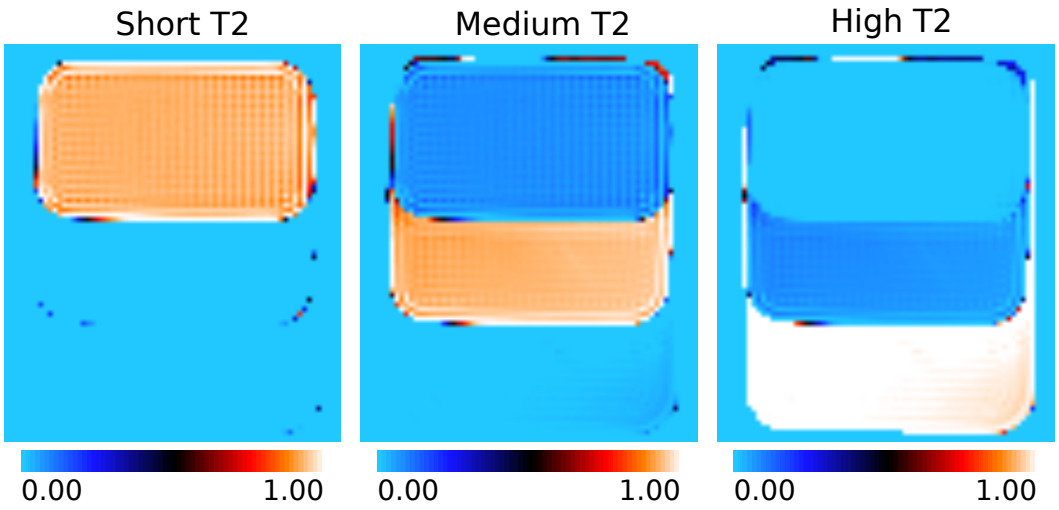

Figure 5.11: *(Left to right)* Short T_2, medium T_2 and high T_2 water fraction maps estimated for the in-vivo phantom I.

	Short T_2 weight		Mono T_2 value	
	μ	σ	μ	σ
Section 1	0.93	0.012	29.78	1.37

	Medium T_2 weight		Mono T_2 value	
	μ	σ	μ	σ
Section 2	0.93	0.009	131.93	4.13

	High T_2 weight		Mono T_2 value	
	μ	σ	μ	σ
Section 3	0.99	0.005	1985.68	186.02

Table 5.2: The water fractions for short T_2, medium T_2 and high T_2 compartments for the three sections are shown here. The mean (μ) and standard deviation (σ) of the water fraction maps are computed over for each section over the regions indicated in Fig. 5.10.

T_2 spheres and the B_1 scale factor map for the NIST phantom is shown in Fig. 5.12. The estimated water fraction maps for the spheres are shown in Fig. 5.13. The spheres in the NIST phantom have mono T_2 solution. The water fraction statistics for all the T_2 spheres are shown in Table 5.3. We show additionally in Fig. 5.14 in red, green and blue shades the regions where the short T_2, medium T_2 and high T_2 water fractions dominate respectively. The T_2 spheres with values less than 35ms are represented by short T_2 compartment. From 35 to 130 ms, the water fraction values are represented by the medium T_2 compartment. The high T_2 water fraction value gains representation from 130ms onward. The T_2 spheres having T_2 values

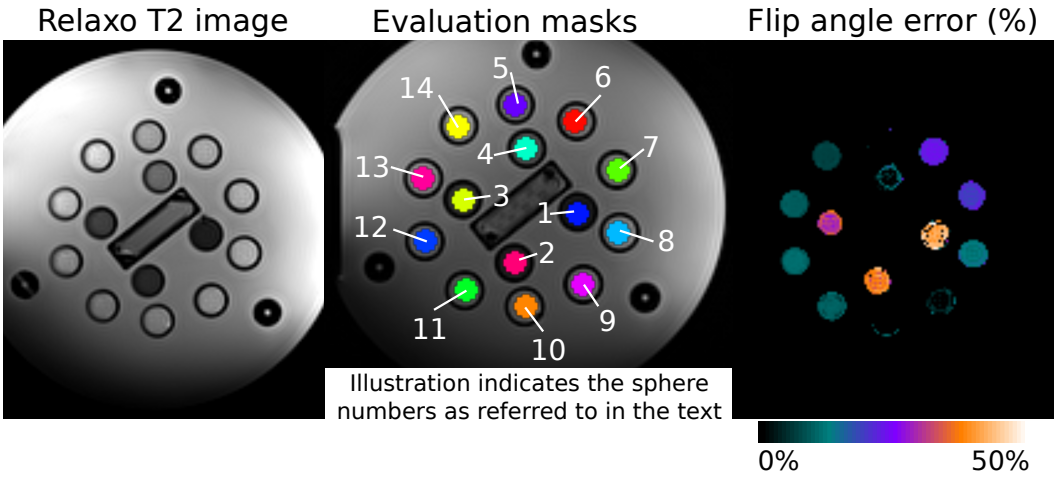

Figure 5.12: *(Left to right)* The phantom with the annotated sections. Region of interest over which statistics of the estimated water fraction values are analyzed for the 14 T_2 spheres. FAE percentage maps estimated using the model.

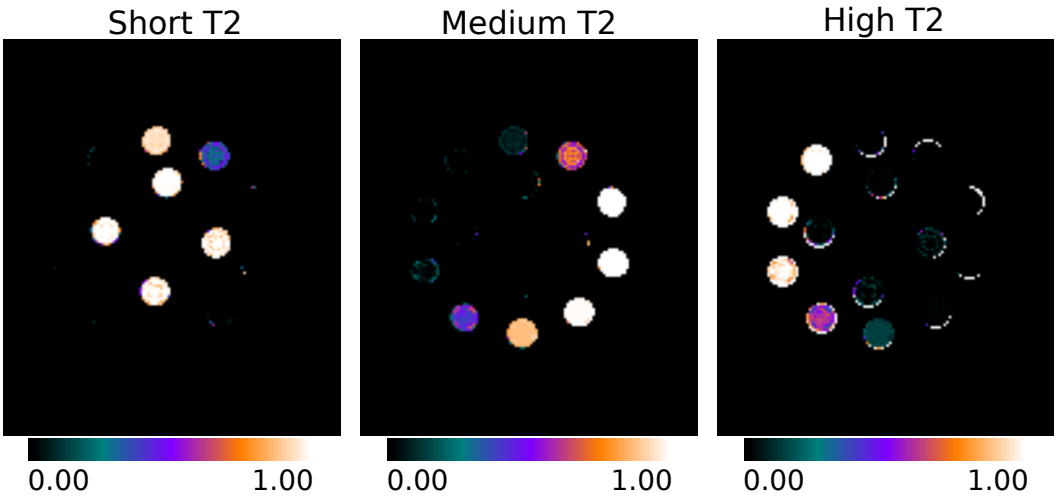

Figure 5.13: *(Left to right)* Short , medium and high T_2 water fraction maps estimated for the T_2 spheres in the NIST phantom using the proposed model are shown.

greater than 200ms are represented solely by the high T_2 compartment.

5.4.4 Repeatability test

The Bland-Altman (BA) plots for short, medium and high-T_2 water fraction estimates over the ROIs are shown in Fig. 5.15. BA plots are scatter plots between the average test-retest measurement and the difference between test-retest measurements. We measured the means of the estimated values of 15 ROIs in 4 healthy

		Short T_2 weights		Medium T_2 weights		High T_2 weights	
Region	T_2 value	μ	σ	μ	σ	μ	σ
Label 1	31.84	0.96	0.05	–	–	0.04	0.05
Label 2	21.92	0.96	0.04	–	–	0.04	0.04
Label 3	16.56	0.98	0.03	–	–	0.02	0.03
Label 4	19.56	0.99	0.01	–	–	0.01	0.01
Label 5	26.07	0.93	0.03	0.06	0.04	–	–
Label 6	34.79	0.29	0.15	0.71	0.15	–	–
Label 7	47.59	–	–	1.00	0.00	–	–
Label 8	65.59	–	–	1.00	0.00	–	–
Label 9	91.64	–	–	0.99	0.01	0.01	0.01
Label 10	130.64	–	–	0.88	0.01	0.12	0.01
Label 11	200.02	–	–	0.40	0.06	0.60	0.06
Label 12	286.89	–	–	0.01	0.02	0.99	0.02
Label 13	378.11	–	–	–	–	1.00	0.00
Label 14	603.03	–	–	–	–	1.00	0.00

Table 5.3: This table show the mean (μ) and standard deviation (σ) of short T_2, medium T_2 and high T_2 compartments for the 14 T_2 spheres in the NIST phantom. The label index can be checked from Fig. 5.12. The T_2 values shown in this table are obtained by performing a mono T_2 analysis of the data.

controls. The BA plots for short, medium and high-T_2 water fraction estimates for the 15 ROIs are shown in Fig. 5.15a, 5.15b and 5.15c respectively. The plots shows the level of mean error (m_d) observed. The gray area around the mean error level is its 95% confidence interval (CI). Along with m_d, the $m_d \pm 1.96 \times \sigma_d$ levels are also shown and are referred to as levels of agreement (LoA). σ_d is the standard deviation associated with the errors observed in the test-retest measurements. LoA is thus an empirical estimate of the range around m_d within which 95% of the differences are expected to exist. The 95% CI of the LoAs for each plot is shown with a yellow shade around LoA in the plots. The BA plot statistics are summarized in Table 5.4. From Fig. 5.15, we observe that the mean bias of difference between the test-retest ROI mean values (m_d) is close to zero for short, medium and high-T_2 water fraction estimates. For all three water fraction estimations, the zero level lies comfortably inside the 95% CI of the m_d. The test retest differences lie within the LoA and its 95% CI.

5.4.5 Application on healthy control and multiple sclerosis patient

The water fraction maps for a healthy control are shown in Fig. 5.16. Results for a MS patient are shown in Fig. 5.17. Two lesions are indicated in the axial slice: lesion-1 and lesion-2 are marked with green and red arrows respectively. The absence or very low short T_2 water fraction values in the lesion region (and its immediate surrounding) indicates demyelination. The high T_2 water fractions in

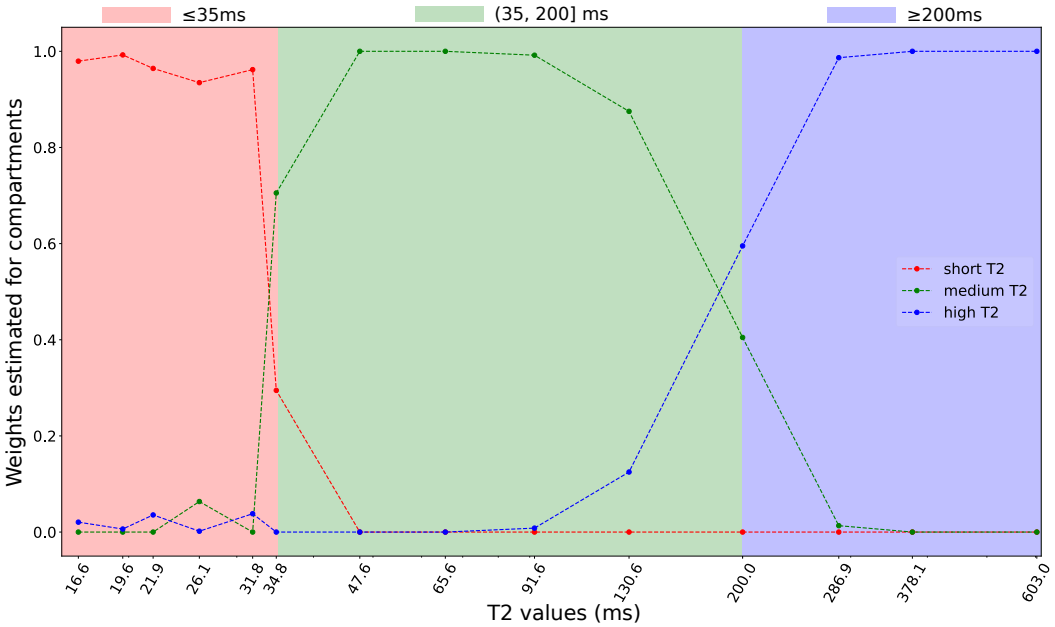

Figure 5.14: The values for the estimated water fraction value for three compartments are plotted with respect to the T_2 value of the spheres. The three sections shown in the graph pertain to regions where water fractions for one compartment is dominant.

	Mean bias (m_d)	*95% CI around* m_d	*LoA*
Short T_2	-0.0005	$[-0.0051, 0.0039]$	0.0161
Medium T_2	0.0006	$[-0.0039, 0.0051]$	0.0161
High T_2	-0.0001	$[-0.0005, 0.0002]$	0.0001

Table 5.4: This table summarizes the statistics of the Bland-Altman (BA) plots shown in Fig. 5.15 for short, medium and high-T_2 water fraction estimates. For each compartment the mean bias of the difference in the estimates (m_d), the 95% confidence interval (CI) around m_d and the limits of agreement (LoA) are shown.

these regions are higher compared to the surrounding NAWM in the brain, indicating inflammation. In lesion-2, the medium T_2 water fraction values decrease as we move from the surrounding NAWM regions towards the lesion core. This might be an indication of the axonal damage caused by MS. Hence from the water fraction maps, we observe indications of the expected demyelination and inflammation in the lesion affected regions.

As mentioned in section 5.3.5, there were two follow-up scans from the baseline scan for the MS patient. For the two lesions highlighted, we observed the change in the water fraction for the three compartments over a 24 months period. Results are

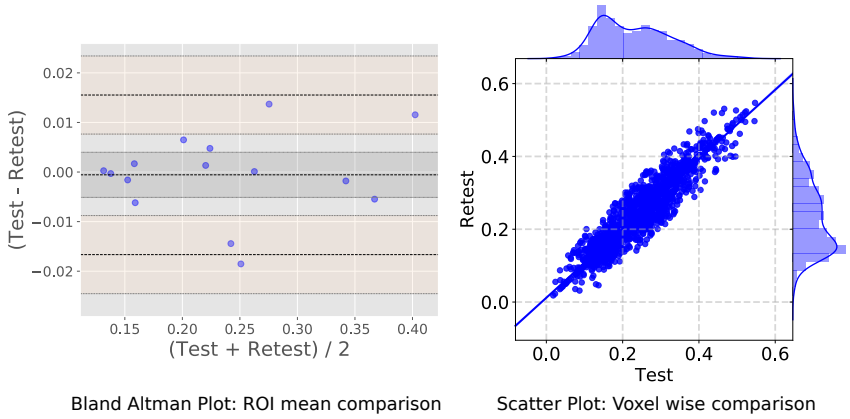

Bland Altman Plot: ROI mean comparison Scatter Plot: Voxel wise comparison

(a) Short T_2 water fraction

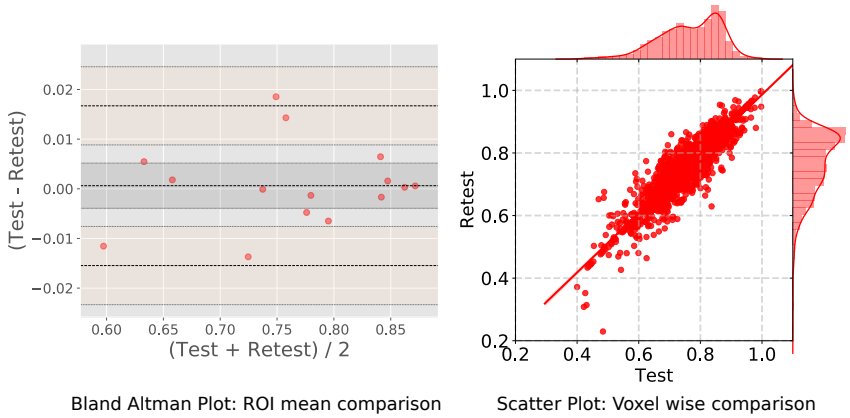

Bland Altman Plot: ROI mean comparison Scatter Plot: Voxel wise comparison

(b) Medium T_2 water fraction

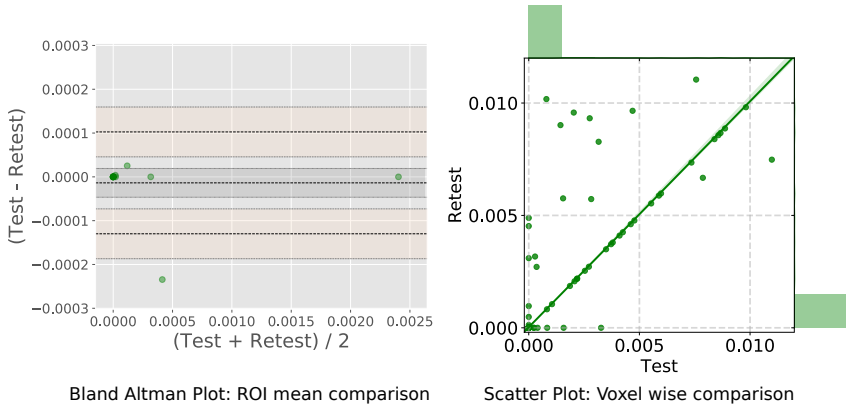

Bland Altman Plot: ROI mean comparison Scatter Plot: Voxel wise comparison

(c) High T_2 water fraction

Figure 5.15: The test retest values for the estimated water fraction of three compartments in the ROIs (shown in Fig. 5.7) are compared in the form of Bland-Altman (BA) plots and scatter here. The BA plots compare the ROI mean values whereas the scatter plot compares values at each the voxel in ROIs. The BA plot and scatter plot statistics are summarized in Table 5.4 and 5.5 respectively.

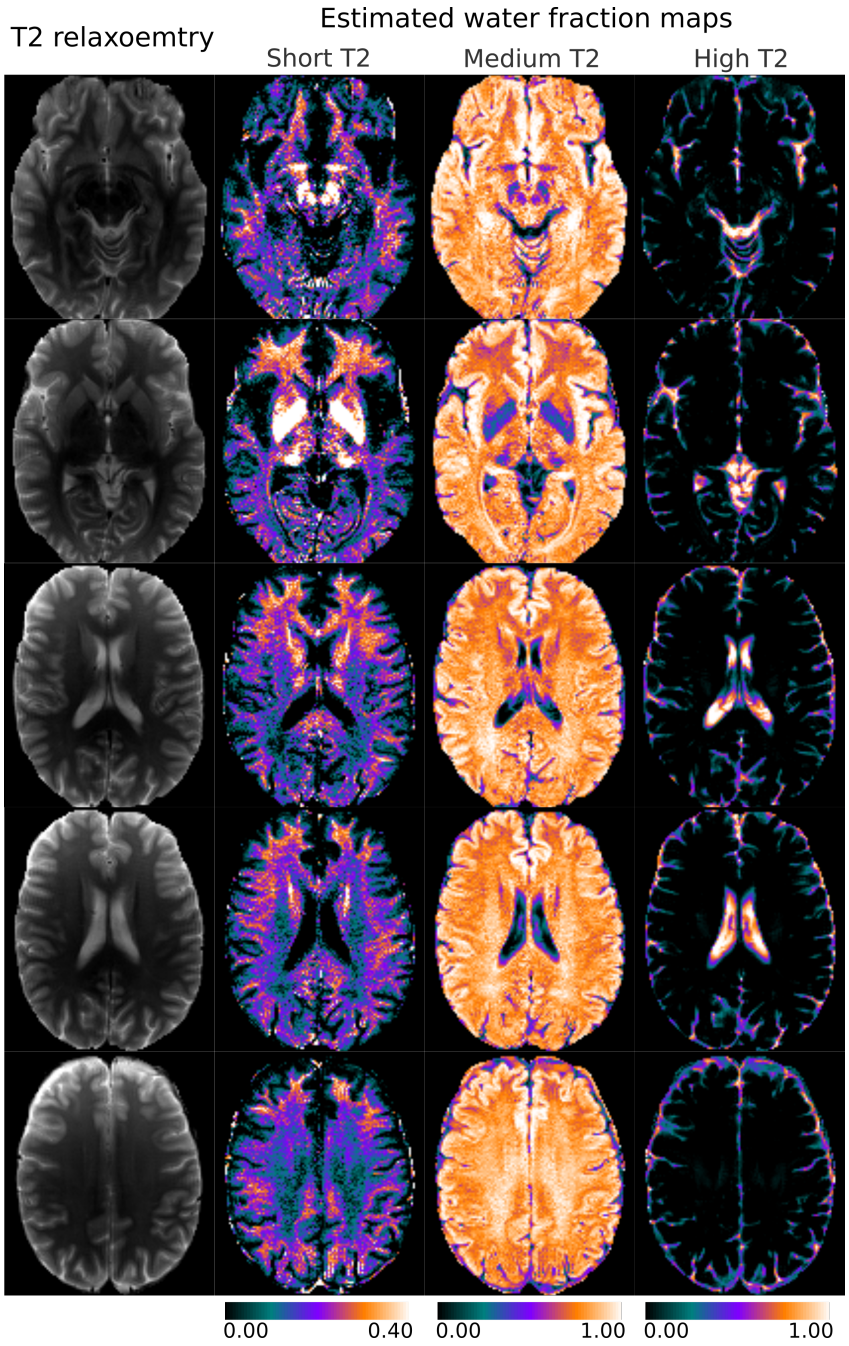

Figure 5.16: Water fraction maps estimated for the short T_2, medium T_2 and high T_2 compartments for a healthy control.

Water fraction	R^2	*Slope*	*Intercept*
Short T_2	0.888	0.952	0.012
Medium T_2	0.861	0.947	0.039
High T_2	0.966	1.005	0.000

Table 5.5: This table summarizes the regression statistics of the plots shown in Fig. 5.15 for short, medium and high-T_2 water fraction estimates respectively. The regression statistics are obtained by comparing all the voxels in the 15 ROIs of four healthy controls.

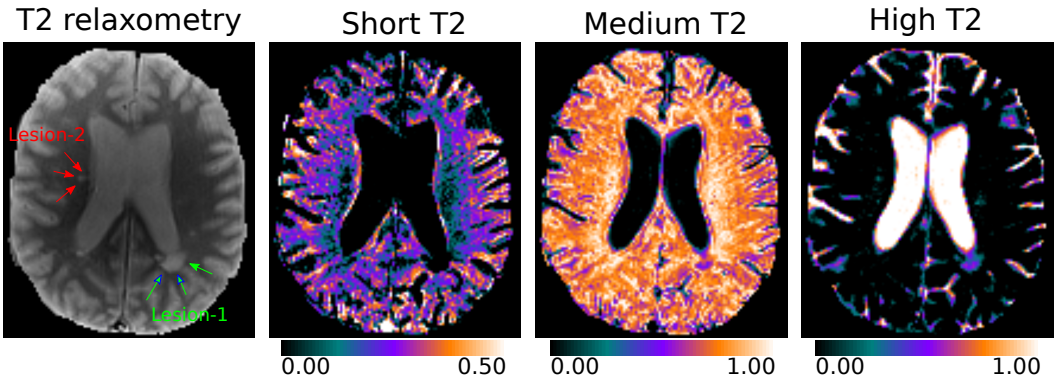

Figure 5.17: Water fraction maps estimated for the short T_2, medium T_2 and high T_2 compartments for a MS patient.

shown in Fig. 5.18. In both lesions, an increase in the short T_2 water fraction value over 24 months indicates remyelination. A slight decline in the medium T_2 water fraction values is observed for lesion-2. This might be an indication of axonal loss.

In the next analysis, we evaluate the evolution of the water fractions in all lesions and 8 NAWM ROIs in the same patient. Results are shown in Fig. 5.19. The short T_2 values in the NAWM regions (refer Fig. 5.19b) do not show indications of demyelination. Absence of high T_2 water fraction values in NAWM regions indicate no signs of inflammation. On the contrary, tissues affected by MS lesions have a very low short T_2 water fraction values and substantial presence of high T_2 water fraction values indicating demyelination and presence of inflammation.

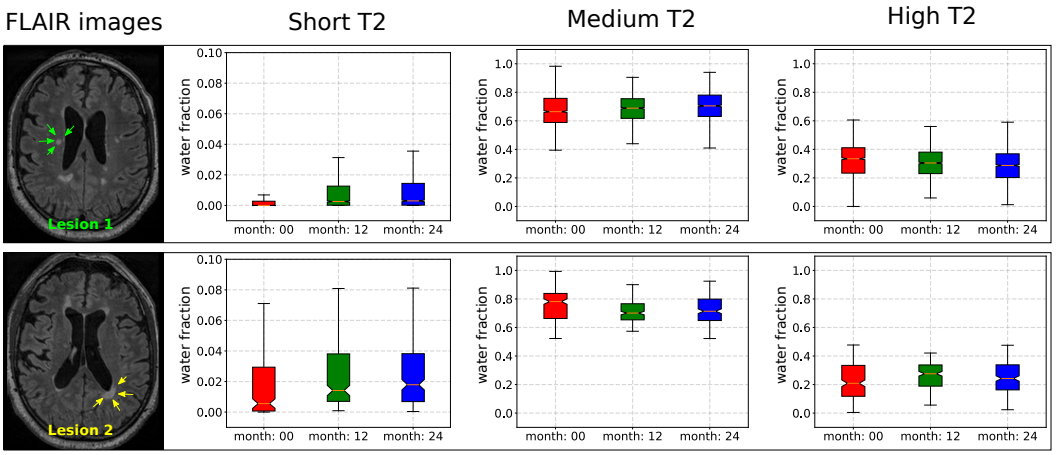

Figure 5.18: Evolution of the water fraction values of the short T_2, medium T_2 and high T_2 compartments over a period of 24 months for two lesions in a MS patient.

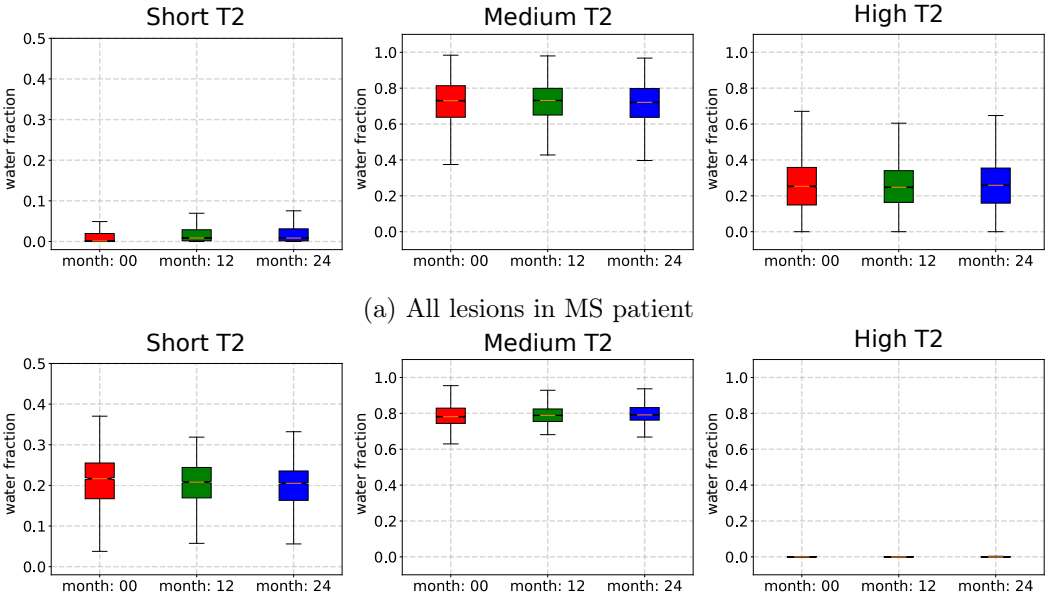

(a) All lesions in MS patient

(b) NAWM region of interests

Figure 5.19: The evolution of water fractions for the three compartments are compared for lesions and NAWM regions in MS patients.

5.5 Discussion

An initial validation of the method was carried out on a synthetic phantom. The relative mean square error for the estimated short and high T_2 water fractions was of the order of 10^{-2}, whereas it was of the order of 10^{-3} for the medium T_2 water fraction. This might be attributed to the fact that the data specification used for

simulation (echo spacing = 9.0ms; echo train length = 32) had maximum echoes corresponding to the medium T_2 compartment. However, it shall be noted that rMSE was quite low for all SNRs and reduced as the SNR improved. The water fraction maps also show a visual improvement in the estimation with improving SNR.

The next stage of validation of the method was carried out on two phantoms. Both phantoms had multiple sections with single T_2 values. The first phantom had three sections and each section's T_2 values fell within the range of a single compartment. The estimation results showed that the model predicted this with high accuracy. The second phantom had a wider range of T_2 values. Some T_2 values were in the transition range of the T_2 compartments. There were two important outcomes of this experiments. The first observation is that for a range of values which were well within the range of a single T_2 compartment were predicted with high accuracy. Secondly, this method provided insights into how the model behaves when the T_2 values are in the transition stages of the compartment. For the choice of parameters made for the model in this work, we can roughly say that the short T_2 and high T_2 compartments represent tissues with T_2 values lesser than $35ms$ and greater than $200ms$ respectively. The medium T_2 compartment has representations for T_2 values in the range of 35-$200ms$. Hence this experiment provides us a rough idea of T_2 values of the tissues depicted by each compartment. However, it shall be noted that these are mono T_2 voxels whereas the tissues in the brain and other parts of the body are multi T_2 (other than regions with only fluids such as CSF etc.). Hence this experiment is not a perfect depiction of a multi-compartment T_2 relaxometry voxel, but does provide a fair idea of the T_2 values which compartments resemble for in-vivo MRI data. Phantom experiments like this is useful in analyzing the effect of fixing parameters in parametric models where the parameters are preselected. Similarly, it can also be used to select the parameters to be fixed for the model.

The test-retest experiment results show that the quantitative MRI markers estimated by the proposed method is repeatable. For all the markers estimated, the zero level was comfortably inside the 95% confidence interval of the mean difference observed between the test and retest values of the marker for the 15 ROIs (refer the Bland-Altman plots in Fig. 5.15). Hence there are no noticeable systematic changes in the estimated markers for the test and retest data [Lexell 2005]. The regression results on the scatter plot shows a good linear fit and the slope and intercept of the linear fit being close to ideal. Thus, combining the observations from results of the experiments on synthetic phantom data, in-vivo phantom data and repeatability tests on healthy controls, the proposed method appears to be robust and a good alternative to the conventional non-parametric methods (which suffer from the apprehensions around the use of regularization [Does 2018]) and parametric methods which employ complex estimation methods known for their difficult and unreliable nature of the estimation framework [Layton 2013].

Application of the proposed method on MS patient data provided interesting observations. As compared to the contra-lateral NAWM regions, the MS lesion affected brain tissues show absence or lower short T_2 water fraction values and higher

values of for high T_2 water fractions. These observations indicate demyelination and inflammation in the MS affected tissues. In some large lesions a drop in the medium T_2 water fraction values were observed. This might indicate axonal degeneration in such lesions. The observations from the longitudinal studies showed that lesions slightly gained short T_2 water fraction values. This was accompanied by a small reduction in high T_2 values over the period of 24 months. This might indicate remyelination and reduction of inflammation in the lesion affected regions. However, the changes observed for water fraction values (between acquisitions) were in the order of the *LoA* (refer Table 5.4) obtained from the test retest experiment. Hence we can not comment much on whether the indications of remyelination and reduction of inflammation were possibly true. We should also bear in mind that these experiments were performed on only one patient and there was a long interval between successive scans. The water fraction values of NAWM in the same patient were also observed for the baseline and the follow-up scans. In contrast to the lesion, there was substantial short T_2 and no high T_2 water fraction values in the NAWM regions. There are no observable changes in these values over the period of 24 months. The multi-compartment T_2 relaxometry biomarkers are able to represent the demyelination and inflammation in MS lesions. The observations are consistent with the pathological findings in the literature [Lassmann 2001]. The MS lesion analysis was done on clinically acquired data. The acquisition time of the data used in the presented study was around 11 minutes. The non parametric methods (multiple exponential fitting) would have to rely heavily on regularization for such clinical data. However, the parametric method presented is simple and can be used for clinically acquired data. In the chapters 7 and 8 we have shown more exhaustive clinical study and application using the method proposed here.

Chapter 6

Multi-compartment model of brain tissues from T_2 relaxometry MRI using gamma distribution

Contents

6.1 Introduction

In the last chapter we discussed multi-compartment T_2 relaxometry model where probability density function (PDF) parameters representing the T_2 pools had been fixed based on the cost function analysis. We used synthetic data simulations to observe the cost function while simultaneously varying the T_2 pool PDF parameters and its weight. We observed a (stretched) valley of cost function values around the true minima whose values are close to cost function value at true minima. This

suggested that for a NNLS estimation framework simultaneous T_2 pool PDF parameter and its weights is non-trivial and non-reliable. The observation from the cost function analysis in the last chapter is in agreement with the observations made in [Layton 2013].

In this chapter we evaluate the possibility of estimating the PDF parameters and its weights for a multi-compartment T_2 relaxometry model. Rather than using a direct non-negative least square approach trying to solve T_2 pool PDF parameters and their weights simultaneously, we adopted a variable projection (VARPRO) approach. This approach has been used by Akhondi-Asl et al, where the authors modeled the T_2 pools using Wald PDFs and estimated all the T_2 pool PDF parameters [Akhondi-Asl 2015]. The authors addressed the issue of stimulated echoes by using generalized echo curves (using Bloch equations). In this chapter (similar to the last one) we studied the VARPRO cost function to evaluate the difficulty of estimating multiple T_2 pool PDF parameters. Based on the cost function analysis observations, we form the optimization problem. As in the last chapter, we also estimated the flip angle error (FAE) percentage to account for stimulated echoes.

The model is first validated on synthetic data where the estimated water fraction values against ground truth. In-vivo phantom experiments were performed using two different phantoms. The water fraction estimates were compared for test-retest data of healthy controls to asses the repeatability of the proposed method. The method was then applied on a patient with multiple sclerosis patient.

6.2 Method

6.2.1 Signal Model

As in chapter 5, the T_2 space is modeled as a weighted mixture of three PDFs, representing each of the three T_2 relaxometry compartments: short−, medium− and high−T_2. Thus the voxel signal at the i−th echo time (t_i) is given as:

$$s\left(t_i\right) = \mathrm{M}_0 \sum_{j=1}^{3} w_j \int_0^{\infty} f_j\left(T_2; \mathbf{p_j}\right) \mathrm{EPG}\left(T_2, \triangle TE, i, B_1\right) dT_2 \tag{6.1}$$

Each compartment is described by a chosen PDF, $f_j\left(T_2; \mathbf{p_j}\right)$, where $\mathbf{p_j} = \{p_{j_1}, \ldots, p_{j_n}\} \in \mathbb{R}^n$ are the PDF parameters. In Eq. (6.1), w_j is the weight of the j-th distribution with $\sum_j w_j = 1$. ΔTE and M_0 are the echo spacing and magnetization constant respectively. Imperfect rephasing of the nuclear spins after application of refocusing pulses leads to the generation of stimulated echoes [Hennig 2004]. Hence the T_2 decay is not purely exponential. The stimulated echoes are thus obtained using the EPG algorithm [Layton 2013]. EPG$(\cdot)$ is the stimulated echo computed at $t_i = i\,\Delta\mathrm{TE}$ where $i = \{1, \ldots, m\}$ and m is the number of echoes. The flip angle error has been realized using a B_1 (as in Eq. (6.1)) scale factor to account for the stimulated echoes [Layton 2013].

Optimization M_0 and w_j can be combined into a single term $\alpha_j \in \mathbb{R}^+$ without any loss of generality. In that case, the weight w_j corresponding to each compartment is obtained as $w_j = \alpha_j / \sum_i \alpha_i$. In the most general case, the least squares minimization problem is thus formulated as:

$$\begin{aligned}\left(\hat{\boldsymbol{\alpha}}, \hat{\mathbf{p}}, \hat{B_1}\right) &= \arg\min_{\boldsymbol{\alpha},\mathbf{p},B_1} \sum_{i=1}^{m} \left(y_i - \sum_{j=1}^{3} \alpha_j \lambda_j \left(t_i; \mathbf{p_j}, B_1\right) \right)^2 \\ &= \arg\min_{\boldsymbol{\alpha},\mathbf{p},B_1} \left\| \mathbf{Y} - \boldsymbol{\Lambda}\left(\mathbf{p}, B_1\right) \boldsymbol{\alpha} \right\|_2^2 \end{aligned} \tag{6.2}$$

where $\mathbf{Y} \in \mathbb{R}^m$ is the observed signal and m is the number of echoes; $\alpha \in \mathbb{R}^{+^3}$; $\boldsymbol{\Lambda} \in \mathbb{R}^{m \times 3}$; $\mathbf{p} = \{\mathbf{p_1}, \mathbf{p_2}, \mathbf{p_3}\} \in \mathbb{R}^k$, where $k = 3n$. $\mathbf{p_j}$ are the PDF parameters describing the j-th T_2 pool. Unlike the method proposed in chapter 5, let us consider optimizing the T_2 pool PDF parameters (at least some if not all). In Eq. (6.2), each element of $\boldsymbol{\Lambda}$, $\Lambda_{ij} = \lambda\left(t_i; \mathbf{p_j}, B_1\right)$, is computed as:

$$\Lambda_{ij} = \int_0^\infty f_j\left(T_2; \mathbf{p_j}\right) EPG\left(T_2, \triangle TE, i, B_1\right) dT_2 \tag{6.3}$$

There is no closed form derivative solution for the optimization of B_1 due to the EPG formulation [Prasloski 2012]. Hence, we opt for an alternate optimization scheme where we iterate between optimization of $\{\mathbf{p}, \boldsymbol{\alpha}\}$ with a fixed value of B_1 and optimization for B_1 using the obtained $\{\mathbf{p}, \boldsymbol{\alpha}\}$ values. The terms $\boldsymbol{\Lambda}\left(\mathbf{p}, B_1\right)$ and $\boldsymbol{\alpha}$ in Eq. (6.2) are linearly separable. Hence we can use the VARPRO approach to solve for $\{\mathbf{p}, \boldsymbol{\alpha}\}$ [Golub 2003]. The unknown $\boldsymbol{\alpha}$ is linearly associated with $\boldsymbol{\Lambda}$ and can be substituted by $\boldsymbol{\Lambda}\left(\mathbf{p}\right)^+ \mathbf{Y}$, where $\boldsymbol{\Lambda}\left(\mathbf{p}\right)^+$ is the Moore-Penrose generalized inverse of $\boldsymbol{\Lambda}\left(\mathbf{p}\right)$. The VARPRO cost function is therefore computed as:

$$\arg\min_{\mathbf{p}} \left\| \left(\mathbf{I} - \boldsymbol{\Lambda}\left(\mathbf{p}\right) \boldsymbol{\Lambda}\left(\mathbf{p}\right)^+\right) \mathbf{Y} \right\|_2^2 \tag{6.4}$$

where, $\mathbf{I} - \boldsymbol{\Lambda}\left(\mathbf{p}\right) \boldsymbol{\Lambda}\left(\mathbf{p}\right)^+$ is the projector on the orthogonal complement of the column space of $\boldsymbol{\Lambda}\left(\mathbf{p}\right)$. Since $\mathbf{p} \in \mathbb{R}^k$, the Jacobian matrix $\mathbf{J} \in \mathbb{R}^{k \times m}$ and its columns are computed using the results shown in [Golub 2003]. To compute the elements of $\mathbf{J}$, we therefore need to obtain $\partial\Lambda / \partial p_{j_i}$, for all i and j. After solving Eq. (6.4) for $\mathbf{p}$, the values of $\boldsymbol{\alpha}$ are obtained as $\boldsymbol{\Lambda}\left(\mathbf{p}\right)^+ \mathbf{Y}$. Similar to chapter 5, the optimization for $\{\boldsymbol{\alpha}, \mathbf{p}\}$ and B_1 is performed alternatively until convergence. B_1 is optimized using a gradient free optimizer (BOBYQA), as it does not have any closed form solution [Prasloski 2012].

6.2.2 Multi-compartment model using gamma PDF

The previous estimation framework is generic as it does not depend on the chosen PDF. We choose here to use gamma PDF for $f_j(\cdot)$ for $j = \{1,\ 2\ ,3\}$ since their

non-negative support and skewed nature are well suited to describe the compartments used to model the T_2 space. The mean T_2 values of myelin, myelinated axons, inter- and extra-cellular and free fluids in the brain are well studied in the literature [Lancaster 2003, MacKay 2016]. Hence we parameterized each f_j in terms of its mean (μ_j) and variance (v_j) rather than the usual shape and scale parameter representation (refer Eq. (6.5)). Using this parametric form of the gamma PDF makes the choice of optimization bounds convenient.

$$f\left(T_2;\mu_j,v_j\right)=\frac{T_2^{\left(\mu_j^2/v_j\right)-1}}{\Gamma\left(\mu_j^2/v_j\right)\ \left(v_j/\mu_j\right)^{\frac{\mu_j^2}{v_j}}}\exp\left(\frac{-T_2}{v_j/\mu_j}\right) \tag{6.5}$$

Hence we have, $\mathbf{p}=\{\mu_s,\ v_s,\ \mu_m,\ v_m,\ \mu_h,\ v_h\}$ where, $(\cdot)_s$, $(\cdot)_m$ and $(\cdot)_h$ are the PDF parameters describing the short-, medium- and high-T_2 compartments respectively. Due to practical limitations such as feasible acquisition time, coil heating and specific absorption rate (SAR) guidelines, T_2 relaxometry MRI sequences have limitations on the shortest echo time and number of echoes per acquisition. The high-T_2 compartment aims at capturing of free fluids in the brain, and hence has a T_2 relaxation time larger than 1 second [MacKay 2016]. A standard T_2 spin echo multi-echo sequence has the shortest T_2 acquisition (first echo) at around 8-10ms and has 20-40 acquired echoes. Hence for the short-T_2 compartment, we usually have a very limited (around 3-4) number of echoes. There are almost no echoes available which correspond to the high-T_2 compartment. Since there are no echoes with echo time corresponding to the free water, we decided to fix the PDF parameters for the high T_2 compartment. The mean and variance of the gamma PDF for high T_2 compartment (free water) is chosen as 2000ms and 6400ms^2 respectively [MacKay 2016].

The cost function analysis of chapter 5 demonstrated that the robustness and accuracy of the implementations to simultaneously estimate the weights and all the PDF parameters has been found to be not reliable [Layton 2013]. Several previous works have shown that multiple sclerosis lesions cause a shift in the spectrum of the medium T_2 pool (also referred to as mixed pool in [Lancaster 2003]) [Laule 2007b, Laule 2007c]. To evaluate this, we decided to estimate the T_2 pool PDF parameters. It will be interesting to see whether estimated T_2 spectrum from parametric models are able to demonstrate similar phenomenons. Throughout this work, the variances of the short T_2 and medium T_2 pools are fixed as $\{v_s,\ v_m,\ \}=\{50,\ 100,\ \}ms^2$. In the VARPRO formulation of our problem, we are simultaneously estimating the PDF parameters (mean) of short and medium T_2 gamma PDF. It is important to analyze the cost function characteristics before we go ahead with the idea of simultaneous estimation of the PDF parameters. In the next section we perform the cost function analysis in two different ways. In the first experiment we generate the signal using the signal model formulation shown in Eq. (5.1) for known gamma PDF parameters and their associated weights, and study the VARPRO cost function characteristics (shown in Eq. (6.4)) with respect to mean of the gamma PDF representing the short

and medium T_2 compartments. In the next experiment, the VARPRO cost function characteristics is studied for a few voxels of human brain T_2 relaxometry MRI data to confirm the findings from the earlier experiment. Based on the findings of the experiments shown in Section 6.2.3, we propose the final problem setup is Section 6.2.4.

6.2.3 VARPRO cost function analysis

Based on the discussions in the previous section, we evaluated the potential of minimizing the VARPRO cost function with respect to the variable $\mathbf{p}$, where $\mathbf{p} = \{\mu_s, \mu_m\}$. The cost function is evaluated for the following ranges: $\mu_s \in [15, 50]ms$, $\mu_m \in [80, 200]ms$. The range of values chosen for observing the cost function contain the realistic values (and beyond) for each variable.

We studied the cost function for a T_2 relaxometry data of a healthy volunteer. The evaluation is performed a few voxels at different locations in the brain. The cost function is computed for few voxels of a brain image acquired with the following specifications: 3T MRI scanner; 2D multislice CPMG sequence; 32 echoes; first echo at 9ms; echo spacing = 9ms; TR = 3720ms; voxel resolution= 1.33mm ×1.33mm ×4mm; matrix size of 192 × 192; number of averages= 1.

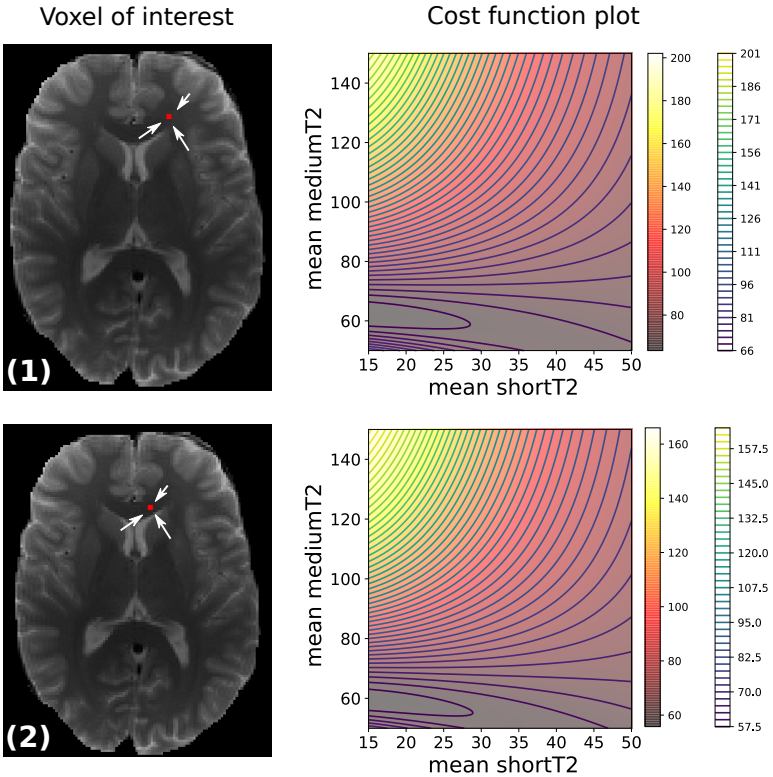

Figure 6.1: VARPRO cost function values for two voxels in the dense white matter region are shown here.

The cost function plots for two voxels in dense white matter region are shown in Fig. 6.1. Both voxels have a similar cost function pattern. These regions of the brain have substantial representation from both short and medium T_2 compartments. Despite this, the cost function plot for both voxels show the difficult nature of optimization with respect to gamma PDF mean of short T_2 and medium T_2 compartments. The cost function plots for two voxels in other regions of the white matter are shown in Fig. 6.2. We observe similar trends for the cost function as those observed for dense white matter shown in Fig. 6.1. Performing optimization for short T_2 gamma PDF mean in bounded intervals shall hit the lower bound for all choices of suitable medium T_2 gamma PDF means. The cost function for a voxel in a free fluid region of the brain is shown in Fig. 6.3. The cost function is vastly flat and there is not clear minima in the reasonable ranges for mean of the gamma PDF representing short T_2 and medium T_2 pools.

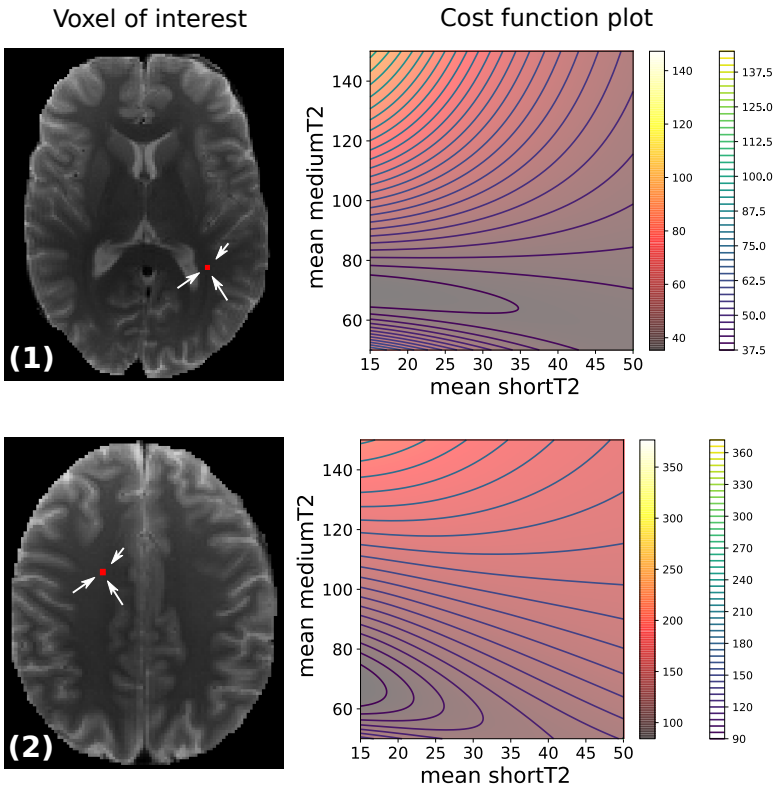

Figure 6.2: VARPRO cost function plots for voxels in other white matter regions.

6.2.4 Problem setup

The cost function plots suggest that when we minimize for short T_2 and medium T_2 PDF mean, the former always hits its lower bound set for the optimization. However, for a fixed value of short T_2 PDF mean, it is viable to estimate the medium T_2 PDF

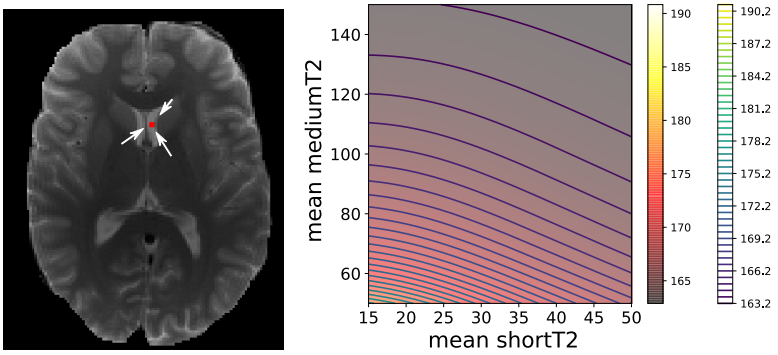

Figure 6.3: The VARPRO cost functions for a voxel in a free water region of the brain tissue.

mean. Hence we choose to estimate only the mean of the gamma PDF corresponding to the medium-T_2 compartment in this chapter.

Using the VARPRO approach we thus estimate four parameters of the signal model: mean of the medium-T_2 gamma PDF (μ_m) and the three weights corresponding to each compartment. In the first step μ_m was estimated and then α was obtained as $\mathbf{\Lambda}^{\dagger}(\mathbf{p})\mathbf{Y}$. The derivation for the Jacobian to be used for our problem has been provided in Appendix B following the approach shown by [Golub 2003]. The specific Jacobian term required to obtain the gradient update step is:

$$J = -\left[\left(P_{\Lambda}^{\perp}\frac{\partial\Lambda}{\partial\mu_m}\Lambda^{\dagger}\right) + \left(P_{\Lambda}^{\perp}\frac{\partial\Lambda}{\partial\mu_m}\Lambda^{\dagger}\right)^{T}\right]Y \tag{6.6}$$

Hence only $\partial\Lambda/\partial\mu_m$ is required for computing the Jacobian matrix. The expression for elements of the matrix $\partial\Lambda/\ \partial\mu_m$ is derived as shown below:

$$\frac{\partial\Lambda_{i,.}}{\partial\mu_m} = \int_{T_2}\frac{\partial f\left(T_2;\mu_m,v_m\right)}{\partial\mu_m}EPG\left(T_2,\triangle TE,i,B_1\right)dT_2 \tag{6.7}$$

where $f(\cdot)$ is the gamma PDF with mean (μ_m) and variance (v_m) (as in Eq. (6.5)). To compute the expression in Eq. 6.7, we need to obtain:

$$\frac{\partial f\left(T_2;\mu_m,v_m\right)}{\partial\mu_m} = \frac{\partial}{\partial\mu_m}\left(\frac{T_2^{\left(\mu_m^2/v_m\right)-1}}{\Gamma\left(\mu_m^2/v_m\right)\ \left(v_m/\mu_m\right)^{\frac{\mu_m^2}{v_m}}}\exp\left(\frac{-T_2}{v_m/\mu_m}\right)\right) \tag{6.8}$$

Substituting $\mu_m/\ v_m = \beta$ in Eq. (6.8), we obtain:

$$\frac{\partial f\left(T_2;\mu_m,v_m\right)}{\partial\mu_m} = \underbrace{\frac{\partial}{\partial\beta}\left(\frac{T_2^{v_m\beta^2-1}}{\Gamma\left(v_m\beta^2\right)}\ \beta^{v_m\beta^2}\exp\left(-\beta T_2\right)\right)}_{\text{A}}\times\overbrace{\frac{\partial\beta}{\partial\mu_m}}^{\text{B}} \tag{6.9}$$

where, A in Eq. (6.9) is solved by using differentiation by parts approach. The term B can be obtained from the definition of β as $1/\ v$. The term A is obtained as shown below:

$$A = \underbrace{\frac{\partial}{\partial\beta}\left[\frac{T_2^{v_m\beta^2-1}}{\Gamma\left(v_m\beta^2\right)}\right]}_{A_1}\ \beta^{v_m\beta^2}\exp\left(-\beta T_2\right) + \frac{T_2^{v_m\beta^2-1}}{\Gamma\left(v_m\beta^2\right)}\ \underbrace{\frac{\partial}{\partial\beta}\left[\beta^{v_m\beta^2}\exp\left(-\beta T_2\right)\right]}_{A_2} \tag{6.10}$$

The expression for A_1 is then obtained as:

$$\begin{aligned}
\frac{\partial}{\partial\beta}\left[\frac{T_2^{v_m\beta^2-1}}{\Gamma\left(v_m\beta^2\right)}\right] &= \frac{\partial}{\partial\left(v_m\beta^2\right)}\left[\frac{T_2^{v_m\beta^2-1}}{\Gamma\left(v_m\beta^2\right)}\right]\ \frac{\partial\, v_m\beta^2}{\partial\beta} \\
&= \left[T_2^{v_m\beta^2-1}\ \frac{-\Gamma'\left(v_m\beta^2\right)}{\Gamma^2\left(v_m\beta^2\right)} + \frac{1}{\Gamma\left(v_m\beta^2\right)}\ T_2^{v_m\beta^2-1}\log T_2\right] \times 2v_m\beta \\
\frac{\partial}{\partial\beta}\left[\frac{T_2^{v_m\beta^2-1}}{\Gamma\left(v_m\beta^2\right)}\right] &= \frac{2v_m\beta}{\Gamma\left(v_m\beta^2\right)}\ T_2^{v_m\beta^2-1}\left[\log T_2 - \Psi\left(v_m\beta^2\right)\right]
\end{aligned} \tag{6.11}$$

where $\Psi(\cdot)$ is the digamma function. The expression for A_2 in Eq. (6.10) is obtained as:

$$\begin{aligned}
\frac{\partial}{\partial\beta}\left[\exp\left(-\beta T_2\right)\ \beta^{v_m\beta^2}\right] &= \beta^{v_m\beta^2}\left(-T_2\right)\exp\left(-\beta T_2\right) + v_m\beta\left(1+\log\beta^2\right)\beta^{v_m\beta^2}\exp\left(-\beta T_2\right) \\
&= \exp\left(-\beta T_2\right)\beta^{v_m\beta^2}\left[-T_2 + v_m\beta\left(1+\log\beta^2\right)\right]
\end{aligned} \tag{6.12}$$

Substituting the results of Eq. (6.11) and (6.12) in Eq. (6.10) we obtain:

$$\begin{aligned}
A &= \frac{2v_m\beta}{\Gamma\left(v_m\beta^2\right)}\ T_2^{v_m\beta^2-1}\left[\log T_2 - \Psi\left(v_m\beta^2\right)\right]\ \exp\left(-\beta T_2\right)\ \beta^{v_m\beta^2} \\
&\quad + \frac{T_2^{v_m\beta^2-1}}{\Gamma\left(v_m\beta^2\right)}\ \left[-T_2 + v_m\beta\left(1+\log\beta^2\right)\right]\ \exp\left(-\beta T_2\right)\beta^{v_m\beta^2} \\
&= \underbrace{\frac{T_2^{v_m\beta^2-1}}{\Gamma\left(v_m\beta^2\right)}\ \beta^{v_m\beta^2}\exp\left(-\beta T_2\right)}_{f\left(T_2;\,\mu,\,v_m\right)}\ \times \\
&\qquad \left[2v_m\beta\left(\log T_2 - \Psi\left(v_m\beta^2\right)\right) - T_2 + v_m\beta\left(1+\log\beta^2\right)\right]
\end{aligned} \tag{6.13}$$

Now, substituting the above result in Eq. (6.9) we obtain the expression of $\partial f/\partial\mu_m$ as:

$$\begin{aligned}
\frac{\partial f\left(T_2;\mu_m,v_m\right)}{\partial\mu_m} &= f\left(T_2;\mu_m,v_m\right)\left[2v_m\beta\left(\log T_2 - \Psi\left(v_m\beta^2\right)\right) - \right. \\
&\qquad \left. T_2 + v_m\beta\left(1+\log\beta^2\right)\right] \times \frac{1}{v_m} \\
&= f\left(T_2;\mu_m,v_m\right)\left[\beta\left(2\log\left(T_2\beta\right) - 2\Psi\left(v_m\beta^2\right) + 1\right) - \frac{T_2}{v_m}\right]
\end{aligned} \tag{6.14}$$

Substituting $\beta = \mu_m / v_m$ in the above equation, we obtain the final result as follows:

$$\frac{\partial f(T_2;\mu_m,v_m)}{\partial \mu} = f(T_2;\mu_m,v_m)\left[\frac{\mu_m}{v_m}\left(2\log\left(T_2\frac{\mu_m}{v_m}\right) - 2\Psi\left(\frac{\mu_m^2}{v_m}\right)+1\right) - \frac{T_2}{v_m}\right]$$

Hence, the term to be computed to obtain the jacobian is shown below:

$$\frac{\partial \Lambda}{\partial \mu_m} = \int_0^\infty f(T_2;\mu_m,v_m)\left[\frac{\mu_m}{v_m}\left(2\log\left(T_2\,\frac{\mu_m}{v_m}\right) - 2\Psi\left(\frac{\mu_m^2}{v_m}\right)+1\right) - \frac{T_2}{v_m}\right] EPG(T_2,\triangle TE,i,B_1)\,dT_2 \tag{6.15}$$

We assumed a reasonable bound on μ_m of $[95ms, 150ms]$ for its optimization. The FAE percentage was optimized for in the range of 0% to 50%. The minimization problem in Eq. (6.4) is solved for μ_m with a gradient based optimizer [Svanberg 2002] using the analytically obtained derivative in Eq. (6.15) .

Interpretation of the compartment weights. The short T_2 compartment here indicates the condition of myelin and myelinated axons [Lancaster 2003]. The medium T_2 compartment's water fraction conveys information on the condition of axons, glial cells and extracellular fluids [Lancaster 2003]. The condition of free fluids (such as in ventricles and fluid accumulation due to tissue injuries) is indicated by the high T_2 water fraction values.

6.3 Experiments

The first experiment is conducted on synthetic data to assess the performance of the proposed method on data with known ground truth. The next experiment is performed on an in-vivo phantom with multiple spheres containing mono T_2 solutions. In the third experiment we evaluate the repeatability of the proposed method by evaluating it on test-retest scans obtained for 4 healthy controls. In the final experiment we apply our method on a MS patient and observe the water fraction maps and study its relevance with the known pathology of MS lesions.

6.3.1 Synthetic data

A multi-compartment T_2 relaxometry voxel was generated with known ground truth with various levels of signal to noise ratios (SNR) to evaluate the proposed method. The voxel is simulated with a short T_2, medium T_2 and high T_2 water fraction values of 0.25, 0.74 and 0.01 respectively. A total of $N = 100$ T_2 curves are combined in proportion of the stated water fraction values to create the multi-compartment T_2 relaxometry voxel. To do so, the T_2 values for the short T_2, medium T_2 and high T_2 compartments are chosen from a Gaussian distribution with mean of $25ms$, $125ms$, $1000ms$ and standard deviation of $5ms$, $20ms$, $80ms$ respectively. The stimulated

echoes were accounted for using the EPG algorithm. A flip angle error value of 10% was used for the synthetic data. The echo spacing and number of echoes was chosen as $9ms$ and 32 for the simulations. Evaluations were performed for 10 SNR values ranging from 50 to 150. Noise was introduced as additive white Gaussian noise and the SNR was considered with respect to the signal observed at the first echo. We performed 1000 simulations for each SNR level. The multi-compartment voxel was regenerated for each simulation to maintain the randomness of the choice of T_2 values corresponding to each compartment. We observed the estimation performance of all three water fractions over the SNR levels.

6.3.2 In-vivo phantom data

In this experiment we tested our method against the NIST phantom, "Phannie" [Russek 2012]. The phantom has been shown in Fig. 6.4.

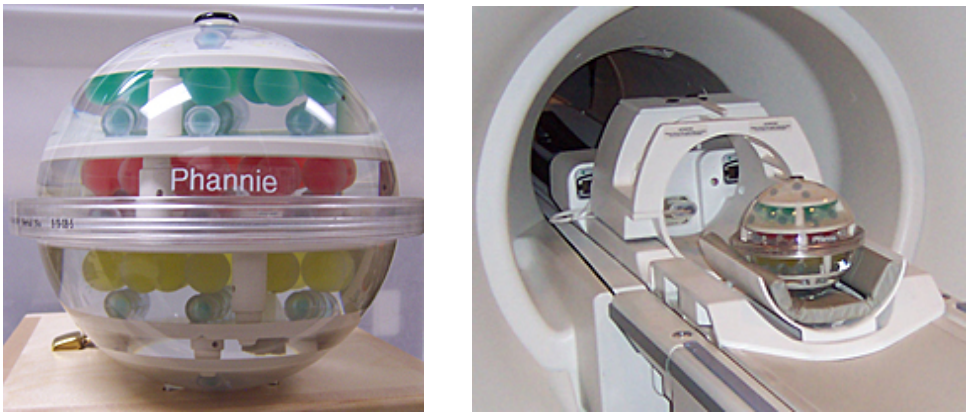

(a) (b)

Figure 6.4: The NIST phantom "Phannie". Images source: https://www.nist.gov/news-events/news/2010/05/meet-phannie-nists-standard-phantom-calibrating-mri-machines

As it can be observed from Fig. 6.4a, the phantom contains three layers of spheres. The middle layer (red spheres) consists of spheres containing solutions of varying T_2 relaxation times. The in-vivo T_2 values for the scanner at our research center were found using mono T_2 analysis. The values ranged from around 10 ms to 700 ms. A mono T_2 estimation was performed to know the T_2 values of the solution in each sphere. The water fraction values for the short T_2, medium T_2 and high T_2 were performed for these spheres.

There are two main objectives of this experiment:

- *Objective 1:* The NIST phantom spheres contain mono T_2 solutions. Hence the first objective is to evaluate the performance of the multi-compartment T_2 relaxometry model in such scenarios.

- *Objective 2:* Few spheres have T_2 values which do not lie in whether compartment clearly. Hence the other objective of the experiment is to observe whether and the manner in which the water fraction values estimated for the spheres reflect the changing T_2 values of the solution in the spheres.

The acquisition details are as follows: Siemens 3T MRI machine; 2D multislice CPMG sequence; number of echoes = 32; first Echo at 9ms; echo spacing = 9ms; single slice acquisition; in plane resolution = 1.33mm × 1.33mm; slice thickness = 3mm; matrix size = 192 × 192.

6.3.3 Repeatability test

The objective of this experiment is to observe whether the proposed model is repeatable in terms of estimation of the microstructure maps. For that purpose, test retest T_2 relaxometry scans of 4 healthy controls were obtained to evaluate the repeatability of the proposed method. The age of the healthy controls was in the range of 26-32 years.

15 regions of interests (ROIs) were marked in the brain for each healthy control over which the test and retest values of the compartments' water fractions were compared. All the ROIs were marked for one case. The ROIs were then registered on the other cases using a rigid followed by an affine registration [Ourselin 2000, Commowick 2012] to ensure that similar regions were analyzed for repeatability in all cases. An illustration of these ROI on a subject is shown in Fig. 6.5.

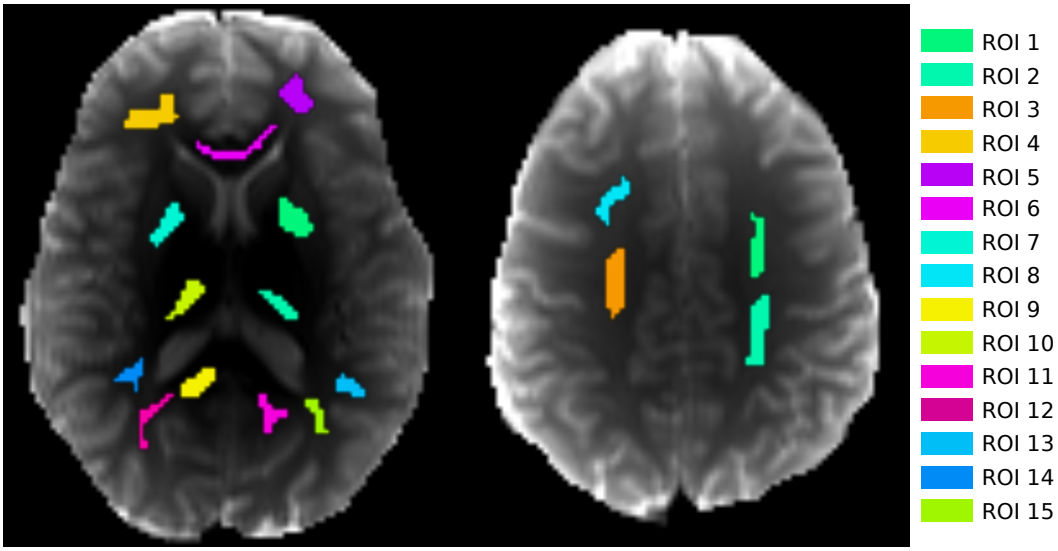

Figure 6.5: Test retest scans were performed for 4 healthy controls to study the repeatability of the proposed method. This figure shows the 15 regions which were marked on the healthy controls over which the repeatability was studied.

The details of the acquired data are as follows: 3T MRI scanner; 2D multislice

CPMG sequence; 32 echoes; first echo at $9ms$; echo spacing = $9ms$; TR = $2000ms$; single slice acquisition; in plane resolution = $1.1mm \times 1.1mm$; slice thickness of $5mm$; matrix size of 192×192; number of averages = 1. The data was acquired on the same day. The subject was moved out and then placed back in the scanner to acquire the test and the retest data.

A Bland-Altman plot was used to measure the agreement between the mean of estimated water fraction values in the 15 ROIs. For voxel wise comparison, regression statistics were studied for a scatter plot between the estimated water fraction values of the test and retest data for all voxels in the ROIs.

6.3.4 Multiple sclerosis patient data

In the final experiment we studied the estimated maps for a multiple sclerosis patient. This experiment is only intended at studying the potential of the proposed method for MS. Demyelination and inflammation in and around MS lesions is a well known phenomenon. In these contexts, the estimated medium T_2 PDF mean and water fraction maps are studied. The estimated medium T_2 PDF mean can provide leads into whether the T_2 spectrum estimation has the potential to provide more insights into MS lesions.

The details of the acquired data are as follows: 3T MRI scanner; 2D multislice CPMG sequence; 32 echoes; first echo at $9ms$; echo spacing = $9ms$; TR = $2000ms$; single slice acquisition; in plane resolution = $1.1mm \times 1.1mm$; slice thickness of $5mm$; matrix size of 192×192; number of averages = 1.

6.4 Results

6.4.1 Synthetic Data

The results of synthetic data are shown in Fig. 6.6. The experiments are done for various levels of SNR. It shows that with increasing SNR the weight estimation gets more accurate. The red line in the plots show the true value. It can be observed that for all levels of SNR, the true values are quite close to the true value. The variation in the estimation over 1000 simulations reduce with increasing SNR for short T_2, medium T_2 and high T_2 water fractions.

6.4.2 In-vivo phantom data

It shall be noted that the spheres in the NIST phantom contain mono T_2 solutions. The T_2 values of the spheres were estimated using a mono T_2 estimation. The T_2 relaxometry image of the first echo of the phantom and the estimated water fraction maps are shown in Fig. 6.7. The spheres are annotated for identification using a label index number as shown in the leftmost figure of Fig. 6.7 for convenience of discussion and analysis. The T_2 values of the spheres obtained using mono T_2 estimation are shown in Table 6.1.

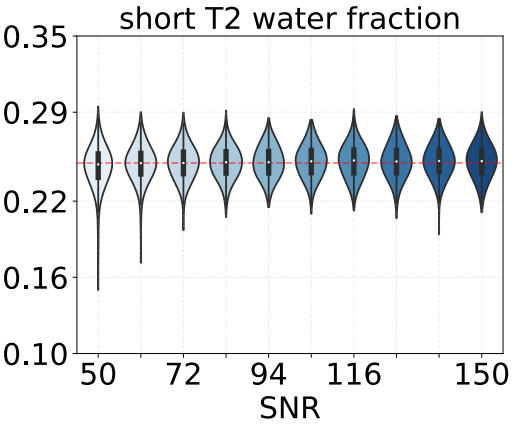

(a) Short T_2 water fraction

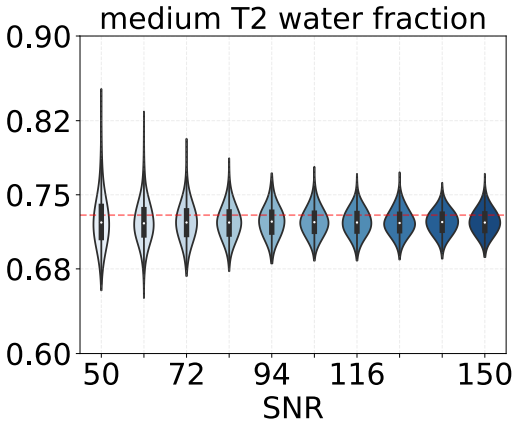

(b) Medium T_2 water fraction

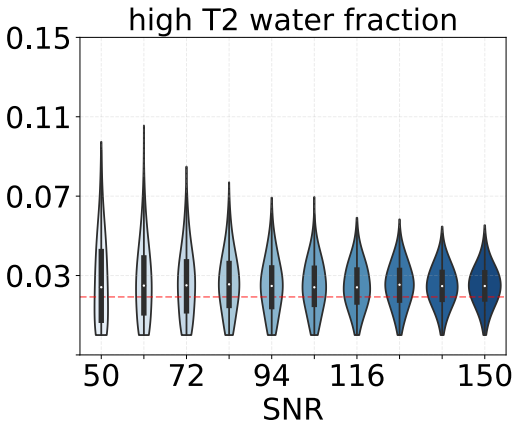

(c) High T_2 water fraction

Figure 6.6: The plots show distribution of the estimated values over 1000 iterations for each SNR of the synthetic data. The red line shows the true value for each case.

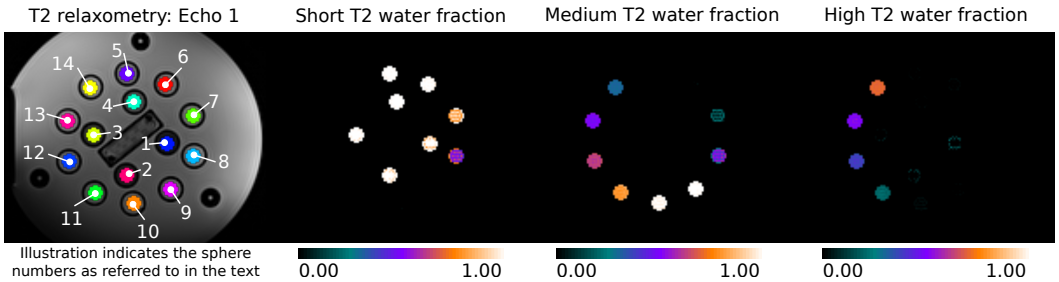

Figure 6.7: (Left to right) First echo of the T_2 relaxometry data is shown with label annotations. The estimated water fractions maps for short T_2, medium T_2 and high T_2 compartments are shown here.

It can be seen that spheres with T_2 values lower than 40ms (i.e. spheres 1 to 6) have a short T_2 water fraction value of 1.0. The short T_2 water fraction value is zero

Label	*1*	*2*	*3*	*4*	*5*	*6*	*7*
T_2 value (ms)	31.84	21.92	16.56	19.56	26.07	34.79	47.59
Label	*8*	*9*	*10*	*11*	*12*	*13*	*14*
T_2 value (ms)	65.59	91.64	130.64	200.02	286.89	378.11	603.03

Table 6.1: The T_2 values of the spheres of the NIST phantom (refer Fig. 6.7) are shown here. The values are obtained by performing a mono T_2 estimation from the T_2 relaxometry data. The label values correspond to the annotations in Fig. 6.7.

for sphere number 8 and above. The medium T_2 water fraction values have non-zero values for sphere number 7 (i.e. $T_2 = 47.8ms$) and above. The high T_2 water fraction value is zero for all spheres with T_2 value less than $200ms$. The estimated water fraction values are plotted with respect to the T_2 value of each sphere in Fig. 6.8. We can observe that the multi-compartment model is able to successfully identify spheres where only one component is present. The estimated water fractions change with increasing T_2 values in an expected manner.

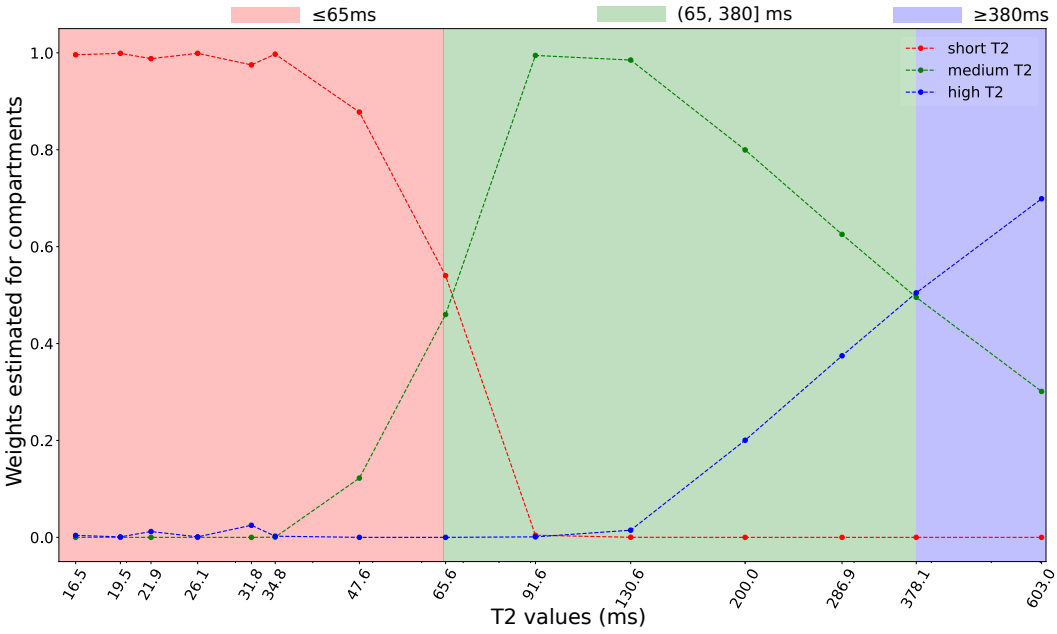

Figure 6.8: The water fraction values estimated is plotted against the T_2 values of each sphere of the NIST phantom containing mono T_2 solution. The red region in the graph denotes the T_2 values where the estimated short T_2 water fraction is greater than or equal to all other weights. In a similar manner, the green and blue regions correspond to the estimated medium T_2 and high T_2 water fraction being greater than the others respectively.

6.4.3 Repeatability test

The repeatability of the proposed method was evaluated on 15 white matter ROIs in four healthy controls. The ROIs evaluated are shown in Fig. 6.5. Two evaluation criteria were used to assess the repeatability of the method.

In the first criteria the test-retest estimation values of the mean of 15 ROIs is compared using a Bland-Altman (BA) plot. From the plot we observed the mean bias in the estimation (b) and the 95% confidence interval around it ($CI_{95\%}$) and the limits of agreement (LoA) of the test-retest estimation. The LoA is computed as $b \pm 1.96 \times SD$, where SD is the standard deviation of the observations. The 95% confidence interval around the LoA is also shown in BA plots. The 95% confidence interval around the mean bias and LoA are computed as discussed in [Lévy 2018].

In the second criteria we performed a voxel wise comparison of the values in the 15 ROIs of 4 healthy controls. The linear regression was performed on all voxels of the ROIs. Regression statistics were computed for the scatter plots between the water fraction estimates for test-retest data. The slope and intercept of the linear regression fit and their correlation coefficient $\left(R^2\right)$ fit score were observed.

The BA and scatter plots for short T_2, medium T_2 and high T_2 water fraction repeatability experiments are shown in Fig. 6.9a, 6.9b and 6.9c respectively. The shaded regions around the mean bias and LoA are shown with their respective 95% confidence intervals. In the scatter plot voxels belonging to different ROIs are represented with varying shades. The ROI labels indexes correspond to the ones shown in Fig. 6.5. The scatter plots show the actual regression fit, as well as the ideal fit (i.e. slope=1 and intercept=0). The BA plot and linear regression analysis statistics are summarized in Table 6.2 and 6.3 respectively. The mean bias for estimates of all three water fractions are close to zero and it confidence intervals contain zero level in all cases as well. The regression analysis shows that the slope and intercept of all the estimates are close to an ideal fit with a high R^2 (> 0.864).

The water fraction maps estimated for a few axial slices for a healthy control are shown in Fig. 6.10. We observed high values of short T_2 water fraction at deep brain gray matter. This is however attributed to the iron rich nature of the region and has been observed to have fast decaying T_2 curves.

Water fraction	*Mean bias (m_d)*	*95% CI around m_d*	*LoA*
Short T_2	-0.0007	$[-0.0075, 0.0059]$	0.0239
Medium T_2	-0.0009	$[-0.0076, 0.0056]$	0.0234
High T_2	0.0001	$[-0.0006, 0.0009]$	0.0002

Table 6.2: Statistics of the Bland-Altman (BA) plots shown in Fig. 6.9 for short, medium and high-T_2 water fraction estimates respectively. For each compartment the mean bias of the difference in the estimates (m_d), the 95% confidence interval (CI) around m_d and the limits of agreement (LoA) are shown.

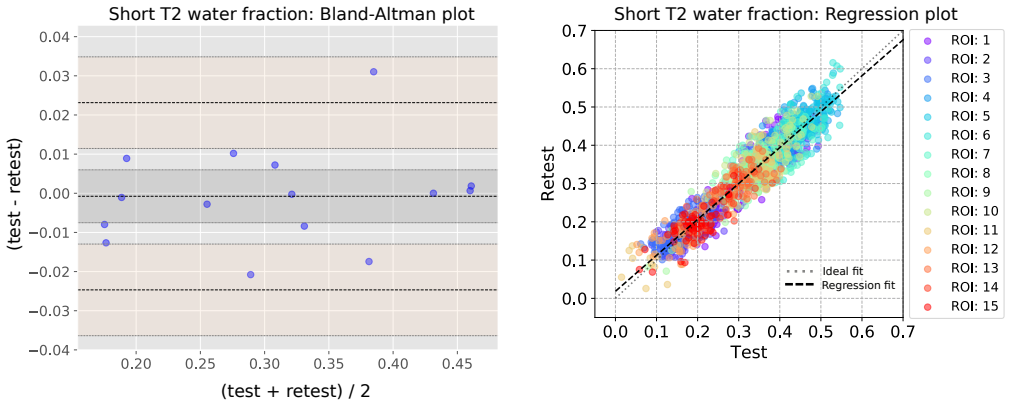

(a) Short T_2 water fraction

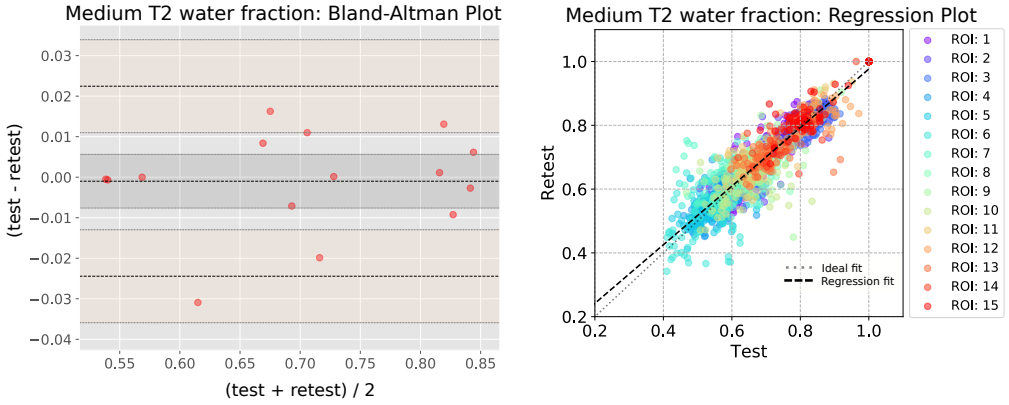

(b) Medium T_2 water fraction

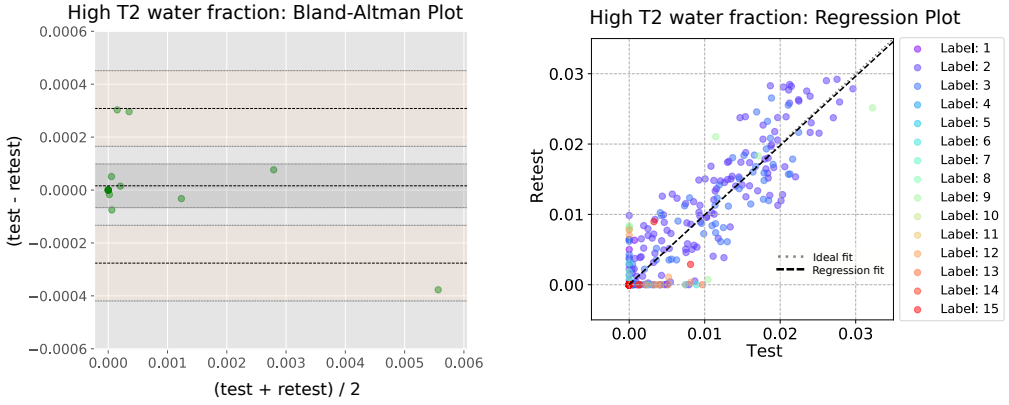

(c) High T_2 water fraction

Figure 6.9: The repeatability of the water fraction estimation in four healthy controls are compared over 15 ROIs (refer Fig. 6.5) using Bland-Altman plot (where ROI means are compared) and voxel-wise regression plot. The repeatability results for short T_2, medium T_2 and high T_2 water fraction estimations are shown in Fig. 6.9a, 6.9b and 6.9c. The Bland-Altman and regression plot statistics for the plots shown here are summarized in Table 6.2 and 6.3 respectively.

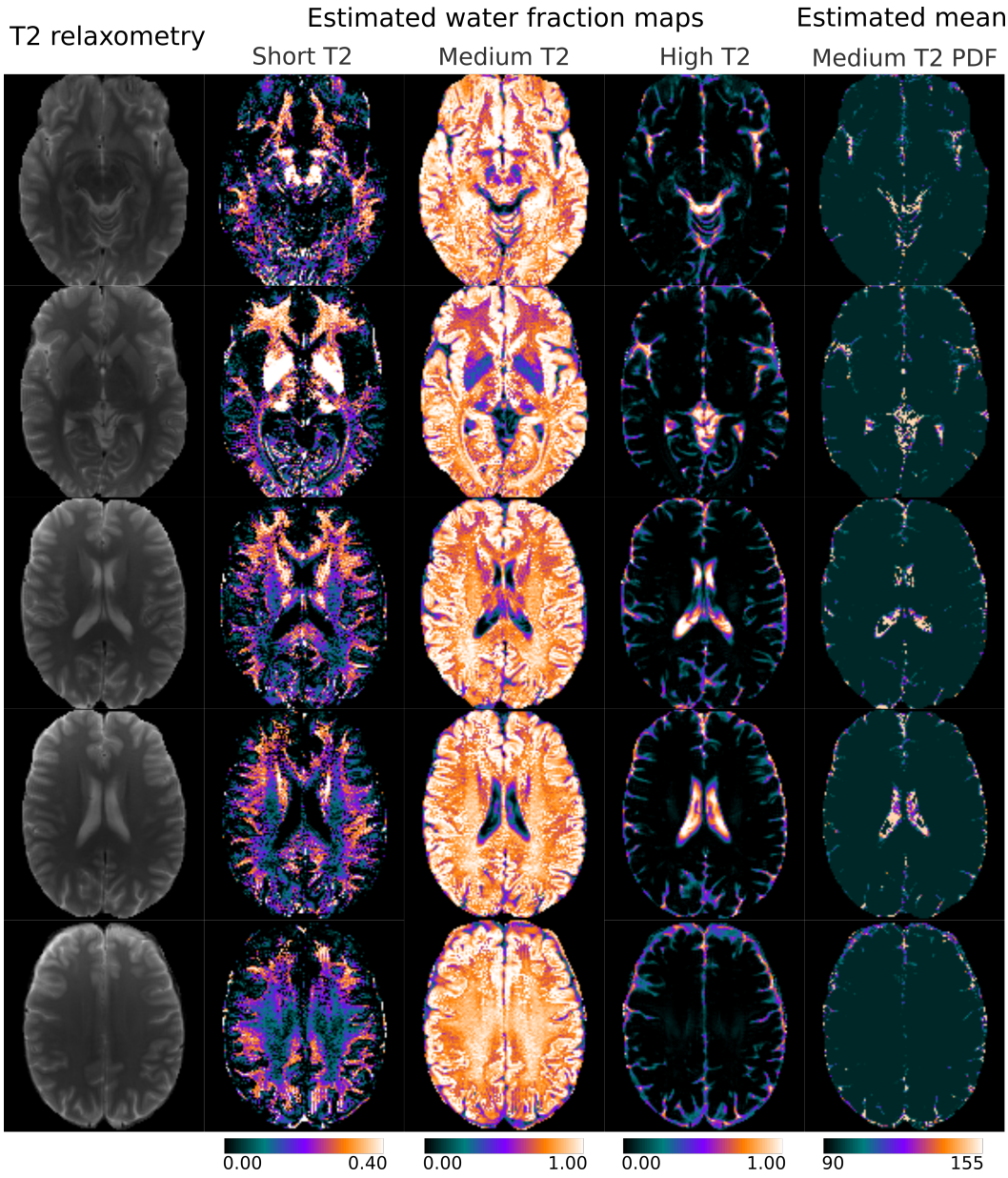

Figure 6.10: The estimated water fraction maps for five axial slices of a healthy control are shown here. The acquired data had following specifications: echo spacing = 9ms, 32 echoes, repetition time = 3720ms, voxel resolution = 1.3mm×1.33mm×4.0mm, matrix size = 192×192.

Water fraction	R^2	*Slope*	*Intercept*
Short T_2	0.904	0.938	0.018
Medium T_2	0.864	0.918	0.058
High T_2	0.886	0.986	0.000

Table 6.3: Regression statistics of the plots shown in Fig. 6.9 for short, medium and high-T_2 water fraction estimates. The regression statistics are obtained by comparing all the voxels in the 15 ROIs of four healthy controls.

6.4.4 Multiple sclerosis patient case

The estimated water fractions and medium T_2 gamma PDF mean for the MS patient case are shown in Fig. 6.11. There are multiple lesions present in the patient. Absence of short T_2 water fraction values in and around the lesions suggests demyelination in the lesion and its surroundings. The medium T_2 water fraction values are also higher as compared to the observations from healthy control water fraction maps. This might be attributed to the presence of increased extra and intracellular matters in the regions undergoing demyelination. The medium T_2 PDF mean map provides information on the spectrum of medium T_2 compartment. The lesion regions clearly have a higher gamma PDF mean as compared to the normal appearing white matter.

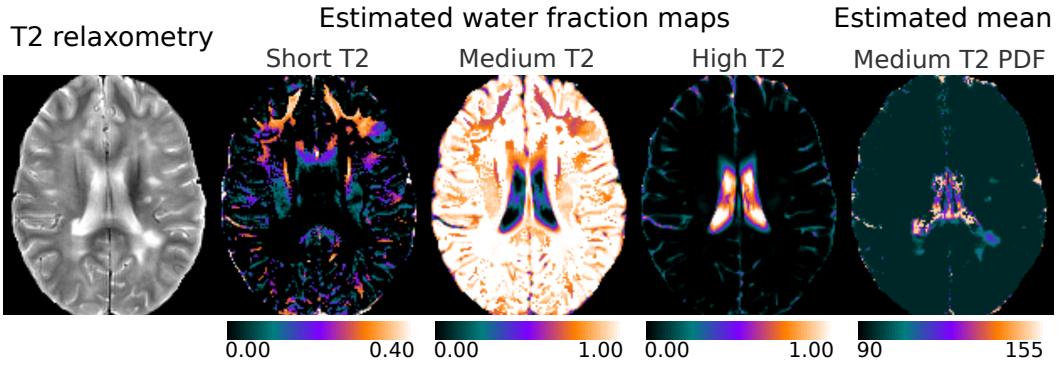

Figure 6.11: The estimated water fraction maps and medium T_2 gamma PDF mean are shown here for a patient with MS lesions.

The medium T_2 gamma PDF mean increases as we approach the center of the lesion from its boundary. This is further explored in Fig. 6.12. For two lesions, we observe the change in medium T_2 mean values along a line profile. For each example, the direction of the profile starts from label indexed as 1 and increases along the direction illustrated in the figures. In general, the indexes start from normal appearing white matter and then traverses the lesion. In the first example (refer Fig. 6.12a) we observe that the medium T_2 gamma PDF mean increases as we

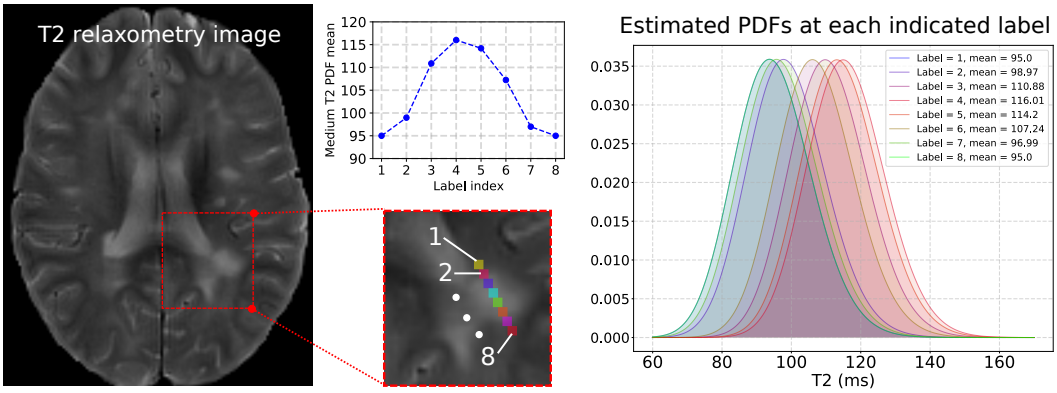

(a) Example 1

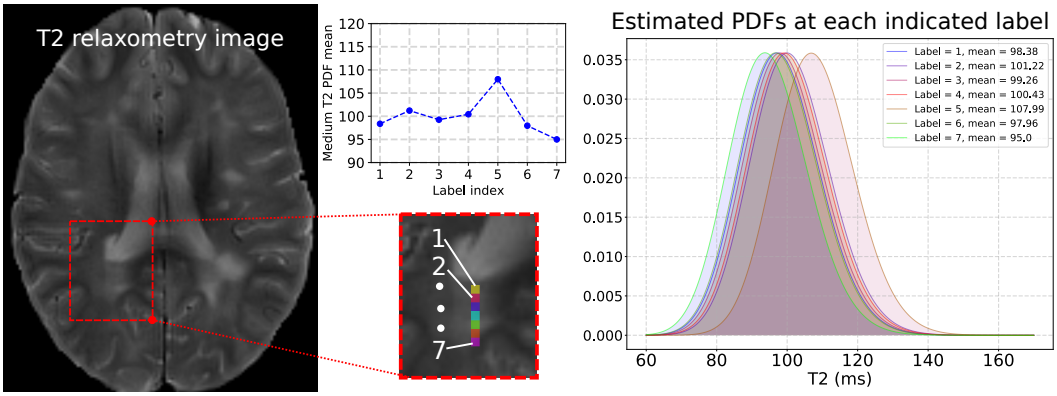

(b) Example 2

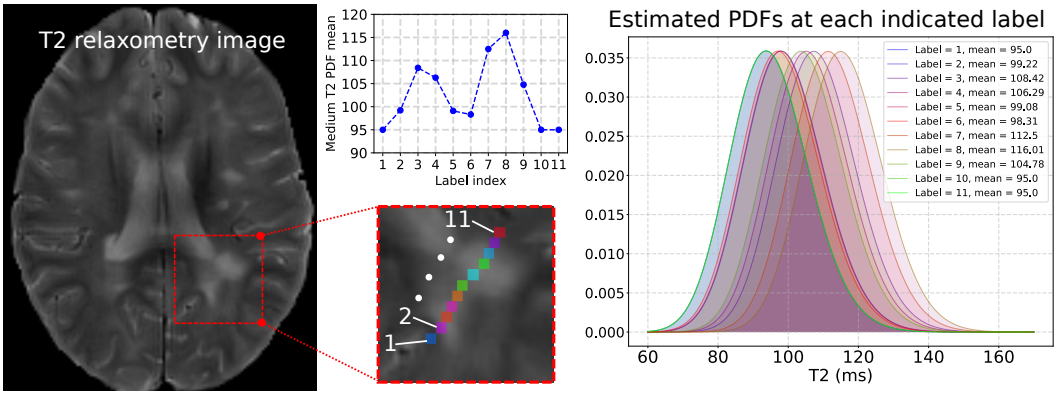

(c) Example 3

Figure 6.12: The medium T_2 gamma PDF mean are observed along a line profile shown for each of the three MS lesion examples shown here. For each example, the medium T_2 PDF mean is plotted against the label indexes to observe its trend as the lesion is traversed. The gamma PDFs are also plotted for each index to observe the shift in the spectrum of the medium T_2 compartment.

approach the inner lesion regions, and then gradually decreases as we exit the lesion and enter normal appearing white matter region. The gamma PDFs are plotted corresponding to the label indexes to show the shift in the location of the medium T_2 spectrum. In the second example (refer Fig. 6.12b) we look at the shift in spectrum for a relatively smaller lesion. The highest medium T_2 PDF mean observed in this example is around $108ms$. It is lower compared to what was observed in example 1 ($\approx 116ms$). In the last example (refer Fig. 6.12c) we observe a profile which traverses two lesions very close to each other. The larger lesion in example 3 is the same as the one shown in the first example. We can see two peaks in the medium T_2 gamma PDF mean as we move along the profile. However, the peak values are different.

6.5 Discussion

We adopted a variable projection approach to estimate parameters of a parametric multiple compartment T_2 relaxometry model and its associated weights. The cost function analysis of the parametric multiple compartment T_2 relaxometry model revealed the difficult nature of simultaneously estimating multiple PDF parameters. Although it is feasible to perform such multi-parameter estimation, it is not trivial and might be always converging to the (upper or lower) bound set for the optimization framework. Based on our analysis, the parameters of the short T_2 and high T_2 compartments are fixed and the mean of medium T_2 compartment is optimized for in the problem setup.

The validation on synthetic data shows that the accuracy of estimation improves with increasing SNR. The simulation was performed in a comprehensive framework. 1000 estimations were performed for each SNR level, where the multi-compartment T_2 voxel was generated for each one from randomly sampled T_2 values from each compartment. The healthy volunteer and multiple sclerosis patient data analyzed in this work had SNR range of around 100 (depending on the measurement region). The SNR was measured using ROI based method. Appropriate correction for non-Gaussian nature of the background noise was performed for the SNR measurements [Henkelman 1985].

Repeatability is an important aspect of quantitative MRI biomarkers. Test-retest experiments showed good agreement between the quantitative estimation maps of test and retest data. No systematic bias is observed in the test-retest quantitative estimates.

The estimation maps for the MS patient showed indications of demyelination in and around the lesion. These regions also showed elevated levels of medium T_2 water fraction values indicating an increased presence of extra-cellular matters in the lesion regions as compared to normal appearing white matter regions of the brain. These observations are in agreement with the MS lesion pathological studies where degeneration of myelin and an increased presence of extracellular matters (such as glial and astrocytes cell bodies) and cellular debris deposition in brain tissues affected by MS lesions have been observed [Lassmann 2001]. An important

aspect of this work was to evaluate the T_2 spectrum of the compartments and whether it provides extra insights into brain tissue microstructures. In our work, we estimated the parameter for T_2 spectrum of the medium T_2 compartment. It provided useful insights in the MS case study. The MS lesion regions are known to undergo axonal degeneration post demyelination. Since MS lesions are focal lesions, the degeneration is expected to be higher in the inner regions of the lesion. The water bound to the injured white matter tissues would hence be loosely bound compared to water in normal appearing white matter tissues. There is also a higher presence of extra-cellular matters in the MS lesion regions. All these phenomenons should lead to shift in the peak of the spectrum of the medium T_2 compartment. This shall explain the observed gradual increase in the mean of the medium T_2 gamma PDF as we approached the inner regions of the lesion from its boundary. This observation is similar to what [Laule 2007b, Laule 2007c] observe in their work using multi-component T_2 relaxometry model. The highest medium T_2 mean observed for each lesion also varies. This variability observed in the medium T_2 spectrum of different MS lesions in the same patient can be attributed to the already known heterogeneity of the MS lesions [Lassmann 2001, Barillot 2016] (both intra-patient and inter-patients).

From experiments performed on MS data with fewer echoes, it has been found that this method is reliable for data acquired with a final echo time of greater than $200ms$. This allows sufficient number of observations for fitting the medium T_2 PDF parameters. However, acquiring T_2 relaxometry data with large number of echoes (typically around 32) is time consuming. Hence such implementations might not be favorable in a clinical setting. The medium T_2 PDF mean for white matter regions hit the lower bound set for it in our method. This is however not surprising from what we observed from the cost function plots of the white matter voxels. However, the medium T_2 PDF mean is found to be valuable in regions of the brain with pathologies, or regions with sufficiently high T_2 value (such as CSF and neighboring partial volume regions). The proposed method was demonstrated on one MS patient case. In the future work we plan to evaluate the method on a larger MS patient dataset.

Part III

Applications

Chapter 7

Longitudinal study of multi-compartment T_2 relaxometry model biomarkers in MS lesions of patients with CIS

Contents

7.1 Introduction

In this chapter, we show application of the method Gaussian multi-compartment T_2 relaxometry model proposed in Chapter 5 on MS patients. We reported observations on the evolution of the quantitative markers obtained from the model in enhancing (MS lesion regions undergoing active blood brain barrier breakdown) and non-enhancing MS lesion regions. Vavasour et al. studied the myelin water fraction and total water content in three new MS lesions in two patients over a year [Vavasour 2009]. Levesque et al. studied evolution of myelin water fraction and geometric mean of T_2 values of gadolinium enhancing lesions in five MS patients over a period of one year [Levesque 2010b]. Although myelin water fraction was found to be quite informative in suggesting changes in active lesions, the geometric mean T_2

values was sensitive to changes in the active lesions. Vargas et al. studied myelin water fraction of gadolinium enhanced and non-enhanced lesions [Vargas 2015]. Measurements were compared for two scans with median duration of around 6 months between them. Authors found that contrary to the non-enhancing lesions, there was significant improvement in myelin water fraction of enhancing lesions between the two scans. Vargas et al. also mention that myelin water fraction is a combined measure of edema and demyelination [Vargas 2015]. The myelin water fraction is a relative measure and a change in its values should be studied in conjunction with the remaining water fraction measures. In our analysis, we observed and compared the change in water fractions of tissues with short, medium and high T_2 values in enhancing and non-enhancing regions of lesions in 10 MS patients over a period of 3 years. The study on the MS patients was a retrospective one. The protocol used for the MS study was different from the ones on which the repeatability experiments were performed. Hence, the water fraction estimations were compared for a T_2 relaxometry data with standard acquisition parameters (32 echoes with echo spacing of $9ms$) to that of the one used for MS study using a synthetic phantom experiment.

7.2 Method and data

7.2.1 Signal model and estimation framework

The short T_2, medium T_2 and high T_2 compartments are defined as mentioned in Chapter 5. Each T_2 relaxometry voxel is considered to be composed of tissues with short T_2, medium T_2 and high T_2 relaxation times. The compartments are defined as Gaussian PDFs. The T_2 relaxometry signal ($s(t_i)$) at each voxel at i-th echo time (t_i) is modeled as shown below:

$$s(t_i) = \sum_{j=1}^{3} \alpha_j \left[\int_0^{\infty} f_j(T_2; \mu, \sigma)\, EPG(T_2, \triangle TE, i, B_1)\, dT_2 \right] \tag{7.1}$$

where $t_i = i \times \Delta TE$; ΔTE is the echo spacing of the T_2 relaxometry data; the flip angle error percentage (FAE) is realized as B_1 scale factor; $EPG(\cdot)$ is the stimulated echo computed as in [Layton 2013]; $f_j(\cdot)$ is the Gaussian PDF representing each T_2 compartment. The means and variances for the short T_2, medium T_2 and high T_2 PDF are $\{\ 20ms,\ 100ms,\ 2000ms\}$ and $\{\ 25ms^2,\ 100ms^2,\ 6400ms^2\}$ respectively. The optimization problem is therefore as shown below:

$$\begin{aligned} \left(\hat{\alpha}, \hat{B_1}\right) &= \underset{\boldsymbol{\alpha}, B_1}{\arg\min} \sum_{i=1}^{m} \left(y_i - s(t_i)\right)^2 \\ &= \underset{\boldsymbol{\alpha}, B_1}{\arg\min} \left\| \mathbf{Y} - \boldsymbol{\Lambda}(B_1)\, \boldsymbol{\alpha} \right\|_2^2 \end{aligned} \tag{7.2}$$

where y_i is the observed signal at i-the echo; $\boldsymbol{\alpha} \in \mathbb{R}^{+3}$. Each element of $\boldsymbol{\Lambda} \in \mathbb{R}^{+m\times 3}$ in Eq. (5.6) is computed as:

$$\lambda_j\left(t_i; B_1\right) = \int_0^\infty f_j\left(T_2; \mathbf{p}\right) EPG\left(T_2, \triangle TE, i, B_1\right) dT_2 \tag{7.3}$$

$EPG(\cdot)$ does not have a closed form solution. However, B_1 and $\boldsymbol{\alpha}$ are linearly separable. Hence, B_1 and $\boldsymbol{\alpha}$ are optimized alternatively. In the first step, $\boldsymbol{\alpha}$ is computed by non-negative least square optimization [Lawson 1995] for a fixed B_1. In the next step, B_1 is numerically optimized for using a gradient free optimizer (BOBBYQA) and the weight values are maintained as found from the earlier step. This alternate optimization is performed till we obtain the required convergence. Finally, the respective weight are obtained as $w_j = \alpha_j / \sum_i \alpha_i$ for $j = \{1, 2, 3\}$. The method has been explained in more detail in Section 5.2 of Chapter 5.

7.2.2 Data

We studied 10 MS patients over a period of 36 months. All patients included in this study had an episode of clinically isolated syndrome (CIS). The patient cohort included equal number of male and female subjects and their median age was 28 years. Data was acquired at eight time points over a period of 36 months. An acquisition at the baseline was followed by acquisitions at 3, 6, 9, 12, 18, 24 and 36 months from the baseline. The lesions in patient scans were marked by an expert radiologist on T_2 weighted images at the baseline. All participants were informed and provided their written consent for the study.

Acquisition details All data was acquired on a 3T MRI scanner. The acquisition details for the T_2 relaxometry data are as follows: 2D multislice CPMG sequence; 7 echoes; first echo at 13.8ms; $\triangle TE$ = 13.8ms; TR = 4530ms; voxel dimensions = $1.3 \times 1.3 \times 3.0$ mm^3; spacing between slices of 3mm; matrix size of 192×192; number of averages = 1; acquisition time $\approx$ 7 minutes. A T_1 weighted scan was obtained post gadolinium injection to identify the lesions undergoing active blood brain barrier breakdown. The post Gadolinium injection (0.1mmol/kg gadopentate dimeglumine) acquisition details are as follows: transverse spin echo T_1 weighted images; voxel dimensions = $1.0 \times 1.0 \times 3.0$ mm^3; spacing between slices of 3mm; matrix size of 256×256; number of averages = 1. The protocols were approved by the institutional review board of Rennes University Hospital.

7.3 Experiments

7.3.1 Synthetic phantom experiment

Repeatability experiments in chapter 5 were conducted on a T_2 relaxometry data with 32 echoes with an echo spacing of $9ms$. However, the MS data being analyzed

has 7 echoes with an echo spacing of $13.8ms$ as data from a retrospective study was used for the longitudinal study. In this experiment we compared the estimation performance for: (i) *Protocol A*: echo spacing/number of echoes = $9ms/32$ and (ii) *Protocol B*: echo spacing/number of echoes = $13.8ms/7$. The repeatability experiments were performed using Protocol A in Chapter 5. The synthetic phantom data generated as explained in Appendix A was used for this purpose. The true water fraction and flip angle error (FAE) percentage of the synthetic phantom is shown in Fig.!7.1. The phantom has five sections with a variety of water fraction values. The phantom sections are annotated in Fig. 7.2 and the corresponding true water fraction values are shown in Table 7.1.

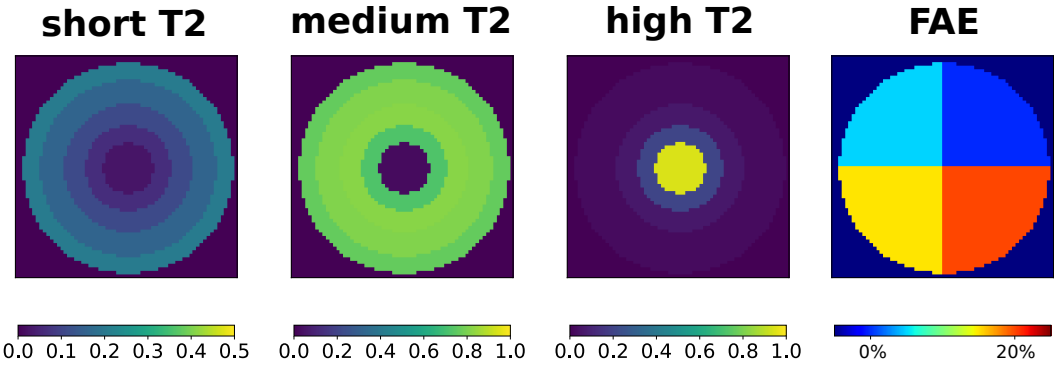

Figure 7.1: True values of the flip angle error (FAE) percentage, short T_2, medium T_2 and high T_2 water fraction for the synthetic phantom.

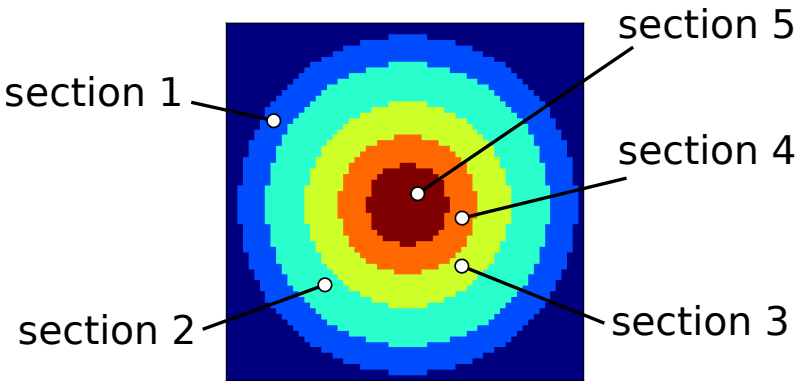

Figure 7.2: Different sections in the synthetic phantom consisting of multi-compartment T_2 relaxometry voxels with varying short, medium and high T_2 water fraction values.

The water fraction values from Section 1 to Section 3 are intended to represent normal appearing white matter (NAWM) in the brain. Section-4 has very low short T_2 water fraction value and has around 20% representation from the high T_2

	short T2	*medium T2*	*high T2*
Section 1	0.20	0.79	0.01
Section 2	0.15	0.84	0.10
Section 3	0.10	0.85	0.05
Section 4	0.05	0.75	0.20
Section 5	0.01	0.01	0.98

Table 7.1: Water fraction values for the short, medium and high T_2 compartments for the different sections of the phantom shown in Fig. 7.2.

compartment. This reduced short T_2 and some high T_2 component is intended at representing a white matter MS lesion which has undergone myelin degeneration and has presence of edema (i.e. the long T_2 component). As explained in Algorithm 1 of Appendix A, each voxel of the synthetic phantom (for Protocol A and Protocol B) is generated by randomly sampling T_2 values from the PDFs describing each compartment as per the true water fraction and FAE maps and selected protocol parameters (echo spacing and number of echoes). The analysis was performed for varying levels of signal to noise ratio (SNR): 50, 75, 100, 200, 500 and 1000. The SNR is defined with respect to the first echo and noise was added as additive Gaussian noise. Decay curves for a voxel each from various sections of the phantom for Protocol A and Protocol B are shown in Fig. A.3. The synthetic phantom images for Protocol A of the first echo for different levels of SNR are shown in Fig. 5.4.

In this experiment we perform two analyses. In the first analysis we observe the relative mean square error in estimation of water fractions and FAE for Protocol B. The results of the same analysis for Protocol A can be found in Section 5.4.1 (refer Fig. 5.8). The relative mean square error is observed for the water fractions and FAE. In the second analysis we compare the water fraction estimations for Protocol A and Protocol B. A paired t-test is performed for the water fraction estimations from Protocol A and Protocol B. The difference is considered not significant if $p > 0.05$ is observed from the paired t-test.

7.3.2 Longitudinal MS study

MS lesions are focal lesions and grow in a concentric manner [Guttmann 1995]. In the early stages, brain tissues in the MS lesions undergo active blood brain barrier breakdown [Lassmann 2001, Guttmann 1995]. Surrounding the core of the lesion is the edema as a result of tissue inflammation due to ongoing tissue damage. As compared to the normal appearing brain matter, the entire MS lesion regions appear hyper-intense on T_2 weighted MRI. However, only the regions of the lesion undergoing active blood brain barrier breakdown appear hyperintense on T_1 weighted MRI acquired post Gd injection. Hence, lesions in active state have two regions, a region which actively undergoes blood brain barrier breakdown and the regions which do not.

The objective of this experiment is to study the evolution of compartments'

water fractions in regions of lesions in MS patients undergoing active blood brain barrier breakdown and the regions which are not. In addition to that, we shall observe whether the water fraction values of the compartments for the two regions are in confirmation with the pathological knowledge of MS lesions.

In this study, we defined two groups of MS lesions, (a) $E+$: lesion regions which appear hyper-intense on post-Gd injection T_1-weighted images at the baseline and (b) $L-$: lesion regions appearing hyper-intense on T_2-weighted images only. Thus a lesion might have both $E+$ and $L-$ regions in it. An illustration of the lesion regions is shown in Fig. 7.3. The lesion ROIs are marked at baseline and the same region is observed over a period of three years. In the 10 MS patients, we observed 229 $L-$ and 25 $E+$ lesion regions. Since the lesions were marked on T_2 weighted images, all processed images were registered to the T_2 images using a block matching algorithm [Ourselin 2000, Commowick 2012].

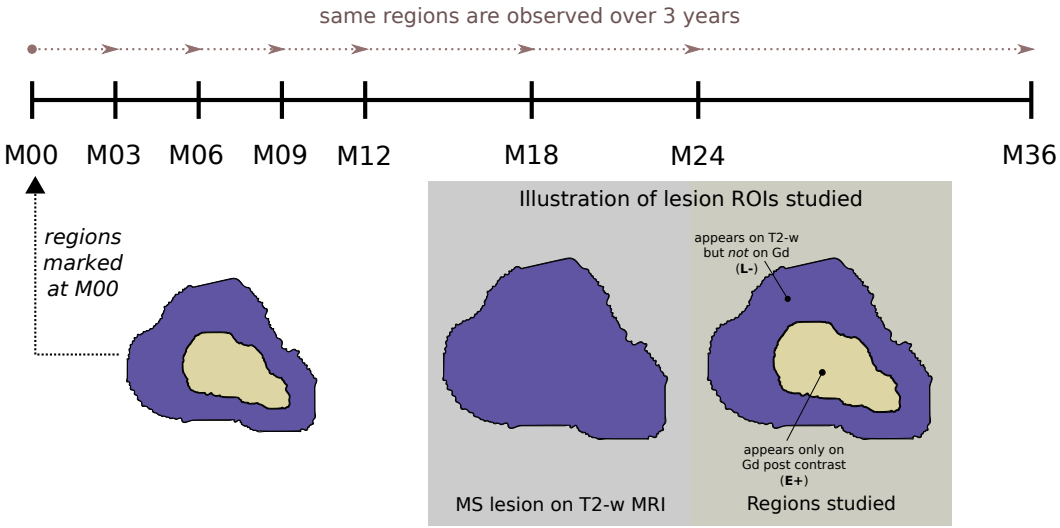

Figure 7.3: MS lesions were marked on T_2 weighted and on Gd post contrast T_1 spin echo MR images of the patients acquired at the first visit (i.e. M00). Eight scans are obtained from the first visit over a period of 36 months for each patient at intervals shown in the figure. The regions of interest (ROI) marked at M00 are studied over the period of 36 months. Two ROIs are studied: *(i)* $E+$: region of the lesion which appears on the gadolinium post contrast T_1 weighted spin echo images. These are the regions of the lesions undergoing active blood brain barrier breakdown, *(ii)* $L-$: lesion regions appearing on T_2 weighted MR images but not on gadolinium post contrast images.

7.4 Results

7.4.1 Synthetic phantom experiment

The Relative mean square error (rMSE) was used to quantify the error in estimation. The rMSE is computed as shown below:

$$rMSE = \frac{\sum_{i=1}^{N} (\hat{q}(i) - q_{true}(i))^2}{\sum_{j=1}^{N} q_{true}(j)^2} \tag{7.4}$$

where $\hat{q}$ is the estimated water fractions and q_{true} is the true value. Results for different water fractions pertaining to the two protocols are shown in Fig 7.4. The rMSE values are in the order of 10^{-2} for all the water fraction values. We also observed that the rMSE values reduce as the SNR improves. The errors in FAE estimation were observed to be in the order of 10^{-5}. The water fraction maps estimated for both protocols evaluated are shown in Fig. 7.5.

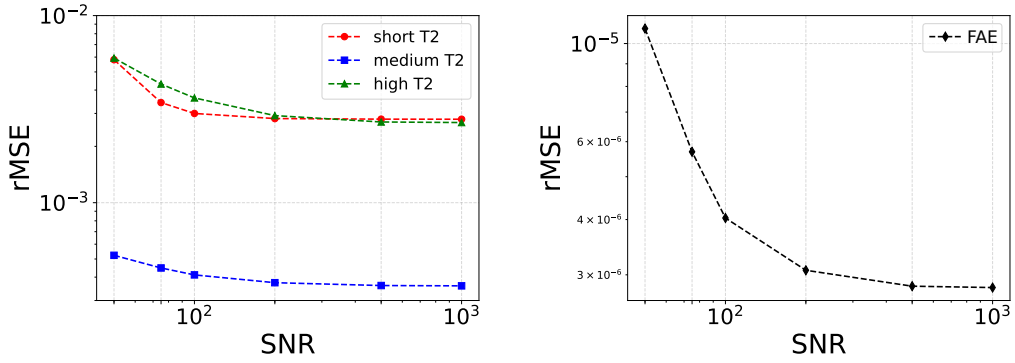

Figure 7.4: rMSE values for estimated water fraction (left) and FAE (right) are shown here. Both axes are in log scale.

The difference in the estimated water fraction maps from the synthetic phantom data with parameters of Protocol A and Protocol B are shown in Fig. 7.6. The differences are shown for each section of the phantom for more clarity. For each section the zero level is very close to the median of the differences in the estimations for all water fractions. The existence of any significant difference between the estimations from Protocol A and Protocol B are further evaluated using a paired t-test. Significant differences ($p < 0.1$) are observed between the estimated water fraction maps from Protocol A and Protocol B for SNR level of 50: short T_2: p-value=0.035, medium T_2: p-value=0.002 and high T_2: p-value=0.085. No significant difference ($p > 0.05$) was observed for any other water fraction estimated (for all SNR levels).

Relative absolute difference percentage (rAD) was computed to observe the change in estimation when using Protocol B relative to Protocol A. The rAD for

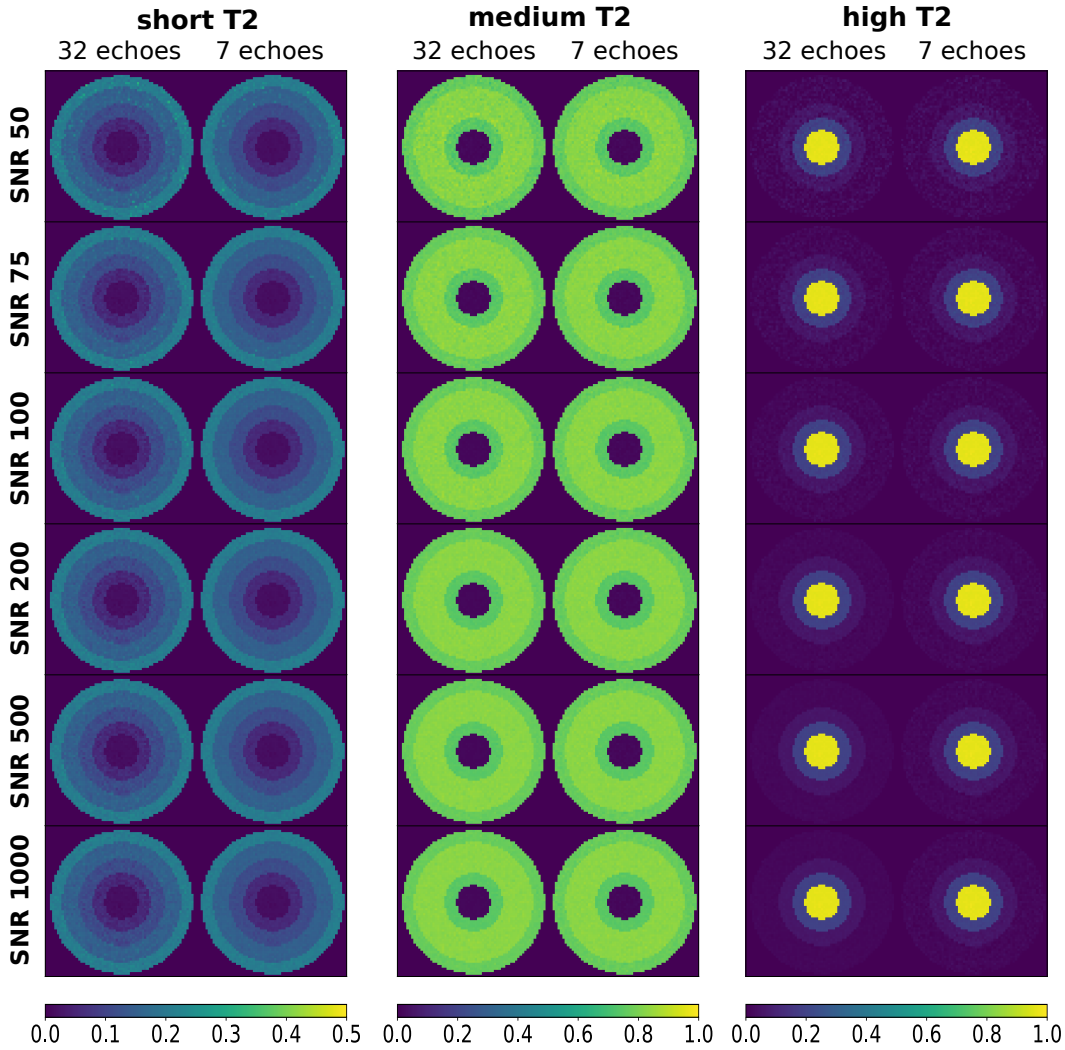

Figure 7.5: The estimated water fraction maps for Protocol A (32 echoes) and Protocol B (7 echoes) are shown here for various levels of SNR.

the $i-$th voxel was computed as shown below:

$$rAD\,(i) = \left| \frac{\hat{q}_A(i) - \hat{q}_B(i)}{\hat{q}_A(i)} \right| \times 100 \tag{7.5}$$

where $\hat{q}_A$ and $\hat{q}_B$ are estimations using data from Protocol A and Protocol B respectively. The rAD and mean of the relative absolute difference values are shown in Fig. 7.7. The calculations are shown for Section 1 to 4 for short T_2 and medium T_2 water fractions, and Section 4 to 5 for the high T_2 water fraction. The left out sections for the respective water fractions had negligible values in the corresponding sections of the synthetic phantom (for example short T_2 and medium T_2 had only 0.01 value in free fluids section i.e. section 5). The images used for clinical study has SNR in the range of 75 to 100 (from ROI based measurements [Henkelman 1985]).

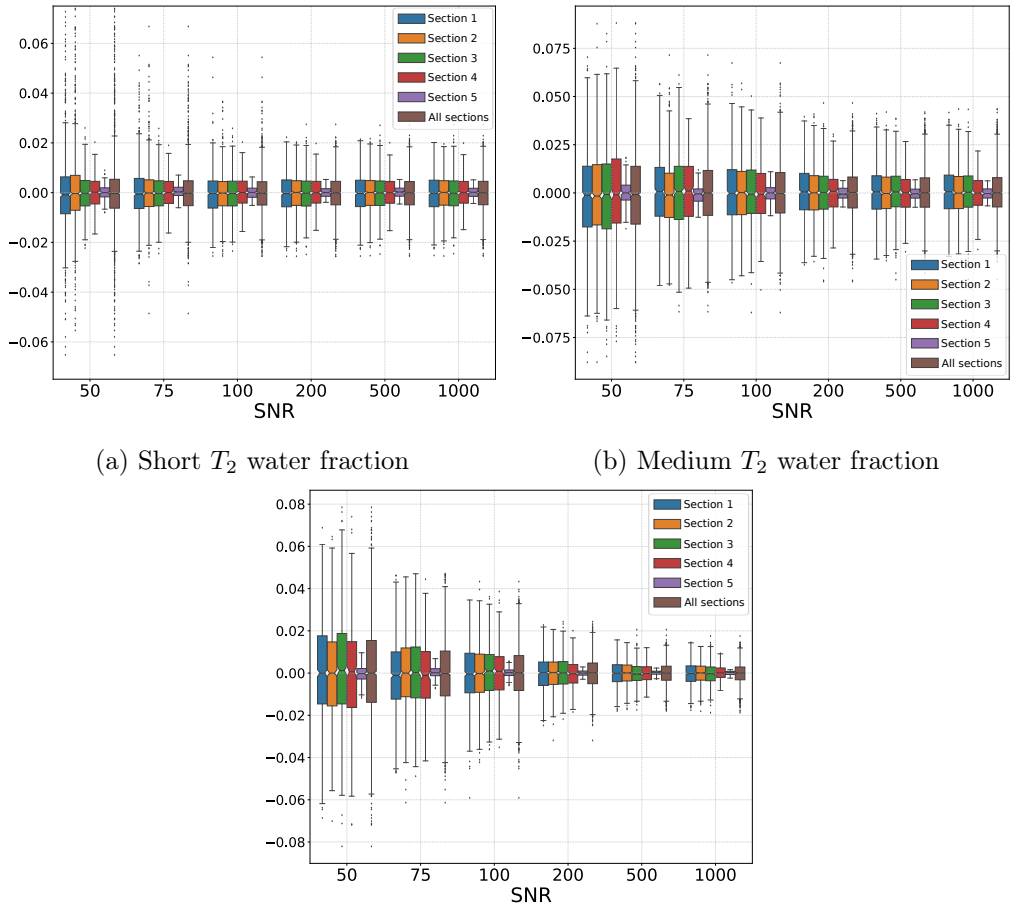

(a) Short T_2 water fraction

(b) Medium T_2 water fraction

(c) High T_2 water fraction

Figure 7.6: The difference between estimated short T_2, medium T_2 and high T_2 water fraction maps from Protocol A and Protocol B are shown here. Along with the whole phantom, section-wise differences are also shown to provide a greater understanding. The section label numbers can be referred from Fig. 7.2.

The short T_2 water fraction values vary by around 5% for those SNR levels for Section 1 to 3. For the same sections and SNR value, variations for medium T_2 water fraction is less than 2%. Section 4 has water fraction values similar to what we may expect in MS lesions. The short T_2 water fraction has a low value of 0.05 and high T_2 water fraction has a value of 0.20. At SNR of 75 and 100, we observed a mean relative absolute difference of around 9%, 2% and 6% for short T_2, medium T_2 and high T_2 water fraction values respectively.

7.4.2 Application to Multiple Sclerosis (MS)

In this experiment we observed and compared the evolution of water fraction maps of the three compartments between $E+$ and $L-$ MS lesion regions in 10 patients

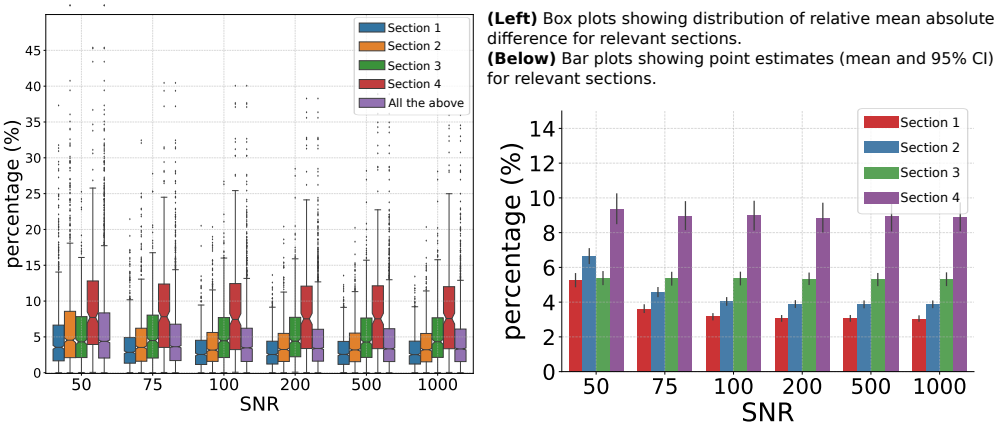

(a) Short T_2 water fraction

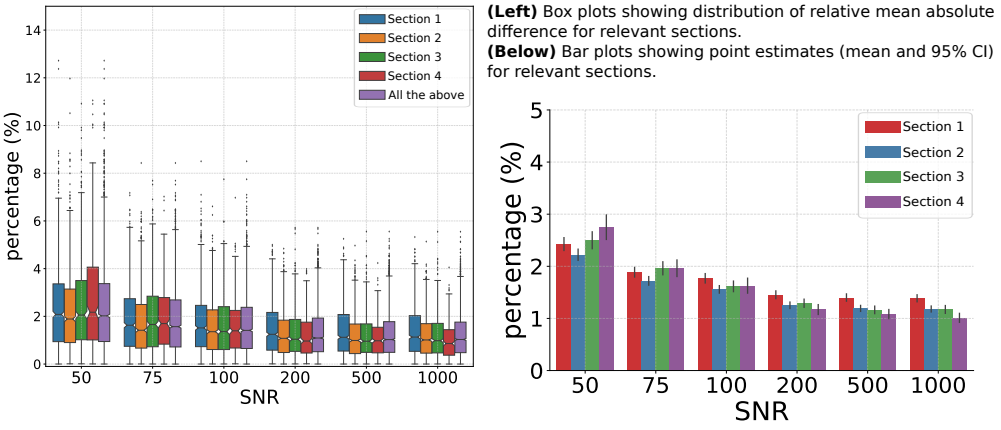

(b) Medium T_2 water fraction

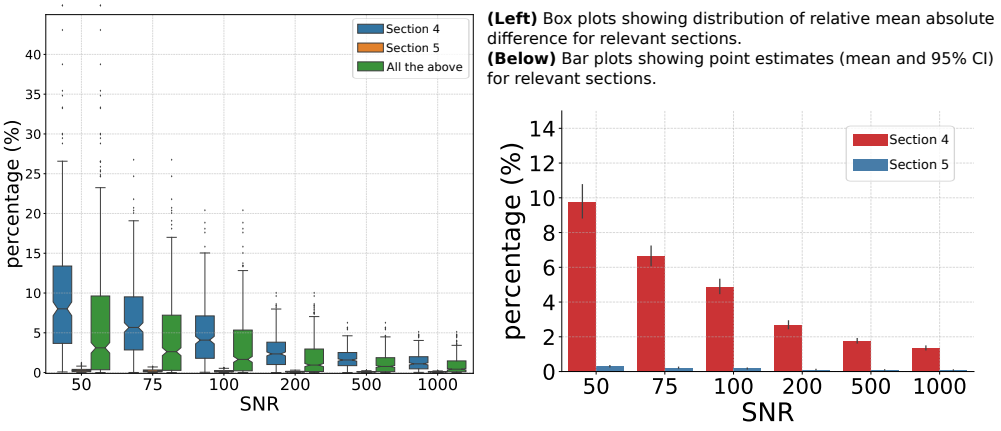

(c) High T_2 water fraction

Figure 7.7: The relative mean absolute difference (in percentage) between estimated short T_2, medium T_2 and high T_2 water fraction maps from Protocol A and Protocol B for relevant sections of the synthetic phantom are shown here. The section label numbers can be referred from Fig. 7.2.

over a period of 3 years. We observed the water fraction values for $E+$ and $L-$ at each scan point. In addition to it, we also observed the change in the water fraction values (for $E+$ and $L-$) between consecutive scans which is computed as: $\Delta w_{f,i} = \left(w_{f_{scan_{i+1}}} - w_{f_{scan_i}}\right)$. Hence positive values indicate a gain in the water fraction values between consecutive scans. The $E+$ and $L-$ group difference analysis was performed using Mann-Whitney U test.

An example illustrating the comparison between the water fraction maps for a healthy control and MS patient is shown in Fig. 7.8. Lesion-1 in the MS patient has a large active core, whereas a very small region of lesion-2 is active. Both lesions show indications of extensive demyelination. The medium T_2 and high T_2 water fraction maps show varying trends among the lesions, and also between the regions of the lesion undergoing active blood brain barrier breakdown and otherwise.

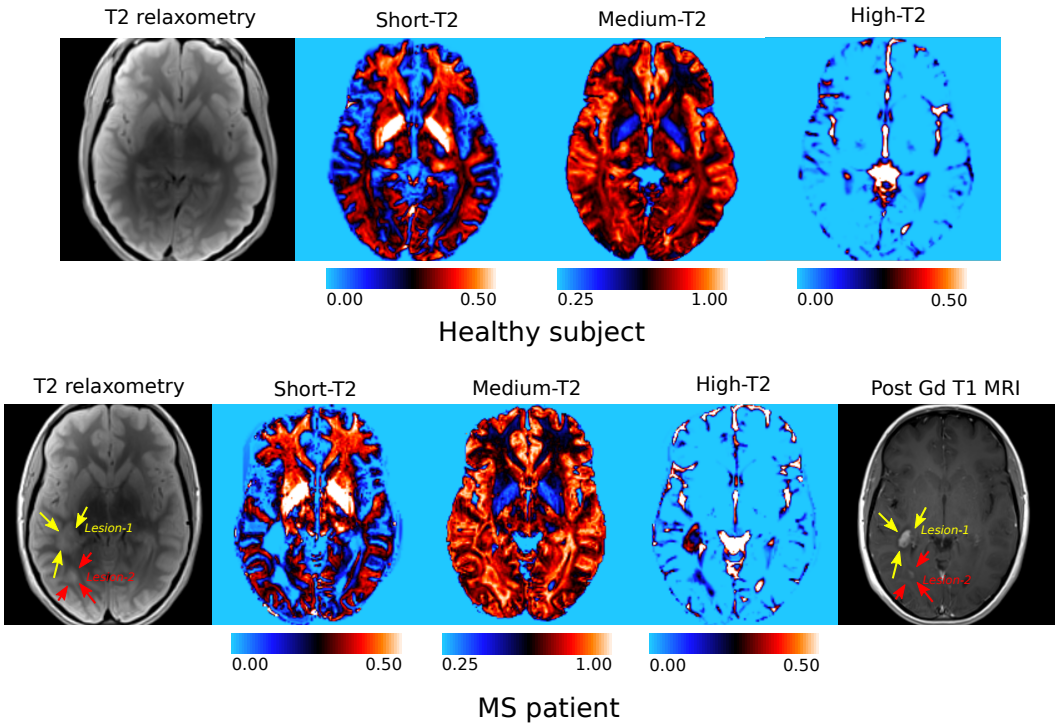

Figure 7.8: A comparison between water fraction maps for (top) healthy subject and (bottom) MS patient with lesions is shown here. Lesion-1 (yellow arrows) has a large active core compared to lesion-2 (red arrows). The difference in water fraction maps can be observed between the enhancing and non-enhancing lesion regions.

Short T_2 water fraction Results for short T_2 water fraction (w_s) maps are shown in Fig. 7.9. The w_s values of the $E+$ and $L-$ lesions at all time points are shown in Fig. 7.9a. The $L-$ lesion regions are significantly associated with higher w_s values as compared to $E+$ at M00 ($p = 0.014$). However, the w_s distributions of $E+$ and $L-$

regions at the end of 3 years are similar. The changes in w_s values (Δw_s) between consecutive scans in shown in Fig. 7.9b. Largely positive $\Delta w_{s,0}$ values for $E+$ lesion regions suggest increased w_s values between M00 and M03. After M06 we observed less changes in w_s values in $E+$ lesion regions. The observed change in w_s values for the $L-$ lesions regions was very less throughout the 3 year period. Only $\Delta w_{s,0}$ values $E+$ and $L-$ were significantly different ($p = 0.009$).

Medium T_2 water fraction The results are shown in Fig. 7.10. The evolution of the medium T_2 water fraction (w_m) in $E+$ and $L-$ lesion regions is shown in Fig. 7.10a. Although the w_m values for both groups reduce slightly at the end of 3 years, there is no evidence of difference between $E+$ and $L-$ with respect to the change in w_m values between successive scans (refer Fig. 7.10b).

High T_2 water fraction The high T_2 water fraction (w_h) values for $E+$ and $L-$ lesion regions are shown in Fig. 7.11a. The $E+$ lesion regions are significantly associated with a higher value of w_h as compared to the $L-$ population at M00 ($p = 0.002$). Largely negative $\Delta w_{h,0}$ values (refer Fig. 7.11b) for $E+$ lesion regions suggest a decrease in their w_h values between M00 and M03. Subsequently, $E+$ lesion regions undergo negligible change between consecutive scans. $L-$ lesion regions show negligible change in their w_h values throughout the period of the study. The change in w_h values were found to be significantly different between $E+$ and $L-$ lesion regions for scan periods M00-M03, M03-M06 and M06-M09 with p-values of 0.008, 0.011 and 0.011 respectively.

It is also important to observe the effect size of the datasets when observing the p-values for group differences. Whereas the p-value conveys information on the strength of the water fraction values to reject the null hypothesis, the effect size is a measure of the magnitude of the difference. We used the common language (CL) effect size statistic and the associated p-values to observe the group differences [McGraw 1992, Grissom 2005]. The CL effect size for the groups that were found to be significantly different from the Mann-Whitney U test is shown in Table 7.2. In this work, the CL effect size value denotes the percentage of times the w_f value of $L-$ is higher than $E+$ when both samples are selected at random from each group. It can hence be interpreted as the probability of superiority of $L-$ over $E+$ for a measurement.

The evolution of water fraction maps for a lesion in a MS patient has been shown in Fig. 7.12. The water fraction maps show indication of remyelination and reduction of edema in the lesion region observed at baseline scan over a period of 3 years.

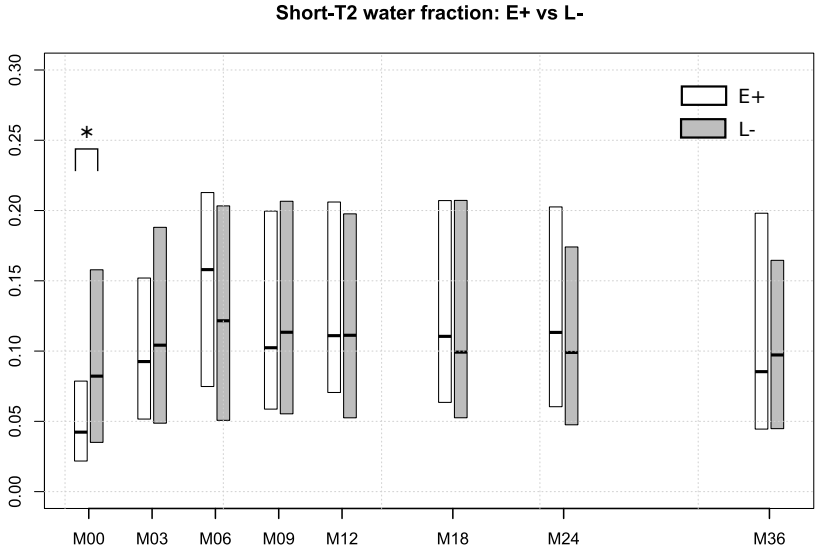

(a) Values at each acquisition point

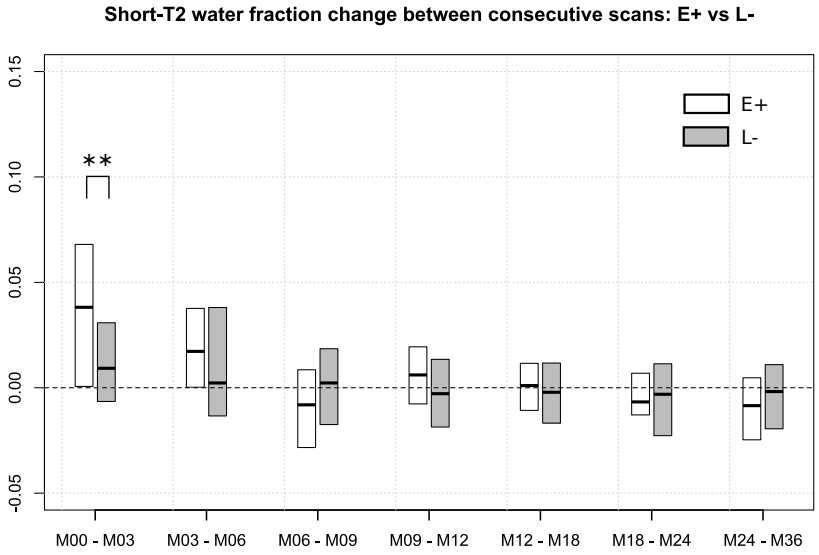

(b) Change in values between consecutive acquisitions

Figure 7.9: *Evolution of short T_2 water fraction values over 3 years*: The plots in this figure show the median and upper and lower quartile levels of the data. (a) The short-T_2 water fraction value (w_s) at each scan. (b) The change in w_s between consecutive scans is shown in Fig. 7.9b. Significant differences between groups are shown using * ($p < 0.05$) and ** ($p < 0.01$).

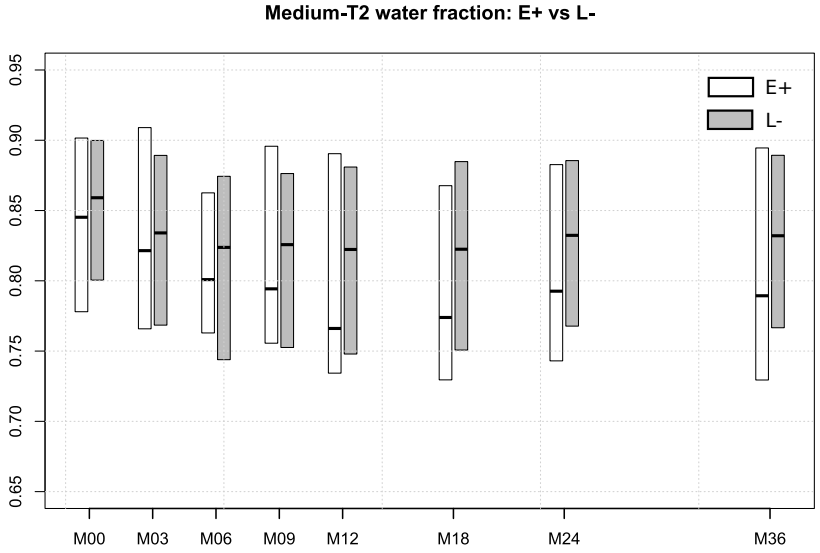

(a) Values at each acquisition point

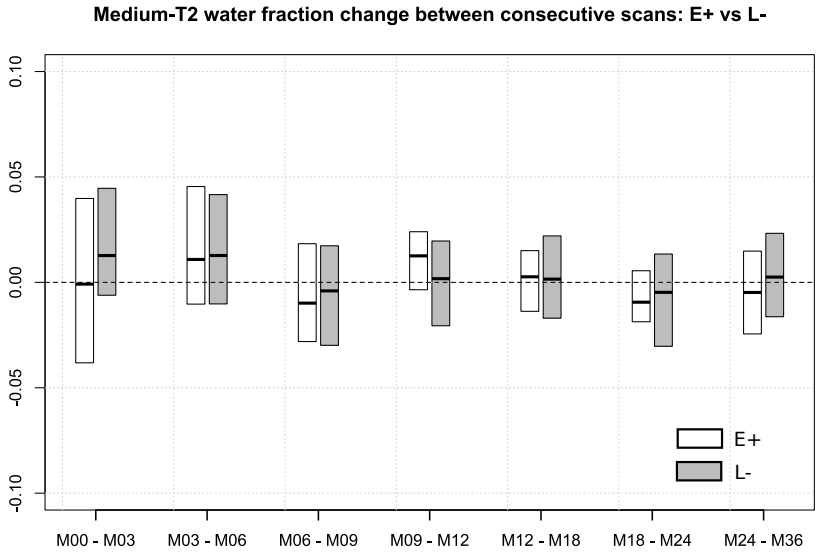

(b) Change in values between consecutive acquisitions

Figure 7.10: *Evolution of medium T_2 water fraction values over 3 years*: The plots in this figure show the median and upper and lower quartile levels of the data. (a) The medium T_2 water fraction value (w_m) at each scan. (b) The change in w_m between consecutive scans. Significant differences between groups are shown using * ($p < 0.05$) and ** ($p < 0.01$).

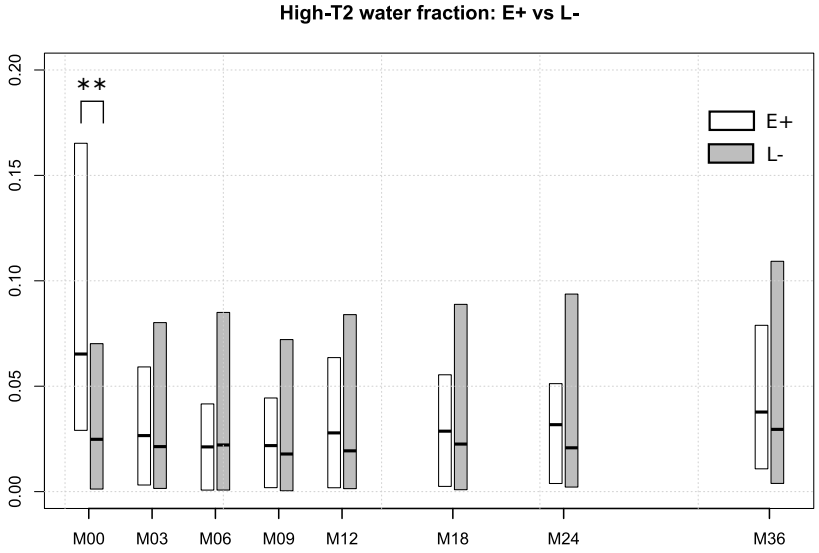

(a) Values at each acquisition point

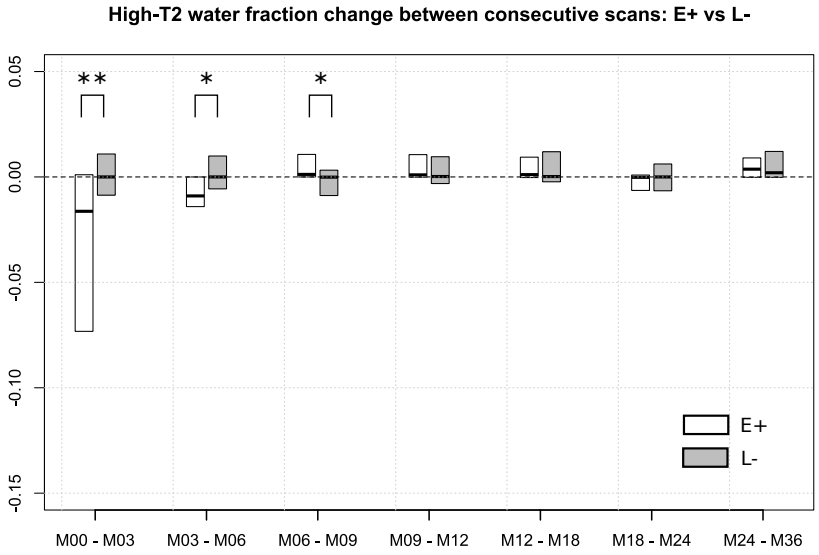

(b) Change in values between consecutive acquisitions

Figure 7.11: *Evolution of high T_2 water fraction values over 3 years* The plots in this figure show the median and upper and lower quartile levels of the data. (a) The high T_2 water fraction value (w_h) at each scan. (b) The change in w_h between consecutive scans. Significant differences between groups are shown using * ($p < 0.05$) and ** ($p < 0.01$).

Value	*p-value*	*CL effect size*
Short-T_2 water fraction (w_s) at M00	0.014	65.05%
Δw_s between M00 and M03	0.009	34.25%
High-T_2 water fraction (w_h) at M00	0.002	31.51%
Δw_h between M00 and M03	0.008	66.08%
Δw_h between M03 and M06	0.011	65.51%
Δw_h between M06 and M09	0.011	34.55%

Table 7.2: The common language (CL) effect size are reported for the measurements which were significantly different for $E+$ and $L-$.

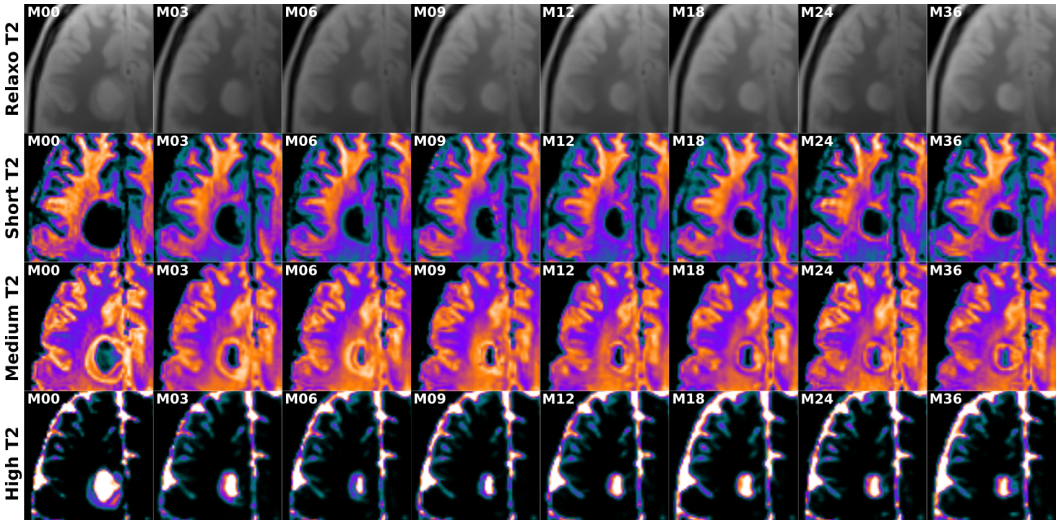

Figure 7.12: An evolution of the water fraction a maps and corresponding T_2 weighted images are shown for a lesion of a MS case used in this study. It can be observed that the T_2 lesion shrinks after the initial scan. The short T_2 water fraction maps indicates signs of remyelination and the high T_2 water fraction map indicates reduction in the edema.

7.5 Discussion

In this work, we used the parametric multi-compartment T_2 relaxometry method proposed in Chapter 5 for studying change in water fraction values in MS lesions. In that analysis we had investigated the repeatability of the method using test-retest experiments on healthy controls (discussed in Sections 5.3.4 and 5.4.4). The results of the repeatability experiments showed that this method can be used for longitudinal studies where the estimations across time points can be compared.

In this study we used MS patient data acquired in under 8 minutes. The number of echoes acquired and the echo spacing were coarser (compared to test=retest experiment data) to obtain the T_2 relaxometry data in a shorter time than usual

(> 20 minutes). However, the test-retest data could not be acquired with this protocol as the clinical study was performed on a retrospective dataset. To address this, we designed a synthetic phantom experiment where images with same ground truth were generated with the protocol on which the repeatability experiments were performed in Chapter 5 and the protocol used for the MS study discussed in this chapter. The synthetic phantom had multiple sections representing normal appearing white matter and sections emulating water fractions usually present in lesions and free water (as CSF). In addition to having sections with varying water fraction values, the phantom had four sections with different FAE values. Experiments were performed for very low to high SNR values. The operating SNR for the images used in this study was in the range of 75-100. The SNR was computed for various white matter regions (of the first echo of T_2 relaxometry image) using the ROI based methods and suitable corrections were made for non-Gaussian nature of the background noise [Henkelman 1985].

The water fraction values estimated for synthetic phantom using MS study and test-retest experiment protocol parameters were compared. The normal appearing white matter regions showed around 5% and less than 2% relative difference in estimations of the short T_2 and medium T_2 water fraction values while using the protocol used for the MS study compared to the protocol used for the repeatability study in Chapter 5. The lesion like section showed a relative difference of around 9% and less than 2% and approximately 5% for the short T_2, medium T_2 and high T_2 water fraction estimates. A paired t-test showed no significant differences (p-value>0.05) between the water fraction estimates for all compartments for the operating SNR range. Even at very low water fraction values, the method proposed in Chapter 5 performs close enough for the clinical (acquisition time <7 minutes) and a high quality T_2 relaxometry data (acquisition time >20 minutes). The comprehensive synthetic phantom experiment enables us to apply the method on the protocol used in the retrospective MS study.

In Section 7.4.2 the evolution of water fraction markers in MS lesion regions which are undergoing active blood brain barrier breakdown are compared to the MS lesion regions in the later stages. At the baseline scan, the $E+$ lesion regions are prone to having lower short T_2 water fraction values as compared to $L-$ regions ($p = 0.014$, CL = 65.05%). This might indicate that regions of the lesion undergoing active blood brain barrier breakdown have undergone greater demyelination. However, there seems to be no significant difference between the two groups with respect to the short T_2 water fraction values for all scans three months after the baseline. The $E+$ lesion regions tend to have significantly higher values for high T_2 water fraction as compared to $L-$ at the baseline scan ($p < 0.01$, CL = 31.51%). The demyelination of MS lesions is accompanied by inflammation due to increased macrophage intervention [Lassmann 2001]. This might explain the low and high values of short T_2 and high T_2 water fraction values observed at the baseline scan for $E+$ lesion regions. The gain in short-T_2 water fraction values for $E+$ lesion regions between the scans at M00 and M03 is significantly greater than that for $L-$ ($p < 0.01$, CL = 34.25%). The increase in short-T_2 values in this period is accompa-

nied by a considerable drop in high-T_2 values for the $E+$ lesion regions. The drop in high-T_2 water fraction values between the baseline and the next scan for $E+$ is significantly larger than that of $L-$ ($p < 0.01$, CL = 66.08%). All $E+$ lesion regions incur a decrease in high T_2 values over the first six months of observation.

Hence, the observations from the change in water fraction values between consecutive scans are: *(i)* although both groups show indications of remyelination, $E+$ lesion regions undergo significantly greater remyelination as compared to $L-$ between the baseline and scan at M03, *(ii)* there is a considerable reduction of inflammation in $E+$ over the first three months but $L-$ show little or no change in this aspect. The myelination activity of $E+$ and $L-$ is similar three months after baseline. However, the inflammation activity seems to continue for 9 months from baseline scan time. Some $L-$ lesion regions observed at the baseline scan would have been in the $E+$ stage at some point of time. This explains the similar water fraction values for $E+$ and $L-$ by the end of three years. Unlike short T_2 and high T_2 water fraction values, the medium T_2 water fraction values for $E+$ and $L-$ lesion regions never show any significant difference, which might be attributed to the fact that in terms of T_2 values considered, the medium T_2 water pool is highly heterogeneous. It conveys information on unmyelinated axons, glia, interstitial and extra-cellular matters [Lancaster 2003].

Our study on MS patients has certain limitations. First, the clinical data available was not of the highest quality possible due to acquisition time constraints in a clinical setting. T_2 relaxometry data with a higher number of echoes and shorter echo times are favorable for multi-compartment models. To address this concern we performed a comprehensive synthetic phantom experiment where the estimation results were compared for a data acquired with the MS study protocol used in for this study and a standard multi-echo T_2 relaxometry sequence. The results showed that for the operating SNR (of the clinical data), the water fraction maps are not significantly different (based on paired t-test with a significance threshold of $p - value$=0.1). Second, the time gap between the first and second scan was three months. A shorter interval between successive acquisitions would be beneficial to study the fast evolving active lesions.

7.6 Conclusion

In this chapter we proposed to use the multi-compartment T_2 relaxometry model proposed in chapter 5 to study evolution of obtained biomarkers from the model in enhancing and non-enhancing regions of the MS lesions. The study of the evolution of multi-compartment T_2 relaxometry markers on 10 MS patients over a period of 3 years had two important observations: *(i)* the markers have the potential to distinguish between gadolinium enhanced and non-enhanced regions in MS lesions and *(ii)* both lesion regions have similar water fraction values by the end of the third year and show little distinction after 3 months from baseline scan. The observations from the longitudinal study shows that the biomarkers obtained from this model explains

the MS lesion evolution along the lines reported in the pathological and radiological studies on MS lesions [Lassmann 2001, Guttmann 1995]. The former observation on the other hand motivates us to investigate methods by which biomarkers from multi-compartment models based on advanced MRI techniques can help distinguish between lesion regions undergoing active blood brain barrier breakdown without injection of contrast enhancers in MS patients, which we shall investigate in the next chapter.

Chapter 8

Identification of gadolinium contrast enhanced regions in MS lesions using diffusion and T_2 relaxometry MRI

Contents

8.1 Introduction

Multiple sclerosis (MS) patients have multiple focal lesions in the brain. In the early stages, the MS lesions undergo active blood brain barrier (BBB) breakdown [Guttmann 1995, Lassmann 2001]. Lesions in this stage are referred to as enhancing lesions and the clinical significance of its identification is well established. Gadolinium based contrast agents (GBCA) are popularly used by radiologists to identify enhancing MS lesions. A T1-weighted MRI acquired post GBCA injection is a part of the recommended MRI protocols for diagnosis and follow-up examinations of MS patients [Brownlee 2017]. However, the use of GBCAs has been

a recent topic of debate, primarily due to reports of Gd deposition in the brain [Kanda 2013, Olchowy 2017]. Suggestions insisting on greater debate before GBCA administration has gained traction due to observed MRI signal changes in the brain tissues due to repeated GBCA administrations and other possible health issues [Gulani 2017]. A MS lesions in its enhancing stage has different pathological traits as compared to late or non-enhancing MS lesions [Lassmann 2001]. Regions of lesion undergoing active BBB breakdown has a higher water content owing to the undergoing tissue damages such as functional impairment of the morphologically intact endothelial cells [Guttmann 1995]. Hence by the virtue of the brain tissue microstructure characteristics of MS lesions, we may identify enhancing regions in the lesion (if any). Although MRI effectively provides in-vivo images of the brain, it is constrained by the limited imaging resolution it can provide. This limitation is primarily attributed to hardware limits and the need for adhering to reasonable scan times for clinical implementations. However, advanced MRI methods, such as diffusion MRI (dMRI) and T2 relaxometry help us obtain estimates on condition of brain tissue microstructure. The multi-compartment models (MCM) [Panagiotaki 2012] in dMRI provide information on the organization of the nerve fibers in the brain. MS lesions disrupt the normal organization of fibers in the brain. The extent of this damage may be assessed from the tissue microstrucutre estimates derived from dMRI MCMs. Myelin is also a critical biomarker in neurodegenerative diseases such as MS [Lassmann 2001, Laule 2007a, MacKay 2016]. Demyelination marks the onset of MS [Lassmann 2001]. Myelin has a very short T2 relaxation time (<50ms) due to its tightly wrapped structure [Lancaster 2003]. Due to higher TEs in dMRI, the myelin information is not present in the dMRI signals. However, myelin information can be obtained by estimating the myelin water fraction (MWF) from T2 relaxometry MRI signal [Laule 2007a, MacKay 2016]. The inflammation in MS lesions can be assessed from T2 relaxometry and dMRI signal. Hence, by combining the tissue microstructure information from these two MRI methods, we can obtain considerable information on brain tissue health. In this work we combine the microstructure information obtained from T2 relaxometry and dMRI to identify Gd enhanced regions in MS lesions.We performed experiments to evaluate whether combining the tissue microstructures is advantageous as compared to using them alone. The observations from this experiment is carried forward to the next stage where we perform enhancing lesion region predictions in a MS patient.

8.2 Material and methods

8.2.1 Multi-compartment T_2 relaxometry model (MCT2)

Three T2 relaxometry compartments are considered in a voxel based on their T2 relaxations times and are referred to as short-, medium- and high-T2. The short-T2 compartment conveys information on brain tissues with T2 relaxation times shorter than 50ms. These tissues primarily include myelin and highly myelinated axons [Lancaster 2003]. The high-T2 compartment represents the tissues with T2

values greater than 1000ms, comprising primarily of free fluids (CSF in healthy volunteer) and water accumulated in tissues due to pathology (edema regions in MS lesions). The medium-T2 compartment is a mixed pool and conveys information on intracellular matter (such as unmyelinated axons and glia), intra and extracellular fluids [Lancaster 2003]. The T2 space is modeled as a weighted mixture of the three compartments, where each compartment is represented by a continuous probability density function (PDF). The signal of a voxel at the i-th echo in the MCT2 is modeled as:

$$s\left(t_i\right) = \sum_{j=1}^{3} \alpha_j \int_0^{\infty} f_j\left(T_2; \mathbf{p_j}\right) EPG\left(T_2, \triangle TE, i, B_1\right) dT_2 \tag{8.1}$$

In Eq. (8.1), $f_j\left(T_2; \mathbf{p}\right)$ is the chosen PDF to represent the j-th compartment with parameters $\mathbf{p_j} = \{p_{j_1}, p_{j_2}, \ldots\}$. We used the 2D multislice Carr-Purcell-Meiboom-Gill (CPMG) sequence to acquire T2 relaxometry data. CPMG sequences suffer from the effect of the stimulated echoes due to imperfect refocusing. It is important to address this effect as this leads to errors in T2 estimation [Crawley 1987]. Here we tackle is the problem of stimulated echoes using the iterative technique of Extended Phase Graph (EPG) algorithm [Prasloski 2012]. Each compartment's weight is obtained as, $w_j = \alpha_j / \sum_i \alpha_i$. Simultaneous estimation of the weights and parameters of the distributions of such multi-compartment models is non-trivial and not reliable in terms of robustness and accuracy [Layton 2013]. Hence we choose to fix the PDF parameters. In this work, the $\{f_j(\cdot)\}_{j=1}^{3}$ are chosen as Gaussian PDFs. Their mean and standard deviation are fixed based on the findings from the literature [Laule 2007a, MacKay 2016, Lancaster 2003] and are set as $\mu = \{20, 100, 2000\}$ and $\sigma = \{5, 10, 80\}$ (all values in milliseconds). Estimating the model thus resorts to finding the optimal $\{\alpha_j\}_{j=1}^{3}$ and B_1 for the following least squares problem:

$$\left(\hat{\alpha}, \hat{B_1}\right) = \arg\min_{\alpha, B_1} \sum_{i=1}^{m} \left(y_i - \sum_{j=1}^{3} \alpha_j \lambda_j\left(t_i; B_1\right) \right)^2 \tag{8.2}$$

where $\mathbf{Y} \in \mathbb{R}^m$ is the observed signal; m is the number of echoes; $\alpha \in \mathbb{R}^{+3}$. Although the optimization of α and B_1 are linear and non-linear in nature, these variables are linearly separable. α and B_1 are computed by non-negative least squares and BOBYQA optimization respectively. The weights of short-T2 (w_s), medium-T2 (w_m) and high-T2 (w_h) compartment for every voxel are used as a feature for each voxel.

8.2.2 Multi-compartment Diffusion model (MCDiff)

For diffusion MRI (dMRI), we considered the recently introduced MCM as they provide an intuitive way of describing the different fascicles, cells and free water contributions to each voxel. MCM are defined as a weighted sum of several compartments each describing a fascicle (i.e. a dense set of fibers sharing the same orientation) or

isotropic matter (such as free water or water trapped in cell bodies). Similar to T2 relaxometry, each compartment in MCDiff is defined by a PDF. However in MCDiff, the PDFs describe water diffusion probability inside the compartments. A variety of compartment types may be defined [Panagiotaki 2012] based on the assumed white matter microstructure and the acquired dMRI data (the more gradient directions and b-values, the more information may be extracted). Our proposed method is quite independent of this choice and can be applied generically to all parameters that may be extracted from MCM. In the specific study in Section 8.4, we have focused on the following model:

$$p(x) = f_w p_{FW}(x) + \sum_{i=1}^{N=3} a_i p_i(x) \tag{8.3}$$

where $f_w + \sum_i a_i = 1$ are the weights of the individual compartments, p_{FW} is an isotropic Gaussian PDF specific to free water (i.e. with a variance of 3.0×10^{-3} $mm^2.s^{-1}$), $p_i(x)$ denotes the i-th fascicle compartment PDF here defined as a stick model (i.e. a Gaussian PDF with equal secondary eigenvalues, fixed from an outside reference). We have specifically chosen this ball and stick model for our experiments as it can be estimated reliably on our clinical data (see Section 8.2.3). This estimation was performed using the method proposed by Stamm et al. [Stamm 2016], which uses a variable projection on the linear elements of the cost function (the compartment weights) to perform a fast maximum likelihood estimation of the model parameters with Levenberg-Marquardt optimization. We then defined different parameters from this MCM which describe the white matter microstructure inside the voxel. First, each anisotropic compartment p_i is defined as a constrained tensor. Hence we can extract the usual tensor scalar maps for each anisotropic compartment. However, to enable comparison between voxels, we need to average those compartment specific values over all anisotropic compartments. We have thus computed the weighted average of those values (using the weights a_i) to get the following scalar maps: fractional anisotropy (FA_{mc}), apparent diffusion coefficient (ADC_{mc}) and axial diffusivity (AD_{mc}). In addition to those maps, the weight of isotropic free water (f_w) is a crucial one that could identify edema or other free water related phenomena and we therefore included it in the parameters as well.

8.2.3 Data

All acquisitions were made on a 3T MRI scanner. The T2 relaxometry data was obtained using a 2D multislice CPMG sequence with the following specifications: first echo time (TE) = 13.8ms; echo spacing = 13.8ms; 7 echoes; repetition time (TR) = 4530ms; $1.33 \times 1.33 \times 3mm^3$ voxel resolution; acquisition time was just less than 7min. The dMRI acquisition was performed with 30 directions on a single shell of b-value at $1000s/mm^2$, with a $2 \times 2 \times 2mm^3$ voxel resolution, on a $128 \times 128 \times 60$ matrix with TE and TR of 94ms and 9.3s respectively. Transverse SE T1-w images ($1 \times 1 \times 3mm^3$) post Gd contrast agent infusion (0.1mmol/kg gadopentetate dimeglumine) were acquired to find Gd enhanced lesions. A T1-w image was also acquired

for performing the distortion correction in diffusion images. A 3D MPRAGE image was acquired with inversion time, TR and TE of 900ms, 1900ms and 2.98ms respectively. The voxel resolution was $1 \times 1 \times 1mm^3$ on a $256 \times 256 \times 160$ matrix. Lesions were segmented on T2-w images by radiologist. Hence all images were registered to the T2 image ($1 \times 1 \times 3mm^3$ voxel resolution) linear registration using a block-matching algorithm [Commowick 2012, Ourselin 2000]. Our data set consisted of 10 MS patient datasets demonstrating clinically isolated syndrome (CIS) condition. There were a total of 227 MS lesions in all patients, out of which 28 lesions had gadolinium enhancing regions. The voxels are divided into two groups: *(a)* (E+): voxels appearing on Gd enhanced T1 SE images and *(b)* (L-): lesion voxels which are hyperintense on T2-w images but do not appear on Gd enhanced T1-weighted images. The protocols were approved by the institutional review board, and all participants gave their written consent.

8.2.4 Identifying enhancing voxels in lesions

We performed enhancing voxel identification using the MCT2 and MCDiff estimates. In our database, we had 15012 and 3904 (L-) and (E+) voxels respectively. We adopted a random shuffle and repeat strategy to compensate for the imbalance in the class. 5000 (L-) and 3400 (E+) voxels are randomly selected from the dataset to train the classifier. The remaining (L-) and (E+) voxels are then used to evaluate the classifier performance. This method is repeated 100 times to avoid any bias in sampling the data set for model training. The accuracy statistics are recorded for every repetition. It shall be noted that the model from one repetition is not retained for the next. For a new repetition, the model is trained and validated on a different dataset. We then observe the validation error of the classifier over 100 repetitions. We used support vector machine classifier (with radial basis function

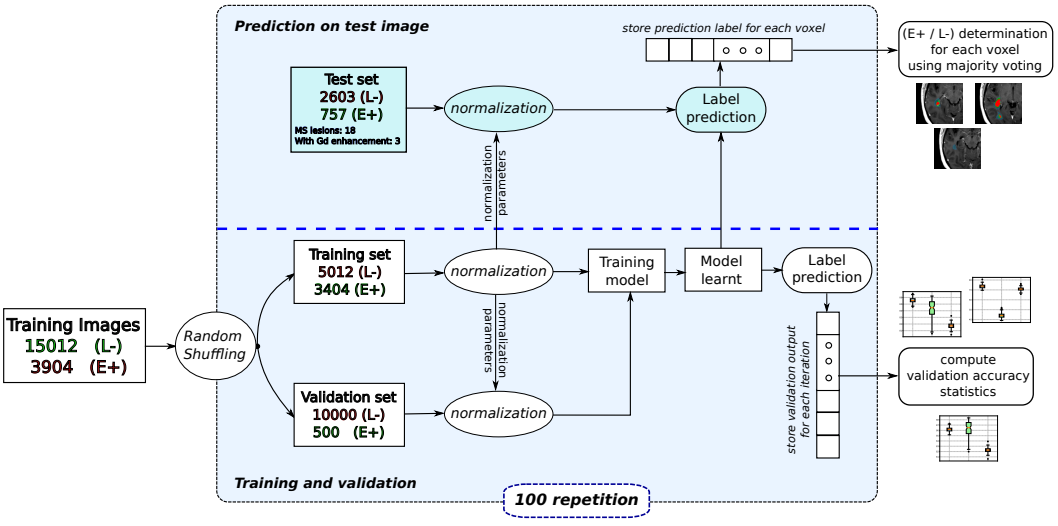

Figure 8.1: The method used to predict the enhancing voxels is illustrated here.

kernel) in this work [Cortes 1995]. The method for predicting enhancing voxels has been illustrated in Fig. 8.1.

8.3 Experiments

8.3.1 Experiment 1: Feature evaluation

The predictions are performed using three features sets: **(a)** MCT2 derived microstructure information: $\mathcal{F}_R = \{w_s,\ w_m,\ w_h,\} \in \mathbb{R}^3$, **(b)** MDiff derived microstructure information: $\mathcal{F}_D = \{f_w\ ,\ FA_{mc},\ ADC_{mc},\ AD_{mc}\} \in \mathbb{R}^4$ and **(c)** a features set containing both MCT2 and MCDiff derived microstructure information $\left(\mathcal{F}_{RD} \in \mathbb{R}^7\right)$. The aim of this experiment is to observe whether combining the diffusion and T2 relaxometry derived microstructure increases the accuracy of prediction. The observations from this experiment will help us comment on complimentary nature of the feature sets (if any). The MCT2 and MCDiff estimation maps are shown for a lesion of a MS patient in Fig. 8.2. The region of the lesion undergoing active blood brain barrier breakdown can be distinguished from the other regions of the lesions from visual inspection of the estimated MCT2 and MCDiff maps.

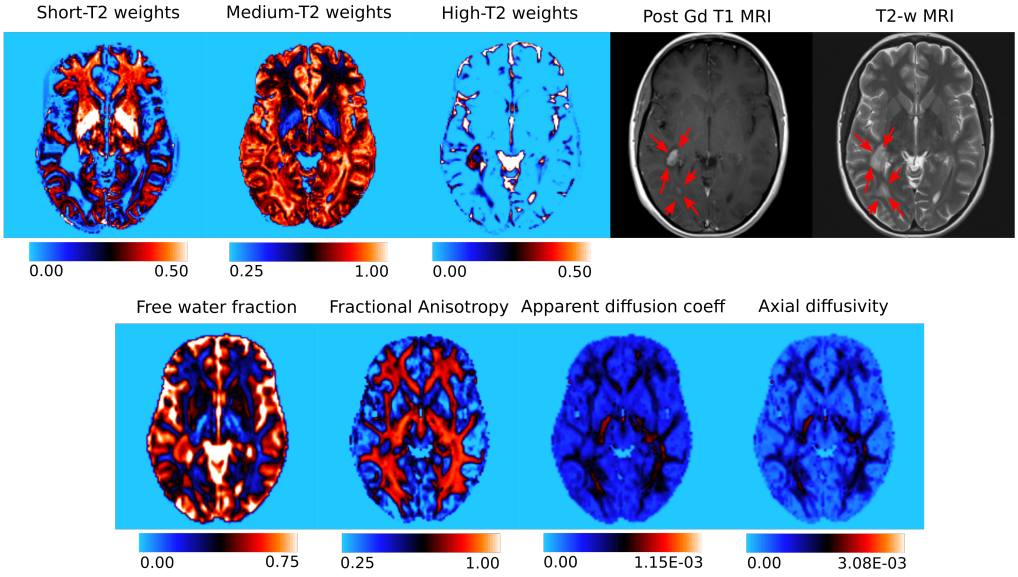

Figure 8.2: The MCT2 and MCDiff maps for a case is shown here as an example. The hyperintense region in the lesion visible on the T_1 weighted image acquired post Gd injection indicates the lesion region undergoing active blood brain barrier breakdown. The same lesion appears as hyperintense in the T_2 weighted image. The hyperintiensity in the T_2 weighted images is larger as it also includes the edema region around the lesion. The estimated MCT2 and MCDiff maps are shown in the top and bottom row respectively.

8.3.2 Experiment 2: Test case evaluation

In this experiment we illustrate the application of the proposed method on a MS patient. We maintain a MS patient dataset which was never used for training the data set in any of the repetitions. The classifier trained in every repetition is used to predict to which category the voxels in the validation image belong. We perform a majority voting on the 100 predictions to decide the final prediction for each voxel. Subsequently we compute the dice measure on the (E+) and (L-) masks to judge the performance of the classifier. The classifier implementation was performed using the scikit-learn package in Python v2.7.

8.4 Results

8.4.1 Experiment 1: Feature evaluation

We show in Fig. 8.3 comparison of the prediction performance of the classifier on validation sets over 100 repititions using features sets derived from: (a) MCT2 model only ($\mathcal{F}_R$), (b) MCDiff model only ($\mathcal{F}_D$) and (c) combination of both ($\mathcal{F}_{RD}$). The mean overall accuracy of prediction when using $\mathcal{F}_{RD}$, $\mathcal{F}_R$ and $\mathcal{F}_D$ are 85.57%, 84.24% and 81.73% respectively. From the overall accuracy plot shown in Fig. 8.3 we observe that combining the microstructure measures from MCT2 and MCDiff model yields better (E+) detection. The true positive rate (TPR) and true negative rate (TNR) plots in Fig. 8.3 show that MCT2 and MCDiff features are better than the other at detecting non-enhanced and enhanced voxels respectively in MS lesions. However, combining both features ($\mathcal{F}_{RD}$) yields better prediction results. Hence we use $\mathcal{F}_{RD}$ for performing predictions in experiment-2.

8.4.2 Experiment 2: Test case evaluation

Results are shown in Fig. 8.4. This MS patient had 18 MS lesions out of which 3 of them had Gd enhancing regions. The dice score for (E+) and (L-) voxel prediction was 0.64 and 0.86 respectively.The top row in Fig. 8.4 shows a lesion which had only (L-) voxels and the proposed method successfully predicted that there were no (E+) voxels in the lesion. The second and third row of Fig. 8.4 shows performance of the method in presence of Gd enhanced voxels in the lesion. Our method identified the (E+) voxels in the lesion. However there were false positives around the Gd enhanced core of the lesions where non-enhancing voxels were identified as belonging to the enhancing region of the lesion.

8.5 Discussion

Our analysis shows that combining tissue microstructure information from multi-compartment T2 relaxometry and diffusion MRI model helps at yielding better prediction accuracy as compared to each feature being used alone. The higher TPR of features derived from MCDiff might be attributed to the fact that during an active

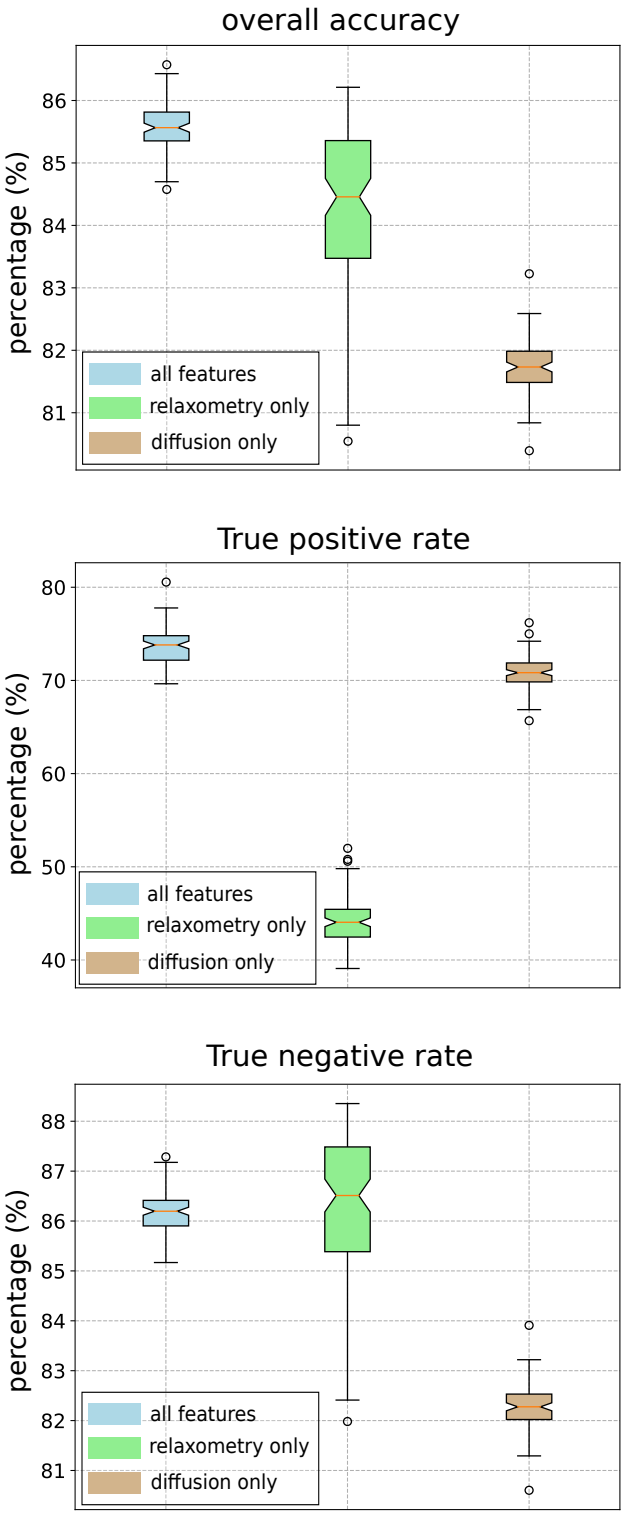

Figure 8.3: (Top to bottom) Overall accuracy, true positive rate and true negative rate of the predictions of the validation set over 100 iterations.

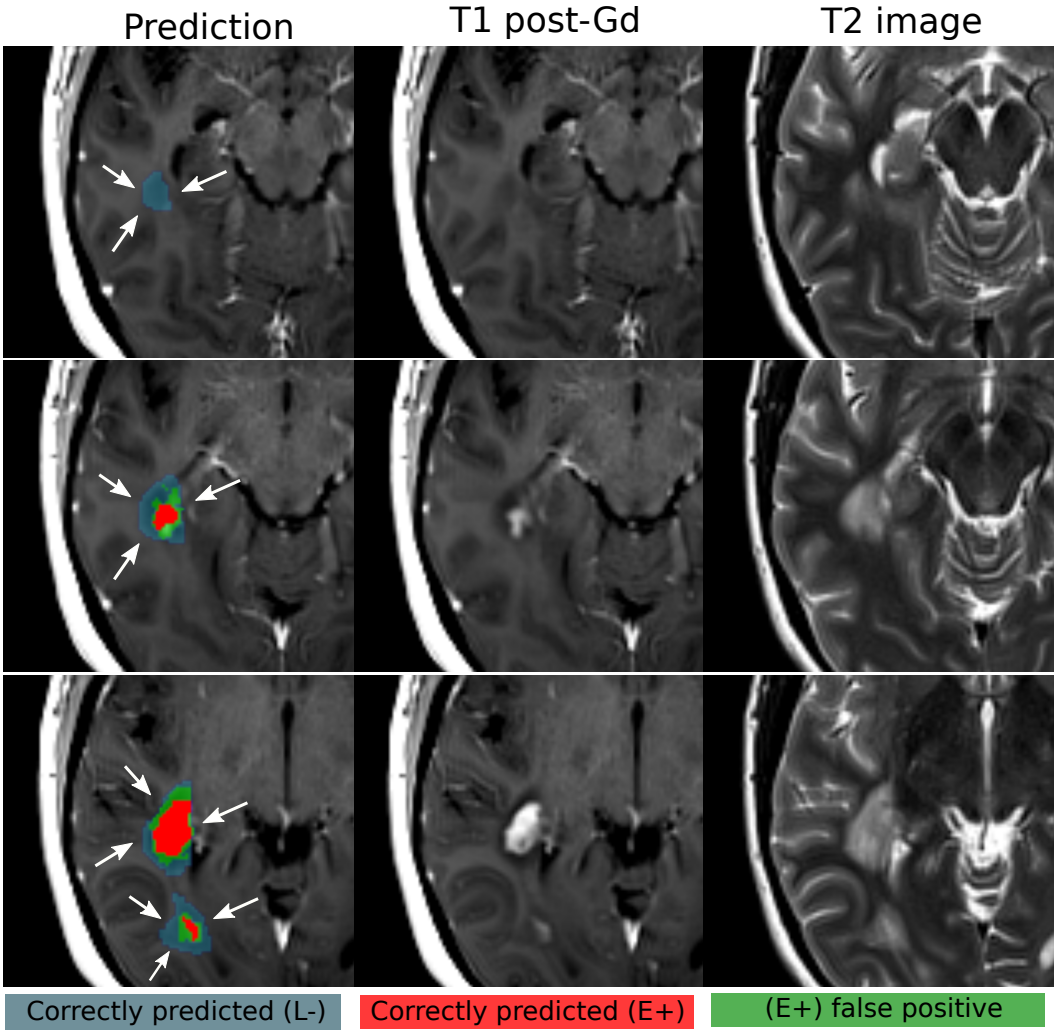

Figure 8.4: The (E+) prediction results on a test image is shown here. Legend for the segmentation labels are shown below the illustrations.

BBB breakdown, there is a greater presence of inter and extra cellular fluid matters and inflammation as compared to non-enhancing parts of the lesion. The high-T2 water fraction from MCT2 model is capable of identifying higher inflammation. However, the medium-T2 water fraction, as described section 8.2.1 is heterogeneous in terms of inter and extra-cellular fluids. However, MCDiff models are able to better explain such scenarios. The non-enhancing regions are demyelinated regions with inflammation which can be explained using MCT2 microstructure information.

Our study has certain limitations. The clinical data used in this work did not favor use of state of the art multi-compartment models. Single b-value data with 30 directions limited us to use a relatively simpler MCM model for MCDiff for reliable estimations. Higher number of echoes and shorter echo times for the T2 relaxometry data will facilitate MCT2 models. However, this study illustrates that even with

clinical protocols, we have good detection of enhanced lesion regions using only MCT2 and MCDiff features.

8.6 Conclusion

We proposed a method to identify MS lesion voxels in which the brain tissues are undergoing active BBB breakdown using brain tissue microstructure information derived from advanced MRI techniques. The proposed method shows promise and motivation to work on improvement of the model from its current form. In the future work, we plan to have uncertainty measures on the predictions so that we can tackle the issue of false positive detection effectively. We also plan to test it on higher quality data to realize the true potential of the current framework.

Part IV

Conclusion

Chapter 9

Conclusion and perspectives

Contents

9.1 Conclusive remarks

There were two major aspects of this thesis. The first objective was to propose and evaluate parametric multi-compartment T_2 relaxometry models and their estimation. The second objective was to demonstrate the potential of the methods proposed in the thesis on a neurodegenerative disease. In this thesis we applied the method on multiple sclerosis (MS) patient data.

9.1.1 Contributions on methods

Two multi-compartment T_2 relaxometry models were proposed in this thesis. The estimation of parameters for such models has been shown to be non-trivial and non-reliable [Layton 2013]. Hence we performed a cost function analysis for each of the models before the problem formulation was finalized. In chapter 5 we proposed a multi-compartment model where each T_2 pool was modeled using a Gaussian probability density function (PDF). Rather than choosing an estimation framework where all parameters and weights are estimated, we adopted a more careful approach where the cost function for the model was analyzed using synthetic data. In this analysis we found that the target cost function for simultaneous estimation of weights and PDF parameters is of a very difficult nature. The convergence to the true value is made tough by presence of a valley of local minima around the true region. Hence we decided to fix the PDF parameters describing each T_2 pool based on values reported in earlier studies. The importance of including the effect of stimulated echoes while using T_2 relaxometry data from fast spin echo sequences has been reported in the literature [Prasloski 2012]. The stimulated echoes were accounted for using the extended phase graph (EPG) algorithm [Prasloski 2012, Layton 2013]. The flip angle

error (FAE) percentage required to compute the EPG is estimated in the proposed method.

It has been observed in the literature that pathologies such as multiple sclerosis cause a shift in the spectrum of the T_2 pools. Fig. 1 in [Laule 2007c] adds credence to this argument. In chapter 6 we realized a more complex model. The objective of the proposed was to identify the best possible framework for which the PDF parameters of the T_2 pools and their associated weights can be estimated. The underlying idea was to observe whether an estimation framework where the PDF parameters are estimated along with the weights is able to confirm such reports. The complexity of the problem was limited to estimating the shift (i.e. mean) parameter of the PDFs. A variable projection (VARPRO) approach was adopted to solve to the optimization problem [Golub 2003]. The cost function to be optimized with respect to the weights and PDF parameters was reduced to an optimization problem only with respect to the PDF parameters in the VARPRO formulation. The weights were later obtained as discussed in chapter 6 [Golub 2003]. As for chapter 5, we analyzed the VARPRO cost function on feasibility of simultaneous estimation of the T_2 pool PDF means. The cost functions for in-vivo brain MRI data were used to investigate nature of the VARPRO cost function. This analysis revealed the difficult nature of the cost function. The observations suggested that for short T_2 pool PDF mean, the cost function always converged at the minimum bound set for optimization. Hence we decided to optimize only for the PDF mean of the medium T_2 pool. The FAE was estimated to account for the effect of stimulated echoes.

Both methods were validated on synthetic data with known ground truth and in-vivo phantom data. The water fractions estimated by the methods were close to the ground truth. Even at low SNR the method performs well. The experiments on in-vivo phantom data showed that the proposed method adapted well to scenarios where mono T_2 solutions were imaged. One in-vivo phantom had mono T_2 solutions with T_2 values gradually increasing from around $15ms$ to $600ms$. The estimated water fractions showed a gradual shift of weights from the short T_2 pool, to the medium T_2 pool and finally to the high T_2 pool as the T_2 values of the imaged solutions increased. Once the validation was performed on known ground truths, estimation maps for the in-vivo brain MRI were observed. Repeatability is an important aspect of quantitative biomarkers (especially when used for longitudinal studies). The values on multiple white matter regions were compared for test-retest data acquired on four healthy volunteers. The estimated water fraction values for the test and retest data were in good agreement. The performance of the methods in the presence of pathologies is of critical importance. Both methods were evaluated on MS patients. The short T_2 water fraction map showed very low values in the lesion regions when compared to the normal appearing white matter regions in MS patients. This indicated demyelination in these regions. Presence of high T_2 component in some white matter lesions indicated edema presence. Hence, the proposed methods detects] the long T_2 component which has been shown to be present in MS lesions [Laule 2007b, Laule 2007c]. The estimated PDF mean for the medium T_2 pool using the method proposed in chapter 6 showed interesting results in the

case of pathologies. The medium T_2 pool spectrum showed a shift towards higher T_2 value as compared to the normal appearing white matter. This is in accordance with observations from previous studies [Laule 2007c].

The study revealed the difficult nature of parameter estimation, especially for the T_2 pool PDF parameters. However with an appropriate choice of the T_2 pools PDF parameters, the weights estimation has been found to be robust and reliable. The observations suggest that estimating PDF parameters of all the T_2 pools and their weights might lead the estimated PDF parameters hitting the upper/lower bounds set for optimization in each case. The proposed methods do not require any regularization terms to enforce spatial smoothness. The validation and evaluations of the methods demonstrated their potential in quantifying tissue microstructures in brain tissues from T_2 relaxometry data. Application of the method on MS patient cases showed that the water fraction maps estimated from these methods can act as useful biomarkers for neurodegenerative disease such as MS. Repeatability experiment results showed that these methods can be used for longitudinal studies.

9.1.2 Contributions on applications in MS

In the first application discussed in chapter 7 we studied and compared the evolution of weights of the three T_2 compartments in active and inactive regions of MS lesions in 10 patients with clinically isolated syndrome (CIS) over a period of three years. The method proposed in chapter 5 was used for obtaining the water fraction maps from T_2 relaxometry data. This study was performed on a retrospective clinical data. The T_2 relaxometry data was acquired under 8 minutes with fewer echoes and greater echo spacing (7 echoes; 13.8ms spacing) than the data used for repeatability experiments (32 echoes; 9ms spacing). Hence, we compared the performance of water fraction estimation while using the protocol as in the clinical trial and a standard T_2 relaxometry protocol (which was also used for repeatability experiments). Simulations were performed using the synthetic phantom data for varying levels of SNR. The synthetic phantom had five sections. Three sections resembled NAWM, one section had MS lesion-like water fraction values and the remaining section resembled free water. The operating range of SNR for the data used in clinical study was around 100. The NAWM regions showed around 5% and less than 2% relative difference in estimations of the short T_2 and medium T_2 water fraction values while using the protocol used for the MS study compared to the protocol used for the repeatability study in Chapter 5. The lesion like section showed a relative difference of around 9% and less than 2% and approximately 5% for the short T_2, medium T_2 and high T_2 water fraction estimates respectively. A paired t-test showed no significant differences (p-value>0.05) between the water fraction estimates from the two protocols for all compartments for the operating SNR range. This experiment demonstrated the robustness of the method in terms of being applicable to T_2 relaxometry data acquired under low scan times with fewer echoes and larger echo spacings. With this observation, we performed the longitudinal study on patients. There were two main observations from the longitudinal study: (i) the active lesions

regions showed activity latest till 9 months from the baseline scan, and (ii) significant differences were observed in the short T_2 and high T_2 water fractions values between the active and inactive regions only at the baseline scan. The follow-up scan to the baseline was performed after 3 months. The water fraction evolution trend indicated signs of remyelination and subsiding inflammation in lesion regions (especially in the active lesion regions). One recommendation which emerges from the observations of this chapter is the importance of interpreting the changes in the short T_2 component in conjunction with the changes observed in the representation of other T_2 compartments in the lesions. Traditionally studies have focused only on evolution of the short T_2 components in the tissues which is an indicator of myelin. However, myelin being judges only on the basis of myelin water fraction (MWF) is not appropriate as the MWF can be influenced by an increasing/decreasing amount of water in the lesions due to inflammation in affected tissues.

In chapter 8 we addressed a critical and challenging clinical problem. An increasing number of reports are raising concerns on the retention of gadolinium in brain tissues due to its repeated usage. While there are health concerns surrounding this retention, this phenomenon has also lead to observable signal changes in the brain MRI. Moreover, administration of gadolinium to patients with renal complications is not possible. However, the importance of identifying enhancing lesions in MS patients using gadolinium injection has been well established. In this chapter we proposed a method to identify gadolinium enhanced regions in MS lesions using tissue microstructure information obtained from T_2 relaxometry and diffusion MRI data. The T_2 relaxometry microstrucutre information was obtained using the method proposed in chapter 5. This chapter had two important observations. The tissue microstructure information obtained from T_2 relaxometry and diffusion MRI data complemented each other. Whereas the tissue microstructure information obtained from diffusion MRI was more effective at identifying the active regions of the lesion, the T_2 relaxometry microstructure information performs better at identifying non-enhancing lesion regions. The experiment on the test case demonstrated the potential of the proposed framework in detecting active regions in the MS lesions without using gadolinium contrast agent injection.

9.1.3 Thesis related publications

Preprint

[1] **Sudhanya Chatterjee**, Olivier Commowick, Onur Afacan, Benoit Combes, Simon K. Warfield, and Christian Barillot. "A three year follow-up study of gadolinium enhanced and non-enhanced regions in multiple sclerosis lesions using a multi-compartment T2 relaxometry model." bioRxiv (2018): 365379.

Peer reviewed conference papers

[1] **Sudhanya Chatterjee**, Olivier Commowick, Onur Afacan, Simon K. Warfield, and Christian Barillot. "Multi-compartment model of brain tissues from T2

relaxometry MRI using gamma distribution." In Biomedical Imaging (ISBI 2018), 2018 IEEE 15th International Symposium on, pp. 141-144. IEEE, 2018.

[2] **Sudhanya Chatterjee**, Olivier Commowick, Onur Afacan, Simon K. Warfield, and Christian Barillot. "Identification of Gadolinium contrast enhanced regions in MS lesions using brain tissue microstructure information obtained from diffusion and T2 relaxometry MRI." In International Conference on Medical Image Computing and Computer-Assisted Intervention, pp. 63-71. Springer, Cham, 2018.

Peer review conference abstracts

[1] **Sudhanya Chatterjee**, Olivier Commowick, Onur Afacan, Benoît Combès, Anne Kerbrat, Simon Warfield, and Christian Barillot. "A 3-year follow-up study of enhancing and non-enhancing multiple sclerosis (MS) lesions in MS patients demonstrating clinically isolated syndrome (CIS) using a multi-compartment T2 relaxometry (MCT2) model." In ISMRM Annual Meeting 2018. 2018. *[Oral]*

[2] **Sudhanya Chatterjee**, Olivier Commowick, Simon Warfield, and Christian Barillot. "Gaining Insights Into Multiple Sclerosis Lesion Characteristics from Brain Tissue Microstructure Information: A Multi-Compartment T2 Relaxometry Approach." In ISMRM 25TH annual meeting and exhibition. 2017.

[3] **Sudhanya Chatterjee**, Olivier Commowick, Simon K. Warfield, and Christian Barillot. "Multi-Compartment T2 Relaxometry Model Using Gamma Distribution Representations: A Framework for Quantitative Estimation of Brain Tissue Microstructures." In ISMRM 25TH annual meeting and exhibition. 2017.

Currently we are in the process of submitting the pre-print to a journal by including the simulation results discussed in chapter 5 and 7. The work discussed in chapter 6 is an extension of a conference paper mentioned above and shall be submitted to a peer reviewed journal. The work discussed in chapter 8 will also be extended with a different problem formulation and then submitted for review in the coming months.

9.2 Perspectives

The multi-compartment models where T_2 pool compartments are described using continuous functions PDFs do not require regularization terms for imposing smoothness and perform better on low SNR data as compared to multi-component T_2 relaxometry models. Mackay and Laule raised a concern on behavior of such models in presence of T_2 pools which are not accounted for in the model [MacKay 2016].

This can be addresses in a few ways. To start with, simulations along the lines of [Graham 1996] can be performed to detect the resolution capability of parametric models for multiple T_2 pools which lie in close proximity. The results however might be similar to the findings of Graham et al. that at low SNRs, the resolution capability might be limited [Graham 1996]. Another analysis can be carried out on figuring out the interplay between weights of the PDFs and their parameters. From the observations made in this work, when the PDF parameters are fixed we can expect to see more variations in the weights in case of pathologies. And on the other hand, when the PDF parameters are varied the weights in the pathology regions remain more or less the same. So the degree of freedom when optimizing for the weights and PDF parameters can be evaluated to conclude whether there is value in performing such complex estimations. These experiments will also usher more light on the interpretation of the estimated parameters of the multi-compartment T_2 relaxometry models.

In our work, we showed the difficult nature of simultaneously estimating the PDF parameters and its weights for the T_2 pools. We also show that even the problem of simultaneously estimating the PDF parameters alone is quite challenging and prone to hitting the boundaries set for optimization of the parameters. All this work was performed based on simulations on synthetic and in-vivo brain MRI data. Although this establishes the difficult nature of such estimations, it would be fruitful to have a rigorous mathematical analysis of such models to state the underlying cause for such behavior. The presence of stimulated echoes (and hence invalidity of pure exponential analysis) does make this task very challenging.

The other interesting aspect to look into is the relation between the T_2 relaxometry and diffusion MRI derived microstructures. Recent works have shown great potential by proposing a variety of models in this field. Benjamini et al. proposed a framework for creating such 2D spectra by using marginal distributions [Benjamini 2016]. Kim et al. on the other hand proposed joint signal model to identify diffusion and relaxation components using diffusion-relaxation correlation spectroscopic imaging [Kim 2017]. The basic idea is that by having both diffusion and relaxation information in the same voxel, the ill-posed nature of the multi-exponential model is reduced. Although this is a very powerful and effective tool, acquiring such data is extremely time consuming. The other approach is to combine myelin water fraction and diffusion microstructure to obtain biomarkers such as g-ratio [Campbell 2017]. Combination of biomarkers from T_2 relaxometry and diffusion MRI makes it implicit that the obtained biomarkers are held to high standards of accuracy and reliability. All models have underlying assumptions which affects the estimation in some way or the other. This might be due to reliance of the methods on certain specifications of acquisition or the estimation framework itself. When the biomarkers from two methods such as relaxometry and diffusion MRI acquired separately are combined using metrics such as ratios, linear combinations etc. such effects become difficult to track. This might become a more pertinent challenge when dealing with pathologies. Hence, if at all a joint signal model and biomarker is aspired for, the methods proposed by [Benjamini 2016] and [Kim 2017]

are ideal. However, it is difficult to dedicate so much time for acquisition when clinical studies are conducted. Keeping all these in mind, for clinical T_2 relaxometry and diffusion MRI data using the type of method proposed in chapter 8 is more justified. The study performed in chapter 8 can be carried out in greater depth where a feature wise analysis for prediction effectiveness can be performed. Multi-compartment diffusion MRI models can be adapted for single shell data with better initializations and analysis techniques. This does not recommend against multiple b-value diffusion MRI data acquisition for clinical studies. Recent advances allow acquisition of high quality diffusion MRI data in under 8 minutes. However, there are lot of clinical studies which have single shell diffusion MRI data which can be used for providing valuable insights to the research community.

Part V

Appendix

Appendix A

Synthetic phantom

A synthetic phantom is created to validate the multi-compartment T_2 relaxoemtry methods proposed in this thesis. Sections are created in the phantom with different water fraction and B_1 scale factor values. There are five sections in the phantom with different water fraction values. An illustration of the sections with different water fraction values are shown in Fig. A.1. The water fraction values corresponding to each section in shown in Table A.1.

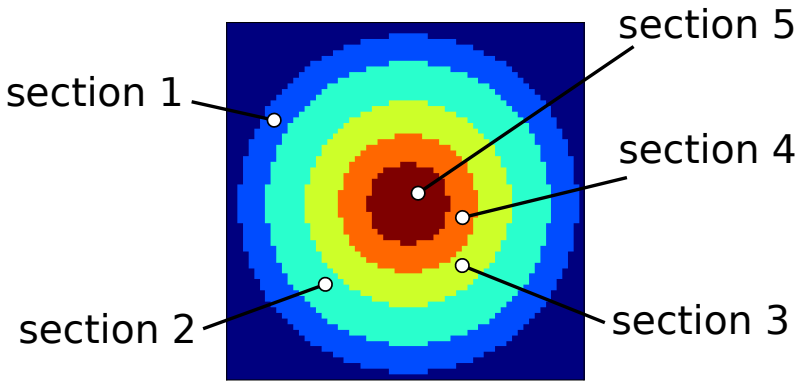

Figure A.1: The different sections in the synthetic phantom consisting of multi-compartment T_2 relaxometry voxels with varying short, medium and high T_2 water fraction values are shown here.

	short T2	*medium T2*	*high T2*
Section 1	0.20	0.79	0.01
Section 2	0.15	0.84	0.10
Section 3	0.10	0.85	0.05
Section 4	0.05	0.75	0.20
Section 5	0.01	0.01	0.98

Table A.1: The water fraction values for the short, medium and high T_2 compartments for the different sections of the phantom shown in Fig. A.1 are provided here.

Section 1 in the phantom is representation of voxels which have free water, such as cerebrospinal fluids. The section 2 of phantom contains voxels emulating MS

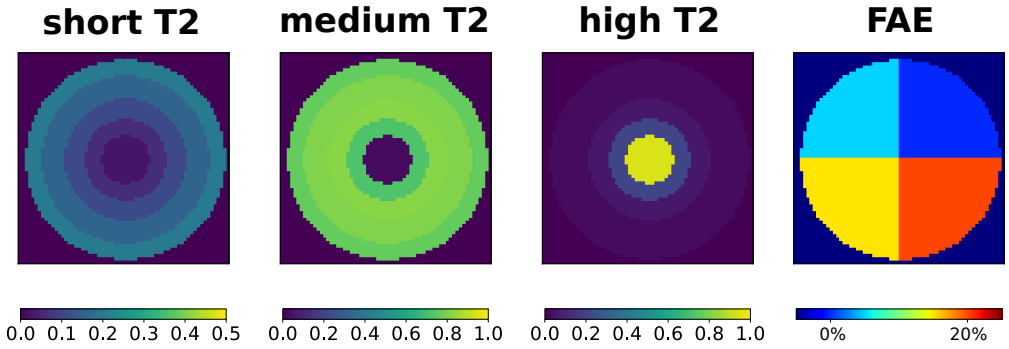

Figure A.2: True values of the B_1 scale water, short T_2, medium T_2 and high T_2 water fraction for the synthetic phantom are shown here.

lesions with a representation of 5% and 20% from the short and high T_2 compartments. The low short T_2 and presence of high T_2 water fraction are chosen to account for the demyelination and edema formation observed in the MS lesions. Sections 3, 4 and 5 are created with water fraction values chosen so as to represent normal appearing white matter tissues. In addition to having sections with varying contributions from the T_2 relaxometry compartments, the phantom contains four sections with different B_1 scale factor values. The multiple echo spin echo sequences are well known to have stimulated echo effects [Crawley 1987]. Hence it is important to account for them in the simulations. The true maps for the B_1 scale factors and water fraction values of the compartments are shown in Fig. A.2. The B_1 scale factor values chosen for simulation are: $\{1.0, 1.05, 1.1, 1.2\}$. The T_1 value for the whole phantom is chosen as 1000ms.

Algorithm 1 Generating Synthetic Phantom

Require: B_1, $sT2$, $mT2$, $hT2$ $\rightarrow$ Maps containing true values of B_1 scale factor, short, medium and high T_2 water fraction values.
Require: $S \rightarrow$ SNR level of the image to be generated.
Require: $n_{base} \rightarrow$ number of T_2 curves required to compose each voxel.
Require: e, n_e: echo spacing (in millisecond), number of echoes.
1: **for** $(i, j) \in$ phantom **do**
2: $n_s = sT2(i,j) \times n_{base}$; $n_m = mT2(i,j) \times n_{base}$; $n_h = hT2(i,j) \times n_{base}$
3: Draw $s \in \mathbb{R}^{n_s}$, $m \in \mathbb{R}^{n_m}$ and $h \in \mathbb{R}^{n_h}$ randomly from gaussian probability distributions as $\mathcal{N}(20,5)$, $\mathcal{N}(100,10)$ and $\mathcal{N}(2000,80)$ respectively.
4: $\mathsf{short}(i,j) = \sum_s \mathsf{GenerateEPG}\,[s(k), B_1(i,j), e, n_e]$
$\mathsf{medium}(i,j) = \sum_m \mathsf{GenerateEPG}\,[m(k), B_1(i,j), e, n_e]$
$\mathsf{high}(i,j) = \sum_h \mathsf{GenerateEPG}\,[h(k), B_1(i,j), e, n_e]$
5: $\mathsf{phantom}(i,j) = \mathsf{short}(i,j) + \mathsf{medium}(i,j) + \mathsf{high}(i,j)$, $\mathsf{phantom}(i,j) \in \mathbb{R}^{n_e}$
6: $\mathsf{phantom}(i,j) += \mathsf{noise}(S)$

The voxels of the synthetic phantom are generated as described in Algorithm

1. Each voxel in the synthetic phantom is composed of 50 ($= n_{base}$) T_2 curves in proportion of the true water fraction values as shown in Fig. A.2. Instead of using the pure exponentials, we account for the stimulated echoes [Crawley 1987] using the extended phase graph (EPG) method [Prasloski 2012, Layton 2013]. The B_1 scale factor for generating the EPG curve is chosen from the true B_1 map shown in Fig. A.2. The T_2 curve for a voxel from each section for different B_1 values are shown in Fig. A.3. The simulations are performed for six levels of additive Gaussian noise. The SNR values evaluated are {50, 75, 100, 200, 500, 1000}. The SNR is stated with respect to the signal value at first echo. The T_2 curves were generated for two specifications: (i) echo spacing = 9.0ms, echo train length = 32 and (ii) echo spacing = 13.8ms, echo train length = 7.

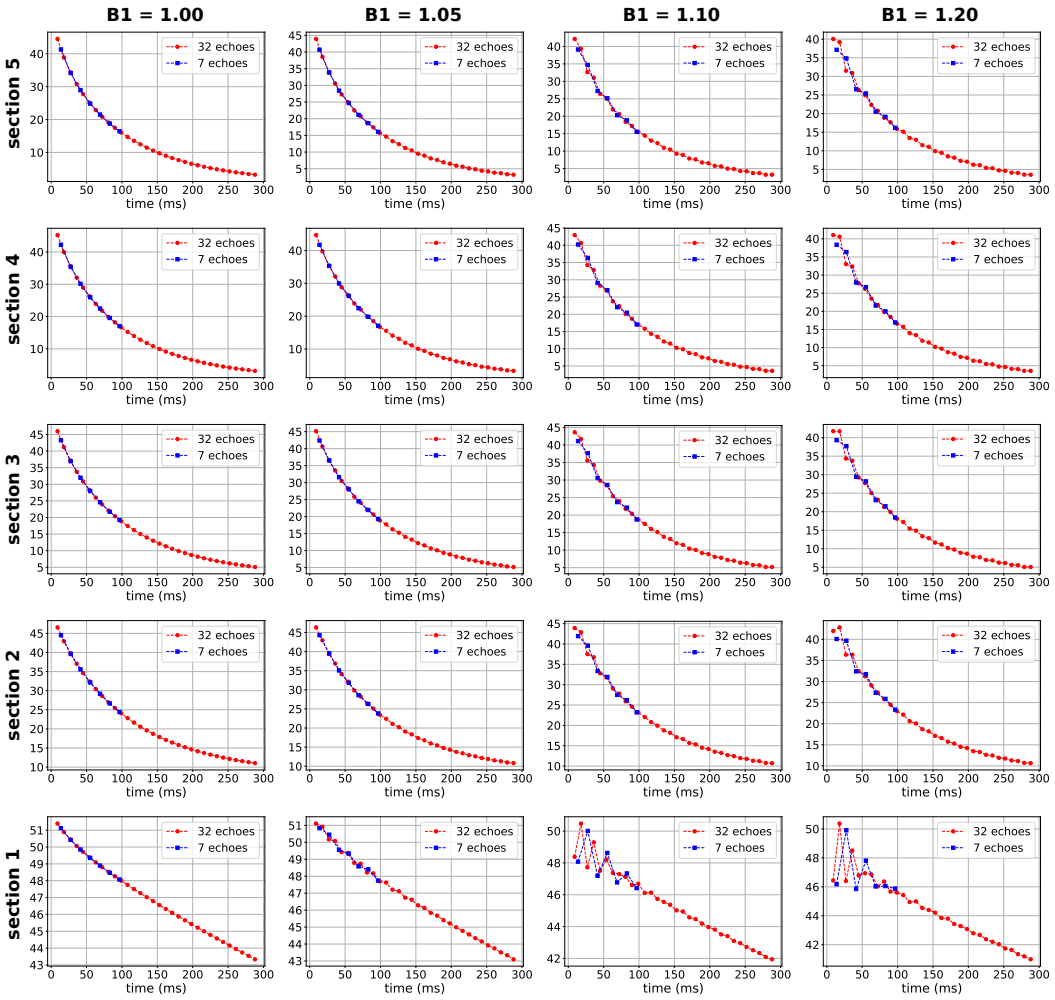

Figure A.3: The T_2 decay curves for all a voxel from each section with the different B_1 values are shown here. The sections mentioned in the figure are the same as those annotated in Fig. A.1. The water fraction values for the sections are provided in Table A.1.

Appendix B

Gradient computation for VARPRO cost function

The variable projection (VARPRO) technique is useful for solving least square problems where the non-linear variables are linearly combined [Golub 2003]. Here we present the computation of gradient for solving the VARPRO formulation. We have a similar problem in Chapter 6 (refer Eq. 6.2 in Section 6.2.1). As mentioned in Section 6.2.1, we optimize for the PDF parameters and its associated weights, and the field inhomogeneity factor in separate steps. The original cost function (refer Eq. 6.2) is restated below:

$$\arg\min_{\mu,\alpha} \|Y - \Lambda(\mu)\,\alpha\|_2^2 \tag{B.1}$$

where $Y \in \mathbb{R}^m$ is the observed signal; $\alpha \in \mathbb{R}^{+^3}$ is the weighted contribution of each gamma PDF to the signal; μ is the mean of the gamma PDF representing the medium T_2 compartment and $\Lambda(\mu) \in \mathbb{R}^{m\times 3}$ is an internal term of the signal model (with 3 compartments). The i-th row and j-th columns element of $\Lambda(\mu)$ is shown below:

$$\Lambda_{ij}(\mu) = \int_{T_2} f(T_2;\mu,v)\, EPG(T_2, T_1, B_1, i_{echo})\, dT_2 \tag{B.2}$$

In Eq. (B.2), $f(\cdot)$ is the gamma PDF with mean and variance as PDF parameters. As elaborated in Chapter 6, we only optimize for the mean of the medium T_2 gamma PDF. In the VARPRO formulation, α in Eq. (B.1) is substituted by $\Lambda(\mu)^\dagger Y$. $\Lambda(\mu)^\dagger$ is the Moore-Penrose pseudo inverse of $\Lambda(\mu)$. Hence, the VARPRO cost function is as shown below:

$$C = \left|\left|\left(I - \Lambda(\mu)\Lambda(\mu)^\dagger\right) Y\right|\right|_2^2 \tag{B.3}$$

Henceforth we will use only Λ for $\Lambda(\mu)$ as in our work this internal terms is only a function of mean of the gamma PDF representing the medium T_2 compartment. The aim is to minimize the error function with respect to the variable: μ. The error function in this case is:

$$e = \left(I - \Lambda\Lambda^\dagger\right) Y \tag{B.4}$$

The gradient with respect to the variable is obtained as shown below:

$$g = \frac{\partial\left(e^T e\right)}{\partial\mu} = e^T\frac{\partial e}{\partial\mu} + \frac{\partial e^T}{\partial\mu}\,e = 2\,e^T\frac{\partial e}{\partial\mu} \tag{B.5}$$

The Jacobian term to compute g in Eq. (B.5) is obtained as follows:

$$J = \frac{\partial e}{\partial \mu} = -\frac{\partial \left(\Lambda\Lambda^{\dagger}\right)}{\partial \mu} Y \tag{B.6}$$

The expression to obtain the elements of Jacobian matrix is provided in [Golub 2003]. However, a brief derivation of the same is shown here for convenience of the reader. The derivation is performed assuming that the optimization problem is to minimize the cost function with respect to a single variable (μ).

We need to obtain the expression for $\partial\left(\Lambda\Lambda^{\dagger}\right) / \partial\mu$ to compute the Jacobian shown in Eq. (B.6). Note that the term $\Lambda\Lambda^{\dagger}$ in Eq. (B.6) can be substituted by $\left(\Lambda\Lambda^{\dagger}\right)\left(\Lambda\Lambda^{\dagger}\right)$. Hence $\partial\left(\Lambda\Lambda^{\dagger}\right) / \partial\mu$ in Eq. (B.6) can be computed as shown below:

$$\begin{aligned}\frac{\partial \left(\Lambda\Lambda^{\dagger}\right)}{\partial \mu} &= \frac{\partial \left(\left(\Lambda\Lambda^{\dagger}\right)\left(\Lambda\Lambda^{\dagger}\right)\right)}{\partial \mu} \\ &= \left[\left(\Lambda\Lambda^{\dagger}\right)\frac{\partial \left(\Lambda\Lambda^{\dagger}\right)}{\partial \mu}\right] + \left[\frac{\partial \left(\Lambda\Lambda^{\dagger}\right)}{\partial \mu}\left(\Lambda\Lambda^{\dagger}\right)\right]\end{aligned} \tag{B.7}$$

Note that $\Lambda\Lambda^{\dagger}$ is symmetric. Hence Eq. (B.7) can be re-written as:

$$\frac{\partial \left(\Lambda\Lambda^{\dagger}\right)}{\partial \mu} = \left[\frac{\partial \left(\Lambda\Lambda^{\dagger}\right)}{\partial \mu}\left(\Lambda\Lambda^{\dagger}\right)\right] + \left[\frac{\partial \left(\Lambda\Lambda^{\dagger}\right)}{\partial \mu}\left(\Lambda\Lambda^{\dagger}\right)\right]^{T} \tag{B.8}$$

Hence we need to compute only the first term in Eq. (B.8) to obtain the elements of the jacobian matrix. Since Λ is same as $\Lambda\Lambda^{\dagger}\Lambda$, we may write the derivative of Λ with respect to μ as:

$$\begin{aligned}\frac{\partial \Lambda}{\partial \mu} &= \frac{\partial \left[\left(\Lambda\Lambda^{\dagger}\right)\Lambda\right]}{\partial \mu} \\ &= \left(\Lambda\Lambda^{\dagger}\right)\frac{\partial \Lambda}{\partial \mu} + \frac{\partial \left(\Lambda\Lambda^{\dagger}\right)}{\partial \mu}\Lambda\end{aligned} \tag{B.9}$$

Rearranging the terms in Eq. (B.9) we obtain:

$$\begin{aligned}\frac{\partial \left(\Lambda\Lambda^{\dagger}\right)}{\partial \mu}\Lambda &= \frac{\partial \Lambda}{\partial \mu} - \left(\Lambda\Lambda^{\dagger}\right)\frac{\partial \Lambda}{\partial \mu} \\ &= \left(1 - \Lambda\Lambda^{\dagger}\right)\frac{\partial \Lambda}{\partial \mu} = P_{\Lambda}^{\perp}\frac{\partial \Lambda}{\partial \mu}\end{aligned} \tag{B.10}$$

Multiplying the left and right hand sides of Eq. (B.10) by $\Lambda^{\dagger}$ we obtain:

$$\begin{aligned}\frac{\partial \left(\Lambda\Lambda^{\dagger}\right)}{\partial \mu}\Lambda\Lambda^{\dagger} &= P_{\Lambda}^{\perp}\frac{\partial \Lambda}{\partial \mu}\Lambda^{\dagger} \\ \frac{\partial \left(\Lambda\Lambda^{\dagger}\right)}{\partial \mu} &= P_{\Lambda}^{\perp}\frac{\partial \Lambda}{\partial \mu}\Lambda^{\dagger}\end{aligned} \tag{B.11}$$

Using the expression obtained in Eq. (B.11), the first term on the right hand side of Eq. (B.8) can be written as:

$$\begin{aligned}\frac{\partial\left(\Lambda\Lambda^{\dagger}\right)}{\partial\mu}\left(\Lambda\Lambda^{\dagger}\right) &= \left(P_{\Lambda}^{\perp}\frac{\partial\Lambda}{\partial\mu}\Lambda^{\dagger}\right)\left(\Lambda\Lambda^{\dagger}\right)\\ &= P_{\Lambda}^{\perp}\,\frac{\partial\Lambda}{\partial\mu}\,\Lambda^{\dagger}\end{aligned} \tag{B.12}$$

Substituting the result of Eq. (B.12) and (B.8) in the Jacobian formulation shown in Eq. (B.6), we obtain:

$$J = -\left[\left(P_{\Lambda}^{\perp}\,\frac{\partial\Lambda}{\partial\mu}\,\Lambda^{\dagger}\right) + \left(P_{\Lambda}^{\perp}\,\frac{\partial\Lambda}{\partial\mu}\,\Lambda^{\dagger}\right)^{T}\right] Y \tag{B.13}$$

The expression for the Jacobian from Eq. (B.13) can be substituted in the gradient formulation shown in Eq. (B.5) to obtain the gradient update term as follows:

$$g = -2\,e^{T}\,\left[\left(P_{\Lambda}^{\perp}\,\frac{\partial\Lambda}{\partial\mu}\,\Lambda^{\dagger}\right) + \left(P_{\Lambda}^{\perp}\,\frac{\partial\Lambda}{\partial\mu}\,\Lambda^{\dagger}\right)^{T}\right] Y \tag{B.14}$$

Hence to the gradient update values can be obtained by deriving the expression for $\partial\Lambda/\ \partial\mu$ for our problem.

List of Tables

List of Figures

Bibliography

[Akhondi-Asl 2015] Alireza Akhondi-Asl, Onur Afacan, Mukund Balasubramanian, Robert V Mulkern and Simon K Warfield. *Fast myelin water fraction estimation using 2D multislice CPMG.* Magnetic resonance in medicine, 2015. (Cited on pages 15, 16 and 66.)

[Alonso-Ortiz 2015] Eva Alonso-Ortiz, Ives R Levesque and G Bruce Pike. *MRI-based myelin water imaging: A technical review.* Magnetic Resonance in Medicine, vol. 73, no. 1, pages 70–81, 2015. (Cited on page 14.)

[Bakshi 2008] Rohit Bakshi, Alan J Thompson, Maria a Rocca, Daniel Pelletier, Vincent Dousset, Frederik Barkhof, Matilde Inglese, Charles R G Guttmann, Mark a Horsfield and Massimo Filippi. *MRI in multiple sclerosis: current status and future prospects.* Lancet neurology, vol. 7, no. 7, pages 615–625, 2008. (Cited on page 26.)

[Barillot 2016] Christian Barillot, Gilles Edan and Olivier Commowick. *Imaging biomarkers in multiple Sclerosis: From image analysis to population imaging.* Medical Image Analysis, no. 33, pages 134–139, 2016. (Cited on pages 25 and 85.)

[Benjamini 2016] Dan Benjamini and Peter J Basser. *Use of marginal distributions constrained optimization (MADCO) for accelerated 2D MRI relaxometry and diffusometry.* Journal of magnetic resonance, vol. 271, pages 40–45, 2016. (Cited on page 126.)

[Bloch 1946] Felix Bloch. *Nuclear induction.* Physical review, vol. 70, no. 7-8, page 460, 1946. (Cited on page 3.)

[Brown 2014] Robert W Brown, E Mark Haacke, Y-C Norman Cheng, Michael R Thompson and Ramesh Venkatesan. Magnetic resonance imaging: physical principles and sequence design. John Wiley & Sons, 2014. (Cited on pages 5, 7, 8 and 141.)

[Brownlee 2017] Wallace J Brownlee, Todd A Hardy, Franz Fazekas and David H Miller. *Diagnosis of multiple sclerosis: progress and challenges.* The Lancet, vol. 389, no. 10076, pages 1336–1346, 2017. (Cited on page 109.)

[Brück 1995] Wolfgang Brück, Phyllis Porada, Sigrid Poser, Peter Rieckmann, Folker Hanefeld, Hans A Kretzschmarch and Hans Lassmann. *Monocyte/macrophage differentiation in early multiple sclerosis lesions.* Annals of neurology, vol. 38, no. 5, pages 788–796, 1995. (Cited on pages 24 and 139.)

[Callaghan 1993] Paul T. Callaghan. Principles of nuclear magnetic resonance microscopy. Oxford University Press on Demand, 1993. (Cited on page 3.)

[Campbell 2017] Jennifer SW Campbell, Ilana R Leppert, Sridar Narayanan, Mathieu Boudreau, Tanguy Duval, Julien Cohen-Adad, G Bruce Pike and Nikola Stikov. *Promise and pitfalls of g-ratio estimation with MRI.* Neuroimage, 2017. (Cited on page 126.)

[Carr 1954] Herman Y Carr and Edward M Purcell. *Effects of diffusion on free precession in nuclear magnetic resonance experiments.* Physical review, vol. 94, no. 3, page 630, 1954. (Cited on pages 7 and 33.)

[Commowick 2012] Olivier Commowick, Nicolas Wiest-Daesslé and Sylvain Prima. *Block-matching strategies for rigid registration of multimodal medical images.* In Biomedical Imaging (ISBI), 2012 9th IEEE International Symposium on, pages 700–703. IEEE, 2012. (Cited on pages 51, 52, 75, 94 and 113.)

[Cortes 1995] Corinna Cortes and Vladimir Vapnik. *Support-vector networks.* Machine learning, vol. 20, no. 3, pages 273–297, 1995. (Cited on page 114.)

[Crawley 1987] AP Crawley and RM Henkelman. *Errors in T2 estimation using multislice multiple-echo imaging.* Magnetic resonance in medicine, vol. 4, no. 1, pages 34–47, 1987. (Cited on pages 7, 33, 42, 48, 111, 132 and 133.)

[Does 2018] Mark D Does. *Inferring brain tissue composition and microstructure via MR relaxometry.* NeuroImage, 2018. (Cited on pages 11, 14, 33 and 63.)

[Fenrich 2001] FRE Fenrich, C Beaulieu and PS Allen. *Relaxation times and microstructures.* NMR in Biomedicine: An International Journal Devoted to the Development and Application of Magnetic Resonance In Vivo, vol. 14, no. 2, pages 133–139, 2001. (Cited on pages 12, 13 and 141.)

[Ferguson 1997] B. Ferguson, M. K. Matyszak, M. M. Esiri and V. H. Perry. *Axonal damage in acute multiple sclerosis lesions.* Brain, vol. 120, no. 3, pages 393–399, 1997. (Cited on page 17.)

[Golub 2003] Gene Golub and Victor Pereyra. *Separable nonlinear least squares: the variable projection method and its applications.* Inverse Problems, vol. 19, no. 2, pages R1–R26, 2003. (Cited on pages 16, 36, 67, 71, 122, 135 and 136.)

[Graham 1996] Simon J Graham, Peter L Stanchev and Michael J Bronskill. *Criteria for analysis of multicomponent tissue T2 relaxation data.* Magnetic Resonance in Medicine, vol. 35, no. 3, pages 370–378, 1996. (Cited on pages 12 and 126.)

[Grissom 2005] Robert J Grissom and John J Kim. Effect sizes for research: A broad practical approach. Lawrence Erlbaum Associates Publishers, 2005. (Cited on page 100.)

[Gulani 2017] Vikas Gulani, Fernando Calamante, Frank G Shellock, Emanuel Kanal, Scott B Reeder*et al. Gadolinium deposition in the brain: summary of*

evidence and recommendations. The Lancet Neurology, vol. 16, no. 7, pages 564–570, 2017. (Cited on page 110.)

[Guttmann 1995] CR Guttmann, Sungkee S Ahn, Liangge Hsu, Ron Kikinis and Ferenc A Jolesz. *The evolution of multiple sclerosis lesions on serial MR.* American journal of neuroradiology, vol. 16, no. 7, pages 1481–1491, 1995. (Cited on pages 93, 107, 109 and 110.)

[Hahn 1952] EL Hahn and DE Maxwell. *Spin echo measurements of nuclear spin coupling in molecules.* Physical Review, vol. 88, no. 5, page 1070, 1952. (Cited on pages 7 and 33.)

[Henkelman 1985] R Mark Henkelman. *Measurement of signal intensities in the presence of noise in MR images.* Medical physics, vol. 12, no. 2, pages 232–233, 1985. (Cited on pages 84, 96 and 105.)

[Hennig 2004] Juergen Hennig, Matthias Weigel and Klaus Scheffler. *Calculation of Flip Angles for Echo Trains with Predefined Amplitudes with the Extended Phase Graph (EPG)-Algorithm: Principles and Applications to Hyperecho and TRAPS Sequences.* Magnetic Resonance in Medicine, vol. 51, no. 1, pages 68–80, 2004. (Cited on page 66.)

[Hohlfeld 1997] Reinhard Hohlfeld. *Biotechnological agents for the immunotherapy of multiple sclerosis. Principles, problems and perspectives.* Brain, vol. 120, no. 5, pages 865–916, 1997. (Cited on page 24.)

[Kanda 2013] Tomonori Kanda, Kazunari Ishii, Hiroki Kawaguchi, Kazuhiro Kitajima and Daisuke Takenaka. *High signal intensity in the dentate nucleus and globus pallidus on unenhanced T1-weighted MR images: relationship with increasing cumulative dose of a gadolinium-based contrast material.* Radiology, vol. 270, no. 3, pages 834–841, 2013. (Cited on page 110.)

[Kim 2017] Daeun Kim, Eamon K Doyle, Jessica L Wisnowski, Joong Hee Kim and Justin P Haldar. *Diffusion-relaxation correlation spectroscopic imaging: A multidimensional approach for probing microstructure.* Magnetic resonance in medicine, vol. 78, no. 6, pages 2236–2249, 2017. (Cited on page 126.)

[Kurtzke 1983] J F Kurtzke. *Rating neurologic impairment in multiple sclerosis: an expanded disability status scale (EDSS).* Neurology, vol. 33, no. 11, pages 1444–1452, 1983. (Cited on pages 18 and 19.)

[Lancaster 2003] Jack L Lancaster, Trevor Andrews, L Jean Hardies, Stephen Dodd and Peter T Fox. *Three-pool model of white matter.* Journal of Magnetic Resonance Imaging, vol. 17, no. 1, pages 1–10, 2003. (Cited on pages 13, 14, 44, 68, 73, 106, 110 and 111.)

[Lassmann 2001] Hans Lassmann, Wolfgang Bruck and Claudia Lucchinetti. *Heterogeneity of multiple sclerosis pathogenesis: Implications for diagnosis and*

therapy. Trends in Molecular Medicine, vol. 7, no. 3, pages 115–121, 2001. (Cited on pages 17, 22, 23, 24, 26, 64, 84, 85, 93, 105, 107, 109, 110 and 139.)

[Laule 2006] C Laule, E Leung, D KB Li, AL Traboulsee, DW Paty, AL MacKay and G RW Moore. *Myelin water imaging in multiple sclerosis: quantitative correlations with histopathology*. Multiple Sclerosis Journal, vol. 12, no. 6, pages 747–753, 2006. (Cited on page 14.)

[Laule 2007a] Cornelia Laule, Irene M. Vavasour, Shannon H. Kolind, David K. B. Li, Tony L. Traboulsee, G. R. Wayne Moore and Alex L. MacKay. *Magnetic resonance imaging of myelin*. Neurotherapeutics, vol. 4, no. 3, pages 460–484, 2007. (Cited on pages 11, 12, 14, 26, 34, 44, 110 and 111.)

[Laule 2007b] Cornelia Laule, Irene M Vavasour, Shannon H Kolind, Anthony L Traboulsee, GRW Moore, David KB Li and Alex L MacKay. *Long T 2 water in multiple sclerosis: What else can we learn from multi-echo T 2 relaxation?* Journal of neurology, vol. 254, no. 11, pages 1579–1587, 2007. (Cited on pages 14, 26, 27, 68, 85 and 122.)

[Laule 2007c] Cornelia Laule, Irene M Vavasour, Burkhard Mädler, Shannon H Kolind, Sandra M Sirrs, Elana E Brief, Anthony L Traboulsee, GR Wayne Moore, David KB Li and Alex L MacKay. *MR evidence of long T2 water in pathological white matter*. Journal of Magnetic Resonance Imaging: An Official Journal of the International Society for Magnetic Resonance in Medicine, vol. 26, no. 4, pages 1117–1121, 2007. (Cited on pages 14, 26, 27, 68, 85, 122 and 123.)

[Lawson 1995] Charles L Lawson and Richard J Hanson. Solving least squares problems. SIAM, 1995. (Cited on pages 9, 47 and 91.)

[Layton 2013] Kelvin J Layton, Mark Morelande, David Wright, Peter M Farrell, Bill Moran and Leigh A Johnston. *Modelling and Estimation of Multicomponent T_2 Distributions*. IEEE transactions on medical imaging, vol. 32, no. 8, pages 1423–1434, 2013. (Cited on pages 15, 16, 42, 48, 63, 66, 68, 90, 111, 121 and 133.)

[Leray 2010] Emmanuelle Leray, Jacqueline Yaouanq, Emmanuelle Le Page, Marc Coustans, David Laplaud, Joël Oger and Gilles Edan. *Evidence for a two-stage disability progression in multiple sclerosis*. Brain, vol. 133, no. 7, pages 1900–1913, 2010. (Cited on pages 18, 19, 22, 26 and 142.)

[Levesque 2010a] Ives R Levesque, Charmaine LL Chia and G Bruce Pike. *Reproducibility of in vivo magnetic resonance imaging–based measurement of myelin water*. Journal of Magnetic Resonance Imaging, vol. 32, no. 1, pages 60–68, 2010. (Cited on pages 13 and 14.)

[Levesque 2010b] Ives R Levesque, Paul S Giacomini, Sridar Narayanan, Luciana T Ribeiro, John G Sled, Doug L Arnold and G Bruce Pike. *Quantitative magnetization transfer and myelin water imaging of the evolution of acute multiple sclerosis lesions.* Magnetic resonance in medicine, vol. 63, no. 3, pages 633–640, 2010. (Cited on pages 26 and 89.)

[Lévy 2018] Simon Lévy, Marie-Claude Guertin, Ali Khatibi, Aviv Mezer, Kristina Martinu, Jen-I Chen, Nikola Stikov, Pierre Rainville and Julien Cohen-Adad. *Correction: Test-retest reliability of myelin imaging in the human spinal cord: Measurement errors versus region-and aging-induced variations.* PloS one, vol. 13, no. 6, page e0199796, 2018. (Cited on page 79.)

[Lexell 2005] Jan E Lexell and David Y Downham. *How to assess the reliability of measurements in rehabilitation.* American journal of physical medicine & rehabilitation, vol. 84, no. 9, pages 719–723, 2005. (Cited on page 63.)

[Lublin 2014] Fred D. Lublin, Stephen C. Reingold, Jeffrey A. Cohen, Gary R. Cutter, Per Soelberg Sorensen, Alan J. Thompson, Jerry S. Wolinsky, Laura J. Balcer, Brenda Banwell, Frederik Barkhof, Bruce Bebo, Peter A. Calabresi, Michel Clanet, Giancarlo Comi, Robert J. Fox, Mark S. Freedman, Andrew D. Goodman, Matilde Inglese, Ludwig Kappos, Bernd C. Kieseier, John A. Lincoln, Catherine Lubetzki, Aaron E. Miller, Xavier Montalban, Paul W. O'Connor, John Petkau, Carlo Pozzilli, Richard A. Rudick, Maria Pia Sormani, Olaf St??ve, Emmanuelle Waubant and Chris H. Polman. *Defining the clinical course of multiple sclerosis: The 2013 revisions.* Neurology, vol. 83, no. 3, pages 278–286, 2014. (Cited on pages 19, 20, 21, 22 and 142.)

[Lucchinetti 1999] Claudia Lucchinetti, Wolfgang Brück, Joseph Parisi, Bernd Scheithauer, Moses Rodriguez and Hans Lassmann. *A quantitative analysis of oligodendrocytes in multiple sclerosis lesions.* Brain, vol. 122, no. 12, pages 2279–2295, 1999. (Cited on page 23.)

[MacKay 1994] A. MacKay, K. Whittall, J. Adler, D. Li, D. Paty and D. Graeb. *In vivo visualization of myelin water in brain by magnetic resonance.* Magnetic Resonance in Medicine, vol. 31, no. 6, pages 673–677, 1994. (Cited on pages 11, 12, 14, 33 and 34.)

[MacKay 2006] Alex MacKay, Cornelia Laule, Irene Vavasour, Thorarin Bjarnason, Shannon Kolind and Burkhard Mädler. *Insights into brain microstructure from the T2 distribution.* Magnetic Resonance Imaging, vol. 24, no. 4, pages 515–525, 2006. (Cited on page 26.)

[MacKay 2016] Alex L MacKay and Cornelia Laule. *Magnetic Resonance of Myelin Water: An in vivo Marker for Myelin.* Brain Plasticity, vol. 2, no. 1, pages 71–91, 2016. (Cited on pages 11, 12, 14, 26, 27, 34, 44, 68, 110, 111, 125, 141 and 142.)

[McGraw 1992] Kenneth O McGraw and SP Wong. *A common language effect size statistic.* Psychological bulletin, vol. 111, no. 2, page 361, 1992. (Cited on page 100.)

[Meiboom 1958] Saul Meiboom and David Gill. *Modified spin-echo method for measuring nuclear relaxation times.* Review of scientific instruments, vol. 29, no. 8, pages 688–691, 1958. (Cited on page 7.)

[Olchowy 2017] Cyprian Olchowy, Kamil Cebulski, Mateusz Lasecki, Radoslaw Chaber, Anna Olchowy, Krzysztof Kalwak and Urszula Zaleska-Dorobisz. *The presence of the gadolinium-based contrast agent depositions in the brain and symptoms of gadolinium neurotoxicity-A systematic review.* PLoS One, vol. 12, no. 2, page e0171704, 2017. (Cited on page 110.)

[Ourselin 2000] Sébastien Ourselin, Alexis Roche, Sylvain Prima and Nicholas Ayache. *Block matching: A general framework to improve robustness of rigid registration of medical images.* In Medical Image Computing and Computer-Assisted Intervention–MICCAI 2000, pages CH373–CH373. Springer, 2000. (Cited on pages 51, 52, 75, 94 and 113.)

[Panagiotaki 2012] E. Panagiotaki*et al.* *Compartment models of the diffusion MR signal in brain white matter: A taxonomy and comparison.* Neuroimage, vol. 59, no. 3, pages 2241–2254, 2012. (Cited on pages 110 and 112.)

[Prasloski 2012] Thomas Prasloski, Burkhard Mädler, Qing San Xiang, Alex MacKay and Craig Jones. *Applications of stimulated echo correction to multicomponent T2 analysis.* Magnetic Resonance in Medicine, vol. 67, no. 6, pages 1803–1814, 2012. (Cited on pages 9, 12, 16, 42, 47, 48, 67, 111, 121 and 133.)

[Purcell 1946] Edward M Purcell, H Co Torrey and Robert V Pound. *Resonance absorption by nuclear magnetic moments in a solid.* Physical review, vol. 69, no. 1-2, page 37, 1946. (Cited on page 3.)

[Raj 2014] Ashish Raj, Sneha Pandya, Xiaobo Shen, Eve LoCastro, Thanh D Nguyen and Susan A Gauthier. *Multi-compartment T2 relaxometry using a spatially constrained multi-Gaussian model.* PLoS One, vol. 9, no. 6, page e98391, 2014. (Cited on pages 15 and 16.)

[Rovira 2013] Alex Rovira, Cristina Auger and Juli Alonso. *Magnetic resonance monitoring of lesion evolution in multiple sclerosis.* Therapeutic advances in neurological disorders, vol. 6, no. 5, pages 298–310, 2013. (Cited on page 25.)

[Rovira 2015] Àlex Rovira, Mike P Wattjes, Mar Tintoré, Carmen Tur, Tarek A Yousry, Maria P Sormani, Nicola De Stefano, Massimo Filippi, Cristina Auger, Maria A Rocca*et al.* *Evidence-based guidelines MAGNIMS consensus guidelines on the use of MRI in multiple sclerosis clinical implementation in*

the diagnostic process. Nature Reviews Neurology, vol. 11, no. 8, page 471, 2015. (Cited on pages 19, 20, 25 and 26.)

[Russek 2012] SE Russek, M Boss, EF Jackson, DL Jennings, JL Evelhoch, JL Gunter and AG Sorensen. *Characterization of NIST/ISMRM MRI system phantom.* In Proceedings of the 20th Annual Meeting of ISMRM, Melbourne, Australia, page 2456, 2012. (Cited on pages 50 and 74.)

[Stamm 2016] Aymeric Stamm, Olivier Commowick, Simon K Warfield and Simone Vantini. *Comprehensive Maximum Likelihood Estimation of Diffusion Compartment Models Towards Reliable Mapping of Brain Microstructure.* In MICCAI, volume 9902 of *LNCS*, pages 622 – 630, 2016. (Cited on page 112.)

[Stanisz 1998] Greg J Stanisz and R Mark Henkelman. *Diffusional anisotropy of T2 components in bovine optic nerve.* Magnetic resonance in medicine, vol. 40, no. 3, pages 405–410, 1998. (Cited on pages 11, 15, 16 and 33.)

[Svanberg 2002] K Svanberg. *A class of globally convergent optimization methods based on conservative convex separable approximations.* SIAM journal on optimization, vol. 12, no. 2, pages 555–573, 2002. (Cited on page 73.)

[Tofts 2005] Paul Tofts. *Quantitative MRI of the brain: measuring changes caused by disease.* chapter 14, pages 477–500. John Wiley & Sons, 2005. (Cited on pages 5, 6, 9, 17 and 141.)

[Van Waesberghe 1999] J. H T M Van Waesberghe, W. Kamphorst, C. J A De Groot, M. A A Van Walderveen, J. A. Castelijns, R. Ravid, G. J. Lycklama À Nijeholt, P. Van Der Valk, C. H. Polman, A. J. Thompson and F. Barkhof. *Axonal loss in multiple sclerosis lesions: Magnetic resonance imaging insights into substrates of disability.* Annals of Neurology, vol. 46, no. 5, pages 747–754, 1999. (Cited on page 26.)

[Vargas 2015] Wendy S Vargas, Elizabeth Monohan, Sneha Pandya, Ashish Raj, Timothy Vartanian, Thanh D Nguyen, Sandra M Hurtado Rúa and Susan A Gauthier. *Measuring longitudinal myelin water fraction in new multiple sclerosis lesions.* NeuroImage: Clinical, vol. 9, pages 369–375, 2015. (Cited on page 90.)

[Vavasour 2009] IM Vavasour, C Laule, DKB Li, J Oger, GRW Moore, A Traboulsee and AL MacKay. *Longitudinal changes in myelin water fraction in two MS patients with active disease.* Journal of the neurological sciences, vol. 276, no. 1, pages 49–53, 2009. (Cited on page 89.)

[Whittall 1989] Kenneth P Whittall and Alexander L MacKay. *Quantitative interpretation of NMR relaxation data.* Journal of Magnetic Resonance (1969), vol. 84, no. 1, pages 134–152, 1989. (Cited on pages 12 and 14.)

[Whittall 1997] K P Whittall, A L MacKay, D A Graeb, R A Nugent, D K Li and D W Paty. *In vivo measurement of T2 distributions and water contents in normal human brain.* Magnetic resonance in medicine, vol. 37, no. 1, pages 34–43, 1997. (Cited on pages 11, 12, 14, 26 and 33.)

Gaining insights into brain tissues using multi-compartment T_2 relaxometry models

Abstract: Magnetic resonance imaging (MRI) is one of the most widely used in-vivo imaging method for obtaining information on brain health. However, MRI voxels have limited resolution due to physical constraints. The objective of this thesis is to obtain quantitative estimates of brain tissue microstructures (such as myelin, intra/extracellular matters and free water) from T2 relaxometry MRI data. Two parametric multi-compartment T2 relaxometry (MCT2) models are proposed in this thesis. The approach and estimation framework for both models were justified using cost function simulation studies. A range of simulation and in-vivo MRI data experiments were performed to evaluate the accuracy and robustness of these models. The model found to be more robust of the two was then used for two studies on multiple sclerosis (MS) lesions. In the first study the evolution of the MCT2 biomarkers was studied in gadolinium (Gd) enhancing and non-enhancing regions of MS lesions in 10 patients with clinically isolated syndrome over a period of three years. In the second study we demonstrated the potential of combined use of the proposed MCT2 biomarkers with those obtained from existing multi-compartment diffusion MRI models to address a clinically relevant and challenging task of identifying regions of MS lesions undergoing active blood brain barrier breakdown without use of Gd injection.
Keywords: microstructure, brain, multiple sclerosis, relaxometry, T_2